A study on the processes that cause extreme precipitation on the west coast of Norway.

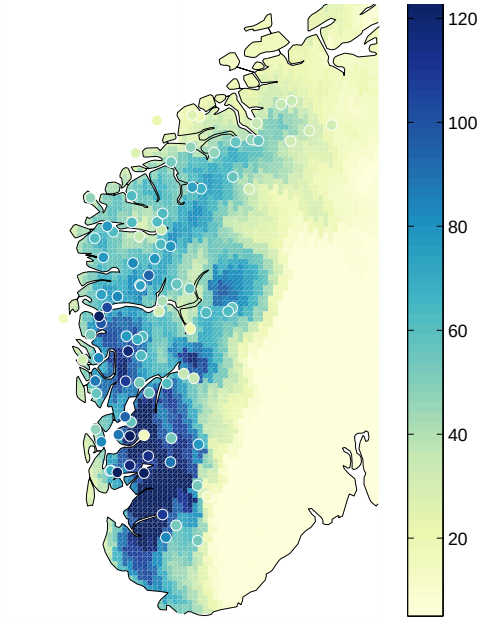

Master Thesis in Climate Dynamics

Mari Ingeborg Sandvik

November 2011

UNIVERSITY OF BERGEN
GEOPHYSICAL INSTITUTE

The figure on the front page shows
the distribution of daily precipitation
for 15. November 2005. The values are
produced by the WRF model, and observations
are shown as circles. The colours represent
the magnitude of the precipitation.

Abstract

The purpose of this thesis was to get a deeper understanding of extreme daily precipitation events on the west coast of Norway. To examine the extreme precipitation on the west coast of Norway, daily precipitation events are investigated by using observations from 114 stations in the time period 1961-2009. The main focus is given to three of the 50 most extreme daily precipitation events; one winter, one spring and one fall event. By using the Weather Research Forecast model and by changing the sea surface temperature, changes in pattern and intensity for the three events are investigated. Parameters such as daily precipitation, specific humidity, relative humidity, vertical velocity and static stability are used to validate the findings. A general shift in the distribution of the daily precipitation is seen for both the winter and fall events, where the combination of vertical velocity and relative humidity seems to be the largest contributors. The change in intensity of daily precipitation differs greatly between the events, with over 20% increase for the spring event and under 5% for the fall event. Static stability combined with relative humidity can explain the different responses in the intensity for the three events. Two simple methods for calculating theoretical precipitation are introduced, but the change in both intensity and distribution makes it difficult for the two methods to produce good predictions of individual extreme daily precipitation events. By introducing thresholds for parameters such as relative humidity, time delay for hydrometeor production and fall speed of the precipitation in the simple methods, more accurate presentation of the daily precipitation may be produced.

Acknowledgement

First of all, I would like to express my gratitude to my supervisor Asgeir Sorteberg. He has been amazing in guiding me through the thesis, with inspiration and created a deeper interest for the subject. Whenever I came to his office, he always made time to help and give me new ideas for possible further work.

For me who have never worked with a numerical model, Torleif Markussen Lunde at the Geophysical institute has been a life saver. Whenever the model did not work or produced unreasonable result, which was quite often, he was always there to help. Things would have been a lot more stressful without his amazing help, so thank you so much!

A special thanks to Brian Aubrey, Lisbeth Håvik and Morten Erlbeck for taking their time to proofread my thesis. All of your help is highly appreciated and most definitely needed.

Would also like to give a special thanks to my parents, Anne Sofie Sandvik and Andreas Sandvik, and my brother, Martin Sandvik, for always picking up the phone and comfort me whenever I felt lost or sad. I would not have been here without your support and love.

Lastly, I would like to say thanks to all of my fellow students, who have made these last 5 and a half years an incredible experience. Hope that we all can continue our journey together.

Contents

Chapter 1

Introduction

The southern part of Norway is divided into two climatic regions by the mountain range Langfjella (Figure 1.1). The area to the east of Langfjella has an inland climate, with a large seasonal cycle in temperature. Most of the extreme precipitation events in these areas occur during summer, when the conditions are favourable for convection. The western side of the mountains on the other hand, has a more coastal climate, with general wet weather and mild temperatures all year long. Extreme precipitation is mostly experienced during late fall and winter due to the frequent occurrence of intense extratropical cyclones (Bengtsson et al., 2009). These low pressure and frontal systems drives air, which is a mix of warm humid air from the south and cold air from polar areas, towards the west coast of Norway. The west coast of Norway has a complex topography with fjords, mountains, and deep and narrow valleys. The combination of the synoptic scale flow with the orographic enhancement of precipitation is the main cause of the extreme precipitation rates that are being recorded for this part of Norway. The complexity of the terrain is also causing large variability in the observed precipitation amount over relatively short distances. In general, the west coast of Norway experiences large amounts of precipitation, typically exceeding 2000 mm/year (Heikkilä et al., 2010).

The amount and distribution of precipitation has a large influence on both ecology and agriculture. The ability to predict both amount of precipitation and the time frame the precipitation is observed are important for human life. On a day to day basis, the Norwegian people are interested in when it is going to precipitate. Forecasts are therefore often seen by people as good if rain occurs when the forecast predicted it, even if the amount is not of the same magnitude. Heavy precipitation, especially over a short time period, could result in destruction of infrastructures and also loss of human life due to floods, avalanches and landslides. Extreme precipitation is the largest reason for snow

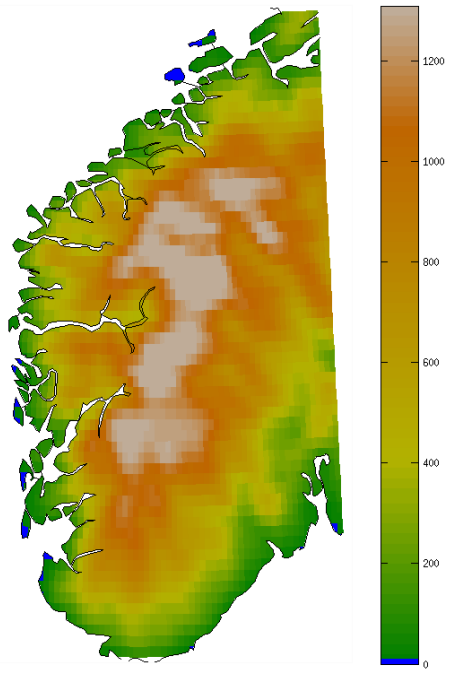

Figure 1.1: Topography of Norway, where the colorbar represents the elevation above sea level (m). The figure is created by geogrid.exe in the Weather Research Forecast model with a 10 km resolution. More details on the model will be presented later in the thesis.

avalanches on the west coast of Norway (Jaedicke et al., 2008). These avalanches are the geohazard that most frequently leads to loss of lives and destruction of infrastructure in Norway(Jaedicke et al., 2008). By being able to predict certain meteorological parameters such as heavy rain and strong winds one may be able to better predict the different landslides and avalanches (Jaedicke et al., 2008). Climate scenarios with climatic warming done by ResClim (2005) indicates an increased risk of precipitation extremes occurring more frequently in the next 100 years. The annual amount of precipitation has been estimated to increase up to 20% on the western part of southern Norway, with the largest increase of precipitation predicted to happen during fall (ResClim, 2005). Due to this it is important that numerical models are able to predict where and when these events will occur, so lives and costs of rebuilding destroyed infrastructures can be saved. A better understanding on how different parameters change the intensity and distribution of a precipitation amount, could result in a better representation in the different models used in both research and weather forecasting.

The main aim of this thesis is therefore to provide more information on how the intensity and distribution of an extreme precipitation event changes with a change in Sea Surface Temperature (SST). This change in SST will be equally distributed, so the temperature gradient is not changed. The study is divided into two parts. In the first part, the time

distribution of the 50 most extreme daily precipitation event between 1961-2009 is investigated. Events are classified as more extreme if a large number of the 114 stations in the area experienced extreme precipitation for the given event. The second part present three case studies where the different events are simulated to see how changes in SST influence the precipitation in both intensity and distribution. An important aspect is to test if simple theory on calculating the theoretical precipitation change due to temperature changes is valid for the three different events (e.g. Pall et al. (2007); Trenberth (1999); Haltiner & Williams (1980); Sinclair (1994)), and to try and draw some general conclusions from the different simulations.

Chapter 2 introduces some general theory on orographic enhanced precipitation and how to calculate the theoretical precipitation. Further the statistical measures used to validate the performance of the simulation on the daily precipitation amount are presented in Chapter 3. A description of the Weather Research and Forecast model (WRF) is given in Chapter 4. The setup and a description of the different simulations are also described in this chapter. The results and discussion from the observational study are presented in Chapter 5, where the variability in space and the synoptic situation for the 50 most extreme precipitation events on the west coast of Norway between 1961-2009 are the main focus. The three case studies are presented in Chapter 6. The main focus in this chapter is to see how the WRF model simulates the three extreme precipitation events, and how sensitive the precipitation is to a two degree change in the SST for the entire domain. Different parameters important for precipitation formation are compared to explain the results. Chapter 7 contain a final summary and the overall conclusions found in this thesis. Future work is given i Chapter 8.

Chapter 2

Theory

2.1 Orographic precipitation

Different formation mechanisms of orographic precipitation have been documented over the last few decades. Three major mechanisms were identified in Smith (1979). Two of these are important mechanisms for orographic precipitation on the west coast of Norway. Therefore only these two will be presented here.

When air is forced over large mountains, the air cools adiabatically due to the decrease in pressure. If the air reaches its Lifting Condensation Level (LCL) it becomes saturated and condensation will occur. The resulting cloud and hydrometeor[1] formation enhances the precipitation upstream of the mountain slope (Figure 2.1a). Downstream, on the

[1] Water and ice particles that have formed due to condensation or sublimation either in the atmosphere or at the Earth's surface.

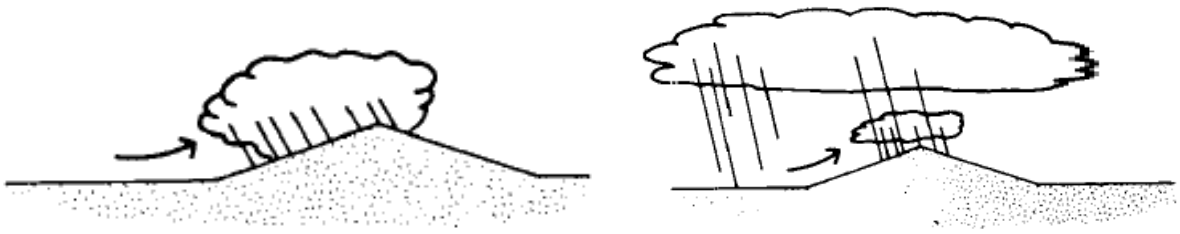

(a) (b)

Figure 2.1: Two of the three major mechanisms of orographic precipitation presented in (Smith, 1979). a) represents the case of forced lifting of large scale mountains, and b) represents the seeder-feeder mechanism.

leeside of the mountain, the air descends creating a rain shadow. A well known concept is that the precipitation efficiency, the ratio of the total condensation rate, increases with increased width of a mountain with a specific mountain height (Jiang & Smith, 2003). This has to do with the advection time[2], which increases with increased mountain width. Jiang & Smith (2003) found that by increasing the mountain width, the slope of the mountain decreases causing the accretion process[3]to slow down and the time to produce snow to increase.

Over smaller hills on the other hand, the time scale is too short for hydrometeor formation (Bergeron, 1949). Bergeron (1960) introduced the so-called "seeder-feeder" mechanism (Figure 2.1b). As a higher cloud system (seeder) produced by fronts or troughs moves over a small mountain while precipitating, some of the precipitation will evaporate as it falls toward the ground. A result of this is more moisture in the lowest layer of the atmosphere. Forced vertical lifting of lower level air due to topography causes the air to reach saturation and condensate (feeder). Precipitation from the seeder cloud that falls through the feeder cloud can wash out water droplets from the feeder cloud (Sinclair, 1994), producing a maximum of precipitation near the top of the mountain. In other words, the precipitation is not produced by forced lifting alone as over large mountains.

Whether air flows over an obstacle depends on the shape of the mountain, its extension, height, the horizontal wind speed and the stability of the air. Moisture also has an effect on the orographic flow, by reducing the static stability (Durran & Klemp, 1982). Kunz & Kottmeier (2006) found precipitation to be very sensitive to wind speed, static stability, mountain height, and temperature at 1000 hPa, especially on the windward side of the mountain by the use of linear theory. For saturated flow over a mountain, the moist Froude number, Fr_m, is defined as

$$Fr_m = \frac{1}{M_m} = \frac{U}{N_m H}, \tag{2.1}$$

where M_m is the non-dimensional mountain height[4], U is the horizontal wind speed and N_m is the moist Brunt-Väisälä frequency which indicates the static stability of the atmosphere (Kunz & Kottmeier, 2006). The air tends to flow over mountains when Fr_m is larger than 1. Vertical velocities produced by the topography increase as Fr increases, resulting in an increase in precipitation intensities (Kunz & Kottmeier, 2006).

[2]The time where hydrometeor formation and precipitation can occur

[3]Growth of hydrometeors by larger precipitation particles overtakes and capture smaller ones. Often used for the capture of supercooled droplets by an ice particle (Rogers & Yau, 1989).

[4]The non-dimensional mountain height measures the non-linearity produced in the flow. When it is much less than 1, linear theory give accurate results. (Markowski et al., 2010)

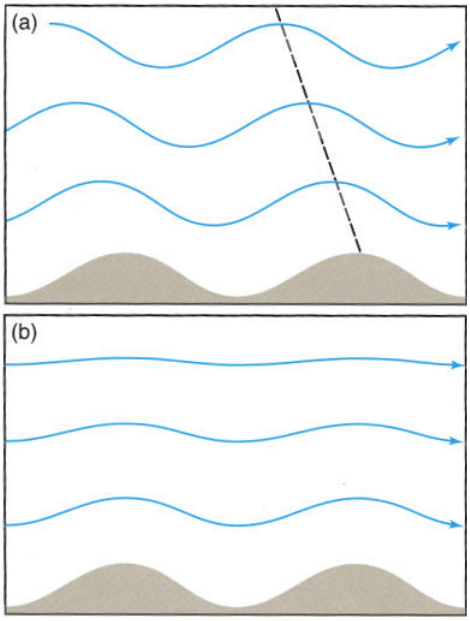

Figure 2.2: Streamlines for steady flow over a series of sinusoidal mountains. a) represents the case where $N^2 > u_0^2k^2$, and b) represents the case where $N^2 < u_0^2k^2$(Markowski et al., 2010).

If the air is able to flow over an obstacle, the orography may induce wave motion. As explained in Markowski et al. (2010), internal wave theory can be used to develop a simple expression for the perturbation vertical velocity, w'. Consider a series of sinusoidal mountains, with a distance of L_x between each mountain top. L_x defines the horizontal wavenumber $k = \frac{2\pi}{L_x}$, in x direction, of the terrain. Assume that the speed of the airflow, u_0, and the static stability, N, in the environmental atmosphere is held constant. When $N^2 > u_0^2k^2$ an oscillation can be supported along an angle $\phi = cos^{-1}(u_0k/N)$, see Figure 2.2a. In other words, the wavefronts are tilted with height. The wave solution will be in the form

$$w' = u_0kh_mcos(kx + mz), \tag{2.2}$$

where h_m is the amplitude of the mountain terrain, x and z indicates the position in x- and z-direction, and m is the vertical wave number. When $N^2 < u_0^2k^2$ the atmosphere cannot support oscillations. The waves are decaying with height, see Figure 2.2b. The wave solution here is in the form

$$w' = u_0kh_me^{-\mu z}cos(kx), \tag{2.3}$$

where μ is the real part of the vertical wavenumber, m.

To get an idea of the magnitude of w' for the west coast of Norway a simple scale analysis

can be used. From Figure 1.1, both the wave length and the amplitude of the mountain terrain can be found for the mountain range Langfjella. L_x is around 300 km and h_m is about 1000 m. The average speed for the airflow can be set as 10 ms^{-1}. By looking at the ground the wave solution w' will oscillate between approximate 0.2 and -0.2 ms^{-1}.

2.2 Theoretical precipitation

For weather forecasting and hydrologists it is important to give an accurate estimation of precipitation (Sinclair, 1994). Precipitation is the total amount of condensed water vapor in all vertical layers, in case of no evaporation. The theoretical precipitation, P_t, when assuming that all condensation fall out immediately, can therefore be defined as

$$P_t = \int_t^{t+\Delta t} \int_0^{\infty} c\rho dz dt, \tag{2.4}$$

where c is the condensation rate and ρ is the air density. An assumption that the whole air column is saturated is often made to simplify calculations. The condensation rate can be defined as

$$c = -\frac{dq_s}{dt},\ when\ \frac{dq_s}{dt} < 0 \tag{2.5}$$

and

$$c = 0,\ when\ \frac{dq_s}{dt} > 0 \tag{2.6}$$

where q_s is the specific humidity. For simplicity, the precipitation is viewed as proportional to how specific humidity changes with time. There are two ways to consider how specific humidity changes with time, presented in Alternative 1 and Alternative 2.

Alternative 1

How the specific humidity changes with time may be defined as

$$\frac{dq_s}{dt} = \frac{dq_s}{dT}\frac{dT}{dz}\frac{dz}{dt}. \tag{2.7}$$

$\frac{dq_s}{dT}$ can be expressed by Clausius Clapeyrons equation, since $q_s \approx \varepsilon \frac{e_s}{p}$. Here $\varepsilon \approx 0.622$ and e_s is the saturation vapor pressure. $\frac{dT}{dz}$ gives indications on how the temperature changes with height. $\frac{dz}{dt}$ is the vertical velocity w, where z is the vertical coordinate. The simplest solution is that precipitation is assumed to only depend on the $\frac{dq_s}{dT}$ term, and

Table 2.1: Saturation vapor pressure over water and ice, and latent heats of condensation and sublimation (Rogers & Yau, 1989).

T(°C)	e_s(Pa)	e_i(Pa)	L(J/g)	L_s(J/g)
-40	19.05	12.85	2603	2839
-35	31.54	22.36		
-30	51.06	38.02	2575	2839
-25	80.90	63.30		
-20	125.63	103.28	2549	2838
-15	191.44	165.32		
-10	286.57	259.92	2525	2837
-5	421.84	401.78		
0	611.21	611.15	2501	2834
5	872.47		2489	
10	1227.94		2477	
15	1705.32		2466	
20	2338.54		2453	
25	3168.54		2442	
30	4245.20		2430	
35	5626.45		2418	
40	7381.27		2406	

the two other terms are assumed constant. Clausius Clapeyron equation is defined as

$$\frac{de_s}{dT} = \frac{Le_s}{R_v T^2}, \tag{2.8}$$

where L is the latent heat, $R_v = 461\text{JK}^{-1}\text{kg}^{-1}$ is the gas constant for water vapor, and T is the temperature (Rogers & Yau, 1989). The saturation vapor pressure, e_s, is a function of temperature and can be defined as

$$e_s(T) = 6.112exp\left(\frac{17.67T}{T+243.5}\right), \tag{2.9}$$

where e_s(T) is given in hPa and T in ^{o}C. Bolton (1980) found that Equation (2.9) was able to produce values to an accuracy of 0.1% for $-30^o\text{C} \leq \text{T} \geq 30^o\text{C}$.

Table 2.1 can be used to calculate the change in specific humidity per temperature. Taking the percentage change in q_s for two temperatures and divide it by the temperature change, the change in specific humidity is about 6-8 %/K, solid blue line in Figure 2.3. Assuming that the atmospheric layer is saturated and constant, w is constant and $\frac{dT}{dz}$ is constant, precipitation should change with 6-8 %/K.

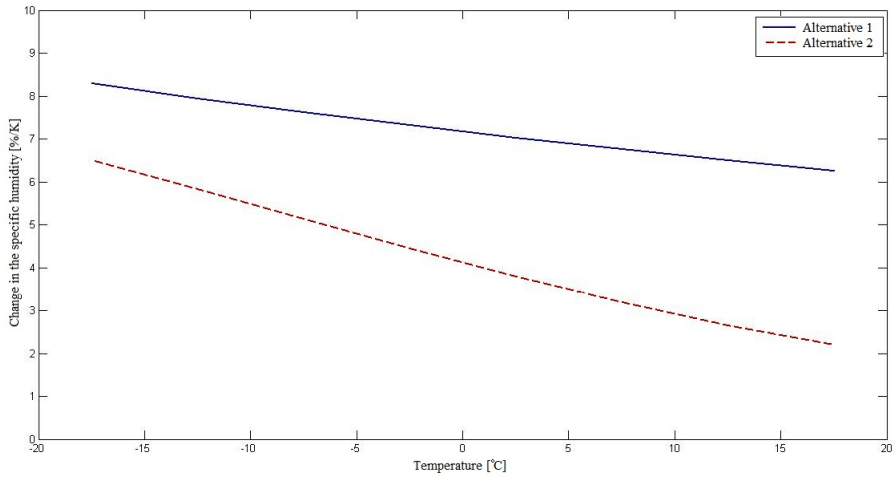

Figure 2.3: The change in specific humidity (%/K) for different temperatures (^oC). Alternative 1 (the solid blue line) is created by assuming that $\frac{dq_s}{dt}$ is approximately equal to $\frac{dq_s}{dT}$ which can be calculated by Clausius Clapeyrons equation. Alternative 2 (the broken red line), is created by assuming that $\frac{dq_s}{dt}$ is approximately equal to $\frac{dq_s}{dp}$, which can be calculated by equation (2.12)

Alternative 2

Latent heat release due to condensation will influence how the temperature changes in the vertical. In other words $\frac{dT}{dz}$ will be influenced. To include the changes in temperature in the vertical $\frac{dq_s}{dt}$ can be defined as

$$\frac{dq_s}{dt} = \frac{dq_s}{dp}\frac{dp}{dt}. \tag{2.10}$$

$\frac{dp}{dt}$ is the vertical velocity, ω, in pressure coordinates. A change in temperature will now be expressed in the term $\frac{dq_s}{dp}$, and is no longer constant.

Precipitation due to adiabatic lifting of a saturated air parcel can then be defined as

$$P = -\frac{1}{g_0}\int_t^{t+\Delta t}\int_0^{\infty}\frac{q_s T}{p}\left(\frac{L_v R - c_p R_v T}{c_p R_v T^2 + q_s L_v^2}\right)\omega dp dt, \tag{2.11}$$

where P is the amount of precipitation (Haltiner & Williams, 1980). q_s is the specific humidity at saturation, T is the temperature, p is the pressure, L_v is the latent heat of evaporation, R and R_v is the gas constant for air and the gas constant for water vapor. The specific heat constant for constant pressure is defined by c_p, and finally ω is the vertical velocity in a pressure coordinate system. The assumptions behind this equation are no temperature advection, no evaporation of falling precipitation and no radiative cooling or heating. Hence, adiabatic lifting is the only force that gives condensation

and all the water vapor that condensates will fall towards the ground instantaneously. By comparing Equation (2.11) with Equation (2.4) the specific humidity changes with pressure can be defined as

$$\frac{dq_s}{dp} = \frac{q_s T}{p}\left(\frac{L_v R - c_p R_v T}{c_p R_v T^2 + q_s L_v^2}\right). \tag{2.12}$$

Taking the percentage change in $\frac{dq_s}{dp}$ for two temperatures and dividing it by the temperature change, the change in specific humidity is about 2-6 %/K depending on the environmental temperature, broken red line in Figure 2.3. Assuming that ω does not change , precipitation would change with 2-6%/K

To summarize, two estimates on how precipitation should change with a change in temperature are presented. The amount of precipitation dependent on the variables T (which determines q_s), $\frac{dT}{dz}$ and ω or w. The vertical velocity and temperature gradient are both dependent on the static stability.

In reality, precipitation does not fall instantaneously to the ground. There is also no guarantee that the vertical velocity would remain unchanged in a changed climate. Hydrometeors may need up to several minutes to grow large enough to escape from the cloud environment due to gravity (Sinclair, 1994). In addition, the hydrometeor needs a finite time to fall a certain length from the cloud base to the surface (Sinclair, 1994), hence there is a delay between the position of the production of the precipitation to the position where the precipitation reaches the ground. The whole air column is not saturated either, which is assumed for the theoretical maximum precipitation. To be able to calculate the precipitation better, thresholds can be introduced. Orographic precipitation is dependent on the moisture contained in the lower levels (Sinclair, 1994). The threshold work as a critical point where values higher (lower) than the threshold indicates precipitation (no precipitation). A lower relative humidity threshold of 80 % seems to give good results for orographic rainfall (Bader & Roach (1977); Sinclair (1994)).

Chapter 3

Statistical validation measures

There are many ways to perform and present the validation of a forecast, and how well the forecast is predicting a meteorological parameter. This section contain a description of the two statistical errors that have been used to verify the model runs presented later in the thesis. Information given here is from Willmott & Matsuura (2005).

3.1 Mean Absolute Error (MAE)

The MAE measure how close the model is to reproduce the individual observations. The MAE is given as an absolute value and ranges between 0 and ∞. Therefore MAE does not consider the direction of the error. The lower the value of the MAE, the better the performance of the model.

$$MAE = \frac{1}{n}\sum_{i=1}^{n}|x_{mod} - x_{obs}|, \tag{3.1}$$

where n is the number of observations, and x_{mod} are the different values created by the model, whereas x_{obs} are the actual observational values.

3.2 Mean Bias Error (MBE)

MBE measures the average error in percentage over time, and is defined as

$$MBE = \frac{\frac{1}{n}\sum_{i=1}^{n} x_{mod} - x_{obs}}{\frac{1}{n}\sum_{i=1}^{n} x_{obs}} \times 100. \tag{3.2}$$

The direction of the error is considered here. MBE is related to the magnitude of the typical error. It ranges between $-\infty$ to ∞, and is given in percent. It is important to remember that even if MBE is close to zero, it is not given that the model has produced a good performance for individual days. The reason is that individual errors may cancel each other out.

Chapter 4

A description of the model and the different simulations

The Weather Research and Forecast (WRF) model has been used in this thesis to be able to give some indications on how sensitive extreme precipitation events are to changes in the Sea Surface Temperature (SST). The information below is from Skamarock et al. (2008) if nothing else is stated.

4.1 Weather Research and Forecast model

The WRF model is a Numerical Weather Prediction (NWP) and atmospheric simulation system. It is being used both for research and operational weather forecasting. The development of the model was to advance the understanding and ability to predict mesoscale

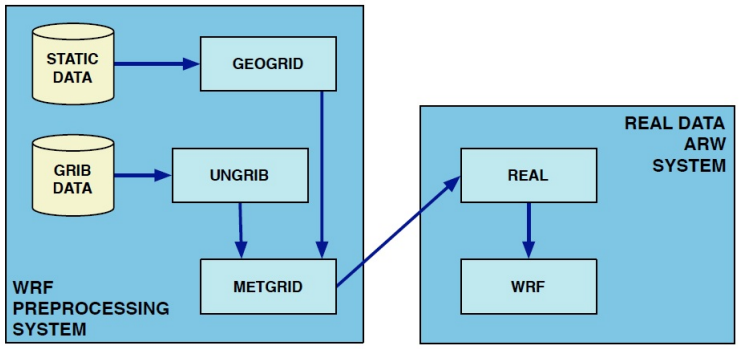

Figure 4.1: Easy visualization of the model setup for the WRF model (Skamarock et al., 2008).

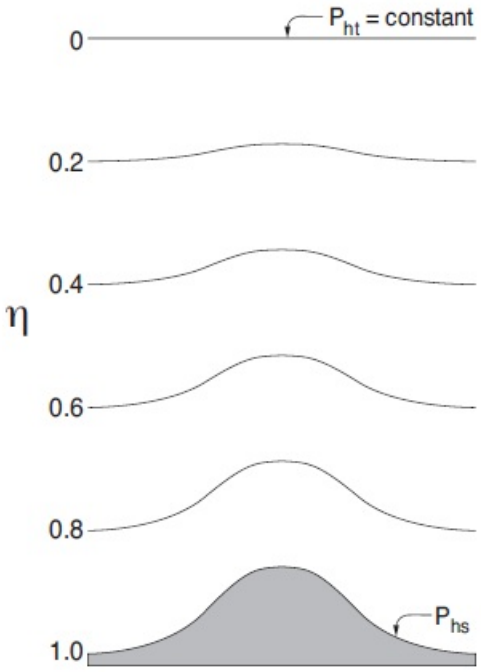

Figure 4.2: Vertical coordinate system used in the ARW dynamic solver (Skamarock et al., 2008).

weather, and to accelerate the transfer of research into operations. Building the model has been a collaboration between the Mesoscale and Microscale Meteorology (MMM) Division of the National Center for Atmospheric Research (NCAR), the National Center for Environmental Prediction (NCEP) and the Earth System Research Laboratory (ESRL) of the National Oceanic and Atmospheric Administration (NOAA), University of Oklahoma's Center for Analysis and Prediction of Storms (CAPS), and the Federal Aviation Administration (FAA), with participation of university scientists.

A simple visualization of the WRF model with the advanced research (ARW) solver as its dynamic solver can be viewed in Figure 4.1. For an idealized case or for a real data case the ARW solver is often used. The WRF preprocessing system will be explained more in detail in Section 3.1.4 under initial conditions.

4.1.1 Governing equations

The ARW dynamic solver is integrating the Euler equations. These equations are compressible and nonhydrostatic. They are formulated by the use of a mass vertical coordi-

nate. This coordinate system uses terrain-following hydrostatic-pressure vertical coordinate, η (Laprise, 1992), and is defined as

$$\eta = \mu^{-1}(p_h - p_{ht}), \tag{4.1}$$

where $\mu = p_{hs} - p_{ht}$. The hydrostatic component of the pressure is denoted as p_h in the equation, while p_{hs} and p_{ht} is giving the value of the pressure along the surface and top boundaries. η is varying between 1 at the surface to 0 at the top boundary (Figure 4.2). This coordinate definition has been used in many hydrostatic atmospheric models.

In the model domain at (x,y), $\mu(x, y)$ represents the mass per unit area within the column. From this the flux form variables are defined as

$$\mathbf{V} = \mu\mathbf{v} = (U, V, W), \;\; \Omega = \mu\dot{\eta}, \;\; \Theta = \mu\theta, \tag{4.2}$$

where $\mathbf{v} = (u, v, w)$ is the covariant velocities for the three dimensions. $\omega = \dot{\eta}$ is the "vertical" velocity that follows the terrain-following hydrostatic-pressure vertical coordinate system, and θ is the potential temperature. In ARW, the non-conserved variables such as geopotential ($\phi = gz$), pressure (p), and inverse density ($\alpha = 1/\rho$) are also appearing in the governing equations.

The flux form of the Euler equations can be written as

$$\partial_t U + (\nabla \cdot \mathbf{V}u) - \partial_x(p\partial_\eta\phi) + \partial_\eta(p\partial_x\phi) = F_U \tag{4.3}$$

$$\partial_t V + (\nabla \cdot \mathbf{V}v) - \partial_y(p\partial_\eta\phi) + \partial_\eta(p\partial_y\phi) = F_V \tag{4.4}$$

$$\partial_t W + (\nabla \cdot \mathbf{V}w) - g(\partial_\eta p - \mu) = F_W \tag{4.5}$$

$$\partial_t \Theta + (\nabla \cdot \mathbf{V}\theta) = F_\Theta \tag{4.6}$$

$$\partial_t \mu + (\nabla \cdot \mathbf{V}) = 0 \tag{4.7}$$

$$\partial_t \phi + \mu^{-1}[(\mathbf{V} \cdot \nabla\phi) - gW] = 0. \tag{4.8}$$

The prognostic equations (4.3) to (4.8) are written in conservative form, the properties are conserved through a control volume in a fixed position relative to the coordinate axes (Holton, 2004), except for Equation (4.8) which is the material derivative of the definition of the geopotential.

The equation of state

$$p = p_0(R_d\theta/p_0\alpha)^\gamma, \tag{4.9}$$

and the diagnostic relation for the inverse density

$$\partial_\eta \phi = -\alpha\mu. \tag{4.10}$$

$\gamma = c_p/c_v = 1.4$ is the ratio of the heat capacities for dry air, R_d is the gas constant for dry air, and p_0 is the reference pressure. F_U, F_V, F_W and F_Θ represent forcing terms arising from model physics, turbulent mixing, spherical projections and the earth's rotation.

The subscripts x, y, and η in the equations above denote differentiation. $\nabla \cdot \mathbf{V}a = \partial_x(Ua) + \partial_y(Va) + \partial_\eta(\Omega a)$ and $\mathbf{V} \cdot \nabla a = U\partial_x a + V\partial_y a + \Omega\partial_\eta a$ where a represents a generic variable.

When moisture is included, the equation can be written in the form

$$\eta = \mu_d^{-1}(p_{dh} - p_{dht}), \tag{4.11}$$

where μ_d is the mass of dry air in a column. p_{dh} represents the hydrostatic pressure of the dry atmosphere and p_{dht} represent the hydrostatic pressure at the top of the dry atmosphere. From this the flux variables will be in the form

$$\mathbf{V} = \mu_d \mathbf{v} = (U, V, W),\ \Omega = \mu_d \dot{\eta},\ \Theta = \mu_d \theta. \tag{4.12}$$

When using these definitions the moist Euler equations can be written as

$$\partial_t U + (\nabla \cdot \mathbf{V}u) + \mu_d \alpha \partial_x p + (\alpha/\alpha_d)\partial_\eta p \partial_x \phi = F_U \tag{4.13}$$

$$\partial_t V + (\nabla \cdot \mathbf{V}v) + \mu_d \alpha \partial_y p + (\alpha/\alpha_d)\partial_\eta p \partial_y \phi = F_V \tag{4.14}$$

$$\partial_t W + (\nabla \cdot \mathbf{V}w) - g[(\alpha/\alpha)\partial_\eta p - \mu_d] = F_W \tag{4.15}$$

$$\partial_t \Theta + (\nabla \cdot \mathbf{V}\theta) = F_\Theta \tag{4.16}$$

$$\partial_t \mu_d + (\nabla \cdot \mathbf{V}) = 0 \tag{4.17}$$

$$\partial_t \phi + \mu_d^{-1}[(\mathbf{V} \cdot \nabla\phi) - gW] = 0 \tag{4.18}$$

$$\partial_t Q_m + (\nabla \cdot \mathbf{V}q_m) = F_{Q_m}. \tag{4.19}$$

The diagnostic relation for the equation of state and the inverse density becomes

$$p = p_0(R_d\theta_m/p_0\alpha_d)^\gamma \tag{4.20}$$

and

$$\partial_\eta \phi = -\alpha_d \mu_d. \tag{4.21}$$

$\alpha = \alpha_d(1 + q_v + q_c + q_r + q_i + ...)^{-1}$ where the indexes symbolise the mixing ratios for water vapour, cloud, rain and ice. $\theta_m = \theta(1+(R_v/R_d)q_v) \approx \theta(1+1.61q_c)$ and $Q_m = \mu_d q_m$ where $q_m = q_v, q_c, q_r, q_i, ...$.

The governing equations on their final form defines perturbation variables to reduce truncation errors in the horizontal pressure gradient calculations and machine rounding errors in the vertical pressure gradient and buoyancy calculations. Effects like map projection and Coriolis are also taken into account in the final form of the equations.

4.1.2 Time discretization

A time-split integration scheme is being used in the ARW solver. The reason for this is the wide range of frequencies (wavelengths) in the atmosphere. The frequency modes are split into a low- and a high-frequency mode. The third order Runge-Kutta (RK3) time integration scheme is used to integrate the slow or low-frequency modes. The higher frequency acoustic modes on the other hand are integrated over shorter timesteps to maintain numerical stability. This time-splitting method, which is an explicit numerical scheme is used to improve computational efficiency. Both of the integrations are limited by the Courant number ($u\Delta t/\Delta x$).

4.1.3 Spatial discretization

The ARW solved uses Arakawa's C grid staggering for the variables (Figure 4.3). Velocities and the thermodynamic variables are staggered one-half grid length from each other. The point where θ is located is denoted the name mass points. The location of u, v and w are defined as u points, v points and w points. Not shown in the figure is η which is defined at the mass points on the discrete grid, the geopotential, ϕ, which is defined at the w points, and the moisture variables q_m which are defined at the mass points. The diagnostic variables used in the model, like pressure p and inverse density α are computed at the mass points. The grid lengths Δx and Δy are constants in the model formulation. The vertical grid length $\Delta\eta$ is not a fixed constant.

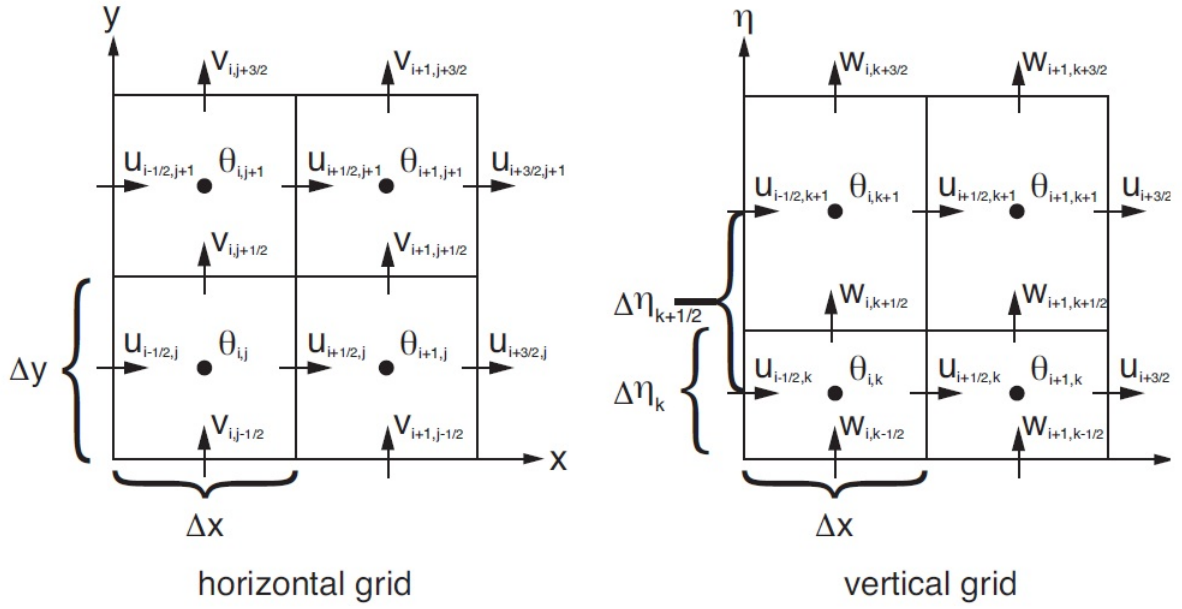

Figure 4.3: The horizontal and vertical grid that is used in the ARW dynamical solver for the Arakawa's C grid staggering (Skamarock et al., 2008).

4.1.4 Initial conditions

For real-data cases a preprocessing system called WRF Preprocessing System (WPS) is used to create complete 3-dimensional snapshots of the atmosphere for a chosen area at different times. Inside the WPS the projection type, location of the globe, number of grid points, nest locations and grid distances, which is the physical grid, are defined. Then static fields (terrestrial data) are interpolated to the chosen domain. Meteorological data is then horizontally interpolated onto the grid. The output data contain 3-dimensional fields of temperature in Kelvin, relative humidity and the horizontal components of momentum, 2-dimensional static terrestrial fields and 2-dimensional time dependent fields that include surface and sea-level pressure, layers of soil temperature and soil moisture, snow depth, skin temperature, sea surface temperature and a sea ice flag. This data is then used as input data for the real-data preprocessor, called real, in the ARW solver to generate initial and lateral boundary conditions for the model. The ARW real-data preprocessor interpolates vertically downwards for each column of the input pressure data.

4.1.5 Boundaries

The specified zone and the relaxation zone are the two zones that are specified in the coarse grid by the lateral boundary condition. The specified zone gets the information from the WPS, which has information about horizontal wind components, potential temperature, humidity and perturbation fields that are given on all four sides of the coarse domain. The relaxation zone is where the model is nudged or relaxed towards the large scale field. There can be smaller domains with higher resolution inside the coarse domain, and these are called nested grids. The nested grids have their information from the parent domain.

4.1.6 Spectral nudging

Spectral nudging is a dynamical downscaling method (Radu et al. 2008; Storch et al. 2000), which forces the large scales in the whole domain, not only at the lateral boundaries, to be influenced by the driving model information (Waldron et al., 1996). Smaller scales on the other hand are left to run freely, so that the model can develop small scale features that is consistent with the large scales (Radu et al. 2008; Miguez-Macho et al. 2004). In our case the nudging is also confined to the higher levels of the atmosphere, so that atmospheric variables in the lower troposphere, especially in the boundary layer, are able to run freely and adjust to the geographical properties of the surface (Storch et al., 2000). The different dynamical parameters that can be nudged in spectral nudging are pressure, specific humidity, horizontal wind velocities and temperature (Radu et al., 2008).

A well known phenomenon when using Regional Climate Model's (RCM) is that in many cases the RCM has a tendency to produce an internal deviation in the large scale fields between the simulation and the driving model information (this is often mentioned in the papers where spectral nudging is evaluated/used). This unwanted deviation is making it difficult at the boundaries where input and output data meet. Due to this, spectral nudging was introduced. Miguez-Macho et al. (2005) and Radu et al. (2008) are some of the studies that have found that this unwanted internal deviation is strongly reduced by the use of spectral nudging. Miguez-Macho et al. (2004) also found out that the spectral nudging is causing the model to no longer be dependent on the size and the position of the domain. This was also seen in the Alexandru et al. (2009) paper. The possible problems by using sprectral nudging on RCM's have not been fully established, and different papers give different results. The general agreement however, from those papers mentioned in this section, is that spectral nudging makes the variabilities of the

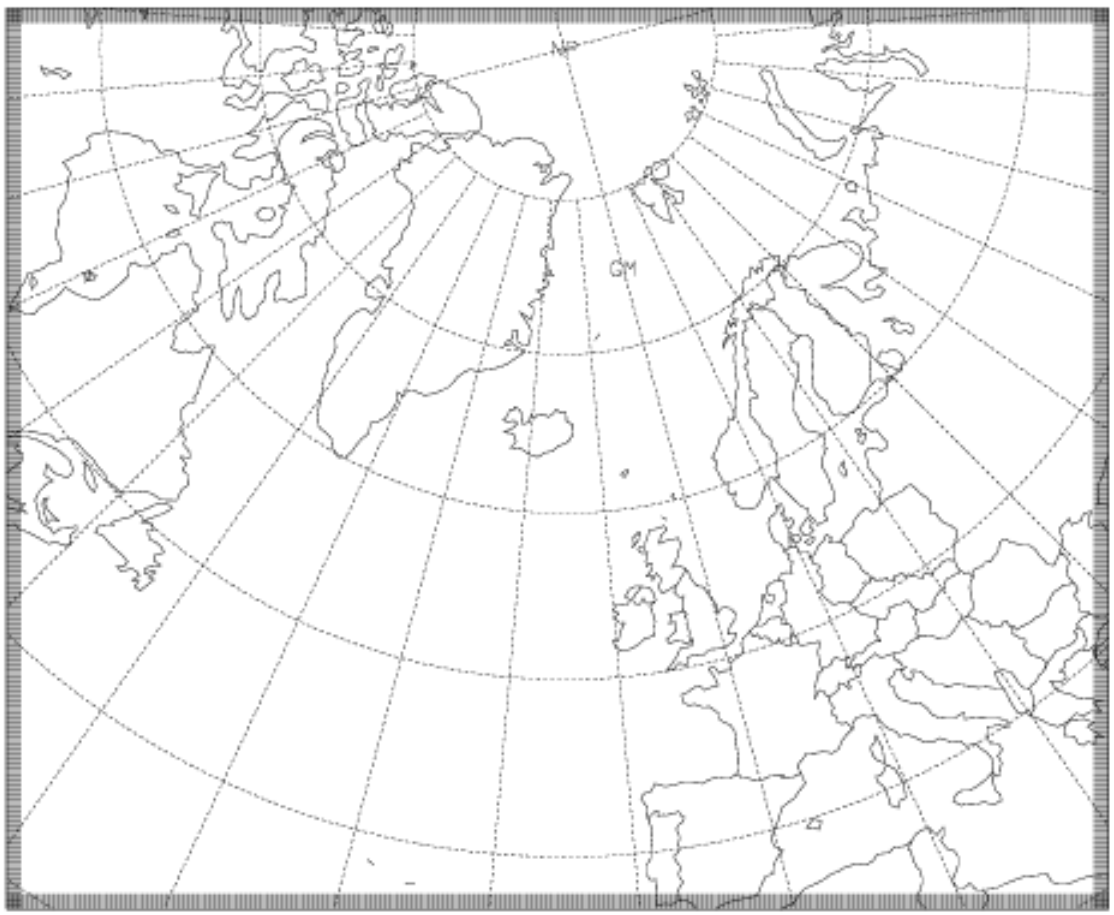

Figure 4.4: The domain with a 10 km horizontal grid solution used in the WRF simulations.

large scale system smaller inside the domain and causes the model to be less dependent on the position and size of the model domain.

4.2 The setup of the model

Version 3.2.1 of the WRF model has been used. The horizontal domain is 6720 km in the east-west direction and 5490 km in the north-south direction with a grid resolution of 10 km (Figure 4.4). The atmosphere is divided into 40 vertical levels that reach up to 50 hPa. The run time was about 15 days, where the first 14 days are prior to the extreme precipitation date (Figure 4.5). The spectral nudging is chosen quite high. Wavelengths above 672 km in the north-south direction and 686 km in the east-west direction are being controlled by the reanalysis data. This nudging is only applied for the wind and geopotential height fields and not for temperature and humidity. The number

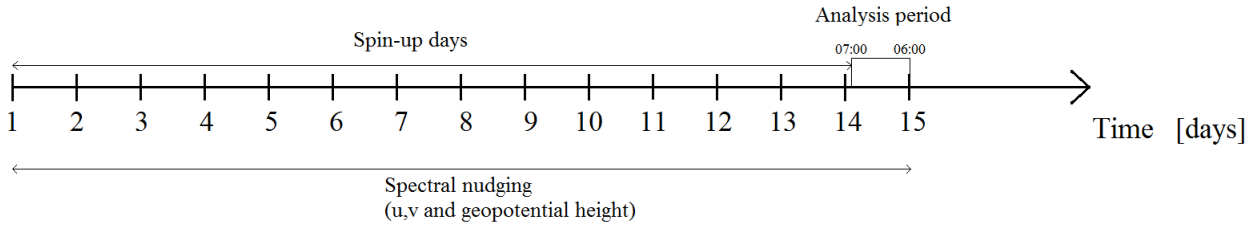

Figure 4.5: A simple description of the model setup. The first 14 days are spin-up days. The analysis period is defined as the time between 07:00-06:00, so the daily precipitation occur between 6 UTC to 6 UTC for the given extreme precipitation date. Spectral nudging of the horizontal wind components (u and v) and the geopotential height occurs throughout the entire run time of 15 days.

of relaxation points creating the boundary is of 4 grid points.

The different physical schemes chosen for this thesis are listed in Table 4.1. For information on the different physical schemes look at chapter 8 in Skamarock et al. (2008).

Table 4.1: The physical schemes used in the setup of the model

Categories of Physics	Name of chosen scheme
Micro-physics scheme	WSM 3-class
Cumulus Parameterization scheme	Kain-Fritsch
Planetary Boundary layer scheme	YSL PBL
Land-surface model	Noah Land Surface Model
Radiation scheme	RRTM longwave and MM5 shortwave(Dudhia)

For all of the simulations, 6 hourly ERA INTERIM reanalysis data from the European Center for Medium Range Weather Forecast (ECMWF) were used as boundary forcing. This dataset is the latest global atmospheric reanalysis produced by ECMWF, and reaches back to 1. January 1979[5]. The reason for using these reanalysis instead of ERA-40 reanalysis is higher resolution both horizontally and vertically, and a better representation of the hydrological cycle (Dee et al., 2011).

4.3 Description of the simulations

One winter, one spring and one fall extreme precipitation event have been selected. These events had a high percentage of stations experiencing extreme precipitation. One control run and two sensitivity simulations have been done for each of the chosen precipitation

[5]http://www.ecmwf.int/research/era/do/get/era-interim

events. A uniform change in the SST values of 2 ^{o}C higher and 2 ^{o}C lower for the entire domain was applied to the boundary conditions for the model run creating the two sensitivity simulations. An uniform change of the SST values could result in a different spin-up and change the path of the large scale system. To prohibit a change in the position of the large scale circulation, spectral nudging was introduced in all of the model runs. Temperature and humidity fields in the model was not nudged, hence production of precipitation could develop more freely. The strength of the spectral nudging was tested by comparing the surface pressure between the sensitivity simulations and their respective control runs. The reason for simulating the events with 2 ^{o}C higher and 2 ^{o}C lower SST with nudging, was to try and establish what would happen to the distribution and intensity of the precipitation if the large scale system was still located in the same position, while the surface boundary condition was changed.

The large domain size was chosen to be able to represent the synoptic features over the North Atlantic (Heikkilä et al., 2010). Heikkilä et al. (2010) found that a grid spacing of 10 km is large enough to be able to represent the regional effects and to get a good enough representation of the topography to reproduce daily precipitation amounts for the west coast of Norway. Such a high resolution over such a large domain costs both computing time and storage space. A water particle usually has a lifetime of 10-15 days in the atmosphere (Wallace & Hobbs, 2006). Therefore, there was no need for a runtime longer than 15 days, where the days prior to the analysing period where spin-up days (Figure 4.5).

Chapter 5

Observational study

5.1 Observations

The area that will be studied in this thesis include Møre og Romsdal, Sogn og Fjordane, Hordaland and part of Sunnhordaland which have been defined under the names Region 1, Region 2 and Region 3 (Figure 5.1). Days that exceeds the 99.5 percentile threshold for the intensity of daily precipitation during the time period 1961-2009, will be defined as an extreme precipitation event. Daily precipitation is defined from 6 UTC to 6 UTC for the given date. The west coast of Norway experiences extreme precipitation due to intense extratropical cyclones. Therefore, days where several of the stations in the defined area experience extreme precipitation will be viewed as one extreme event. This is to ensure that the event is not a purely local effect but a result of large scale pressure and frontal systems. If the focus was on extreme precipitation on the east side of the Norwegian mountain range this would be quite different. This has to do with the fact that most of the extreme precipitation cases there are due to small scale convection, especially during the summer months.

The original dataset contained daily precipitation observations from 1961 to 2009 for 1090 stations distributed all over Norway. Not all of these stations have observations throughout this period. Therefore the number of stations will be lower for any given period. After cutting the dataset to only contain those stations that are within the given area, and to only consider stations that have datasets with more than 80 % data over the 1961-2009 period, 114 stations were left. The reason for only considering stations with more than 80 % data is so that the 99.5 percentile would be as accurate as possible. Information on the 114 stations can be found in Appendix A.1

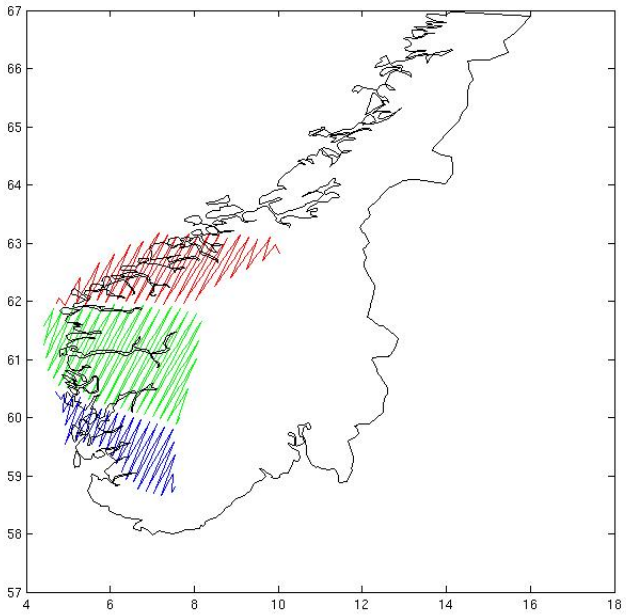

Figure 5.1: The chosen area, where the red area is Region 1, Region 2 is defined by the green color and the blue area is Region 3.

Stations observing precipitation have been relocated in some cases. To get a continuous time series a possible solution is to "merge" the data sets. Observational data is merged only if

- the stations are located less than 4 km from each other.
- the datasets for the different stations overlap for a certain time period, at least a year.
- the correlation between the data is higher than 0.9.

When these criteria are met, the shortest record of observations is corrected by using monthly correction factors created based on the period with overlapping between the stations. By calling two stations A and B, where A has the shortest data record, the corrected record, $P_{corr,A}$, can be calculated by

$$P_{corr,A} = P_{obs,A}\frac{\bar{P_{obs,B}}}{\bar{P_{obs,A}}} \tag{5.1}$$

where the $P_{obs,A}$ is the observed precipitation for station A, and $\bar{P_{obs,A}}$ and $\bar{P_{obs,B}}$ is observed monthly mean of station A and B for the overlapping period.

Table 5.1: The 50 most extreme precipitation events from 1960 to 2009 for the merged dataset. They are organized after percentage of stations with observations experiencing extreme precipitation for that given date. The first column states how many of the stations that have observed a daily precipitation amount over the 99.5 percentile threshold for the 1961-2009 time period during the given events in column 3. Column 2 states the percentage of the stations that have observed extreme precipitation during the given events, of the stations that have a recording of the event. The last column states the most extreme daily precipitation that was recorded during the given events.

Number of Stations	Percentage of Stations [%]	Date	Max precipitation [mm/day]
84	74	21 Jan 1983	140.2
67	74	15 Nov 2005	223.0
75	66	9 Mar 1983	172.8
71	63	11 Jan 1992	156.2
66	62	18 Nov 1967	117.2
54	61	14 Sep 2005	160.0
65	59	2 Mar 1997	175.0
65	58	21 Nov 1980	129.7
65	57	4 Feb 1993	138.7
61	55	31 Mar 1997	158.2
59	55	18 Dec 1966	162.2
46	55	12 Jan 2009	121.6
52	53	15 Nov 2004	195.0
57	51	27 Oct 1995	184.6
57	51	14 Dec 1991	162.0
54	48	29 Nov 1999	135.8
54	47	4 Dec 1986	102.2
50	47	6 Feb 1967	169.6
45	47	5 Dec 2004	161.0
53	46	28 Jan 1989	142.5
52	46	3 Nov 1971	124.0
41	46	1 Nov 2007	135.6
48	43	10 Apr 1999	143.5
48	42	27 Oct 1983	131.6
48	42	27 Dec 1975	151.2
47	42	4 Feb 1999	140.6
42	42	12 Nov 2004	144.0
47	41	19 Dec 1993	123.5
47	41	26 Oct 1983	138.1
44	41	15 Mar 1967	149.9
44	40	1 Jan 1984	152.2
45	39	26 Feb 1976	130.3
37	39	7 Jan 2005	152.3
42	38	16 Feb 1999	121.2
41	38	15 Dec 1967	125.3

39	38	27 Sep 1963	150.5
42	37	11 Nov 1986	129.2
41	36	30 Oct 1983	138.6
41	36	9 Dec 1980	133.0
40	36	9 Feb 1998	132.1
39	36	7 Sep 1966	162.4
40	35	19 Oct 1970	106.5
39	34	7 Oct 1975	109.3
38	34	21 Mar 1993	144.3
38	34	23 Feb 1992	125.0
38	34	21 Feb 1973	108.8
38	33	9 Oct 1992	175.0
37	33	3 Jan 1992	131.0
37	32	19 Jan 1989	156.9
36	32	15 Dec 1992	127.5

In this thesis both data sets with and without "merged" data have been used. Since the merged and nonmerged datasets give quite similar results, only the results from the merged data sets will be presented here.

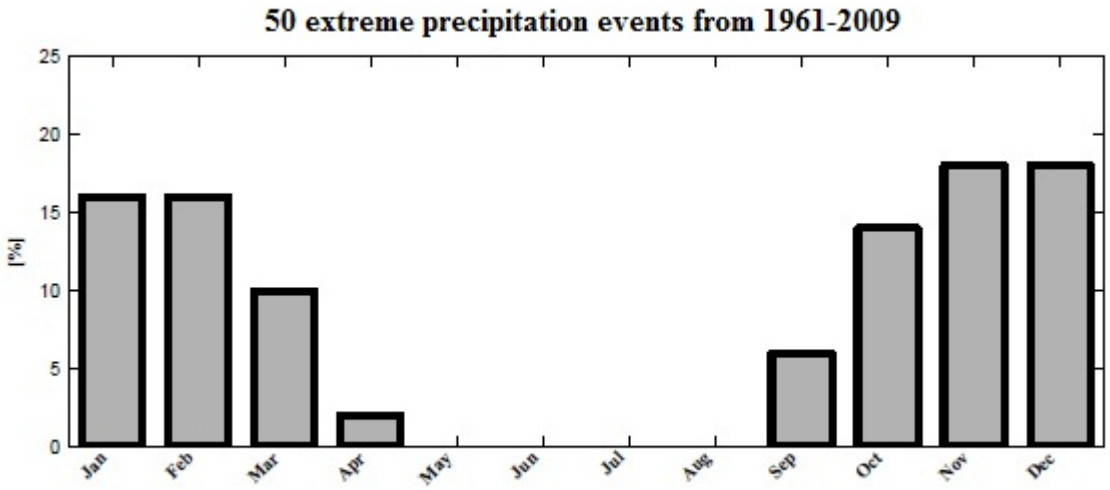

Figure 5.2: Monthly distribution (%) of the 50 most extreme precipitation events between 1961 and 2009 for the merged data set.

After taking the 99.5 percentile on the remaining data from the 114 stations, it was possible to find those dates that had extreme precipitation over several stations. The 50 dates that had the highest percentage of stations with extreme precipitation are listed in Table 5.1 with highest percentage of stations for a given event at the top. An extreme precipitation event might not occur in the defined daily precipitation date. Therefore

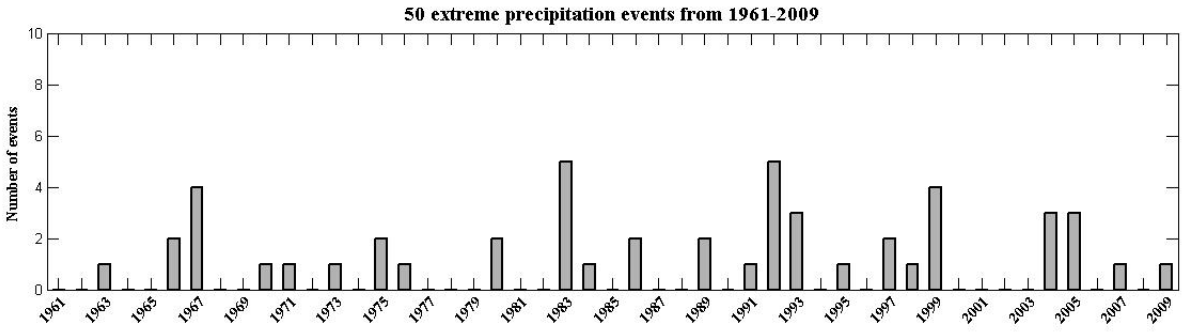

Figure 5.3: Yearly distribution of the 50 most extreme precipitation events between 1961 and 2009 for the merged data set.

the average value of the daily precipitation of two and two days was also evaluated to check if the same dates were seen as the 50 most extreme precipitation dates as those in Table 5.1. Since most of the dates in Table 5.1 were also located in the 50 most extreme daily precipitation events for the average value between two days, the average daily precipitation values will not be further investigated. Interested readers can find the table of the 50 most extreme daily precipitation events for average daily values over two days in Appendix B.1.

To get a picture of the seasonality and variability of the extreme events the monthly frequency (Figure 5.2) and yearly frequency (Figure 5.3) have been plotted. From the monthly distribution of the events (Figure 5.2) one can clearly see that none of the 50 most extensive events happened between May and August. Most of the events were happening during late fall and winter which correspond quite well with what was expected, due to strong temperature gradients during this period creating more intensive extratropical cyclones (Bengtsson et al., 2009). Condensation also occurs more easily in "colder" air since the air needs to contain less humidity or to be cooled less to reach saturation, than warmer air which can contain much more humidity and therefore potentially more precipitation. A more surprising and interesting result was the large percentage of events during March, especially compared to September. When it comes to the yearly distribution there are no signs of increased amounts of extreme precipitation events seen from year to year (Figure 5.3). Several climatological studies (e.g. Caroletti & Barstad (2010); Bengtsson et al. (2009); Trenberth (1999); Pall et al. (2007)) have shown that in future warmer climate, extreme precipitation events will occur more frequently. There are no long term trends in the number of events to give any indication to whether extreme precipitation events will happen more frequently in the future. It is important to remember that this figure does not deny this either, but does not present proof that this is the case. Another important aspect is that the events are the 50 most extreme events between

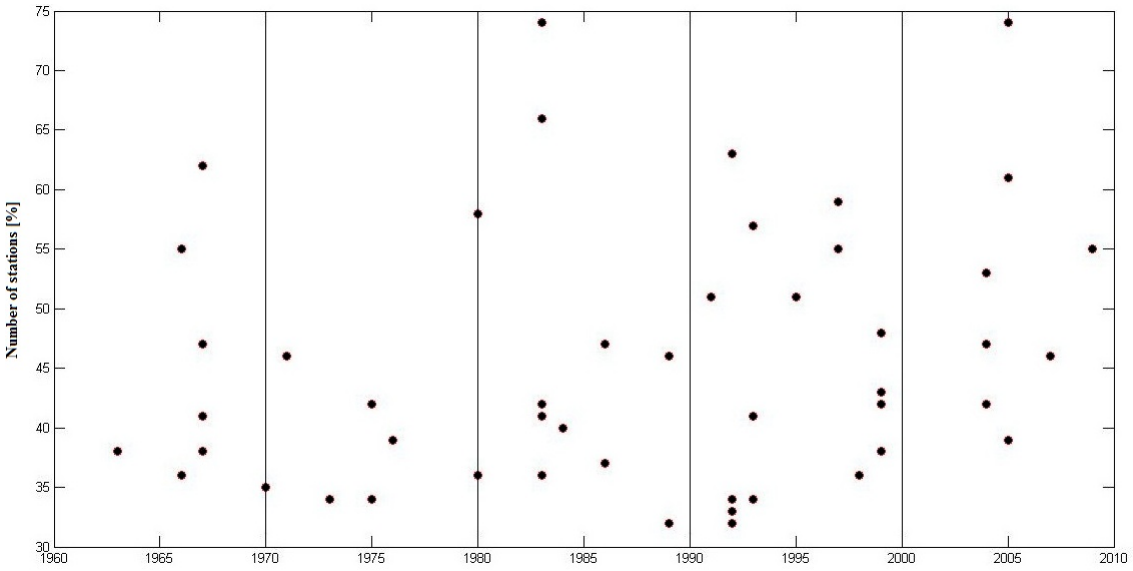

Figure 5.4: The percentage of stations that observed extreme precipitation for a given event over the years 1961-2009. Black lines are used to divide the time period up into ten year periods. The 50 events are indicated by the black dots.

1961 and 2009 when it comes to affecting more than one local area. These events have been chosen in a way that they do not include extreme local events that could have been a result of small scale convective systems. Therefore it is possible that Figure 5.3 could have shown some trends that would have backed up previous studies on more frequent extreme precipitation if local extremes were introduced. 1983 and 1992 had the highest number of events in this time period.

A ten year distribution of the events indicate a trend from the period 1970 to 1999. The 70's have only 6 of the most extreme events while the 80's have 12 and the 90's have 17 events (16 on the Figure 5.4 but there are two events in 1992 having the same percentage of stations). From this figure there seems to be no significant pattern when it comes to the percentage of the stations that experienced extreme precipitation for each of the events. The years before 1980, and especially the 70's, have almost none of the events with the highest percentage. The monthly distribution over the ten year periods is shown in Figure 5.5. The 30 year trend from 1970 to 1999 is also visual for at least the winter and spring events with an increase in the amount of extreme precipitation events occurring. The fall events are strongest represented during the 80's and the 00's.

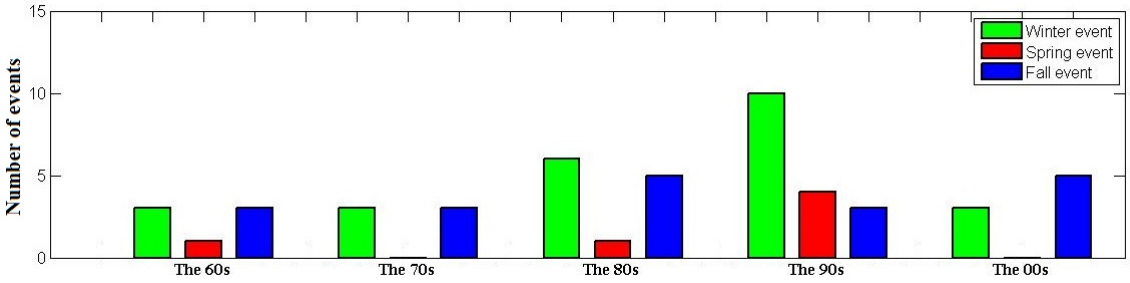

Figure 5.5: The monthly distribution in ten year periods for the 50 most extreme precipitation events.

5.2 Synoptic situation during the extreme events

To get a better understanding on why exactly these 50 events stated in Table 5.1 experienced extreme precipitation on the west coast of Norway, it was necessary to look at the synoptic scale flow of the events. The synoptic system was looked at by using Sea Level Pressure (SLP) data from the Modern Era Retrospective-analysis for Research and Applications (MERRA) reanalysis, for events that had over 40 % of the stations which experienced extreme precipitation. These reanalysis are developed to support NASA's Earth Science, and give hourly three dimensional atmospheric analysis with a spatial resolution of 0.5 degrees in latitude, and 0.67 degree in longitude and up to 72 vertical layers. These reanalysis cover the period between 1979 and 2011[6]. As not all data was available at the time of this analysis, the MERRA reanalysis could only give values of the SLP for only 35 of the 50 most extreme precipitation events. The SLP data for all of the 35 events have two things in common. The low- and high-pressure systems are located so that warm humid air from the south is mixed with colder air from polar areas, and the synoptic scale flow is never coming from an eastern direction. Thus, the isobars and resulting wind system always have a western component. These results can be viewed in Figure 5.6. Figure 5.6a and Figure 5.6b represents events having isobars with a northwestern component on the west coast of Norway. Twelve of the events had this type of synoptic scale flow. The fourteen events with more or less only a western component are represented by Figure 5.6c and Figure 5.6d. Most of the events have this type of synoptic scale flow. The last two figures in Figure 5.6 represent the last nine events which have a more southwestern component for the synoptic scale flow. The gradient of the isobaric lines indicates the strength of the resulting wind field. Stronger gradient (tighter lines) results in stronger winds. Comparing the synoptic scale flow from Figure 5.6 with the intensity of the given event, and the number of stations that experienced extreme precipitation, this seems to be the case. A deeper investigation on the strength of the large

[6]http://gmao.gsfc.nasa.gov/research/merra/

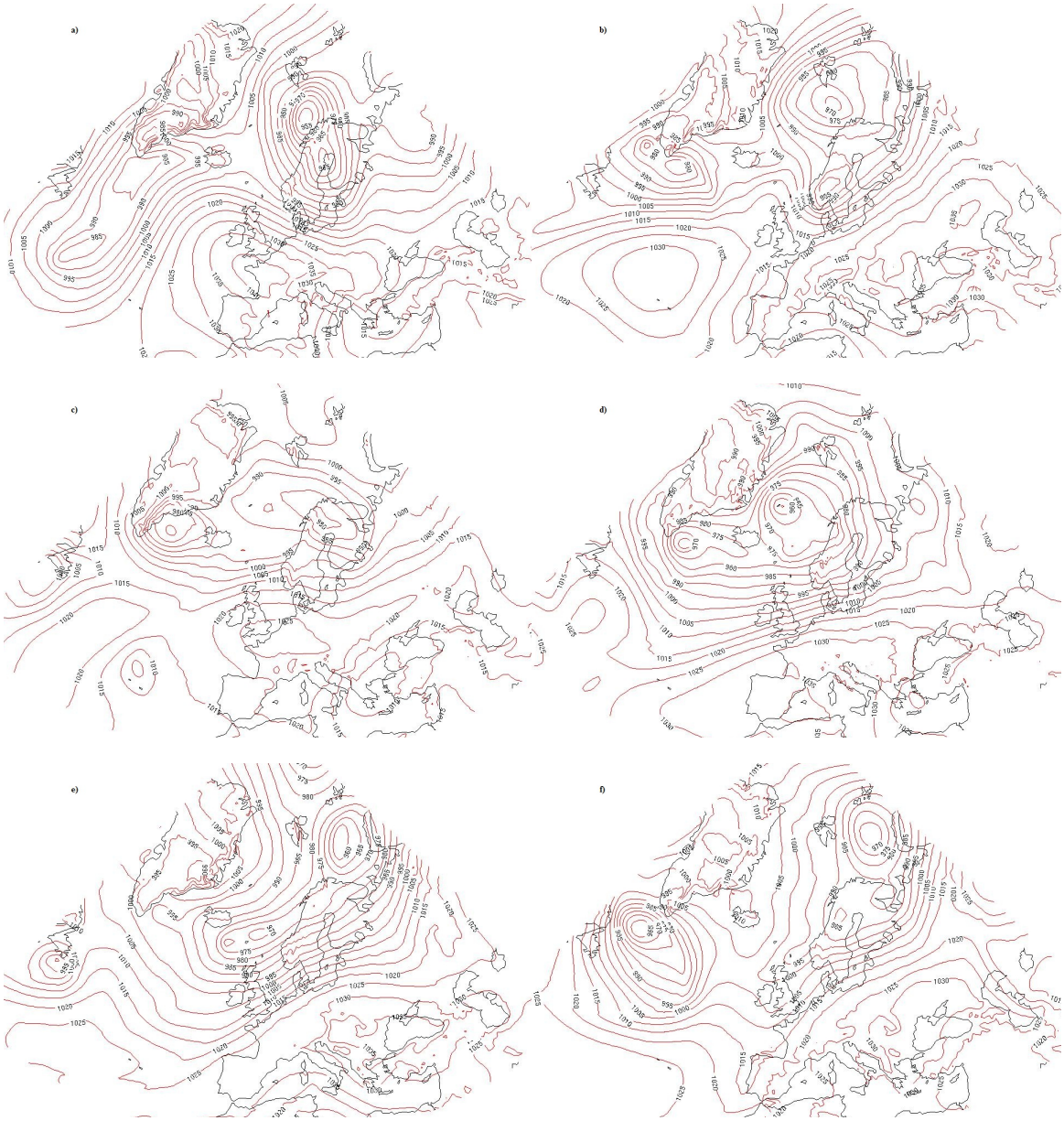

Figure 5.6: The large scale system by representing the Sea Level Pressure from the MERRA reanalysis for a) 21. January 1983, b) 29. November 1999, c) 31. March 1997, d) 7 January 2005, e) 12. January 2009 and f) 11. November 1986 at 06.00 UTC.

scale flow and the resulting wind system will not be further looked at for this thesis. For interested readers, the remaining SLP fields from the MERRA reanalysis are located in Appendix C.-43.

5.3 Conclusions

The analysis has identified the 50 most extreme precipitation events on the Norwegian west coast, considering the highest percentage of stations observing extreme daily precipitation between 1961-2009. The study showed large variations in number of events with an annual distribution, where 1983 and 1992 had the highest number of events (5 events each) during the time period. From a ten year perspective, large variations between the different decades were seen. The 1990s experienced the largest total number of events (17 events). The largest number of the winter and spring events was also experienced in the 1990s.

Most of the 50 extreme events occurred during the late fall and winter months. This result supports previous studies indicating that extreme precipitation on the west coast is related to intense extratropical cyclones during this period due to stronger horizontal temperature gradients (Bengtsson et al., 2009). Non of the most extreme daily precipitation events occurred during the summer months.

The synoptic situation during the extreme events indicated that extreme daily precipitation events only occur for events with a large scale flow orientated with no easterly component on the west coast of Norway. From a subjective view, it seemed like the synoptic scale flow could be divided into three types, with a northwestern (12 events), a western (14 events) and southwestern (9 events) component of the large scale synoptic flow on the west coast of Norway. The study also seems to indicate that the air arriving at the west coast of Norway is a mix between cold Arctic air and warm humid air from the south.

Chapter 6

Three case studies

The three case studies chosen for deeper investigation are listed in Table 6.1. All three events had a high percentage of stations experiencing extreme precipitation (Table 5.1). A general description of each of the extreme daily precipitation events will be presented by both MERRA reanalysis and the control run from the WRF model. As described in Section 4.3, the WRF model is also used to simulate the sensitivity of the three precipitation events to changed SSTs. Parameters such as specific humidity, vertical velocity, relative humidity (RH) and static stability is used to get a deeper insight in the different responses to the changed SSTs for the daily precipitation. The area of interest is the same as defined in Chapter 5 (Figure 5.1). To get a more detailed picture of the changes, the area is also divided into four cross sections (Figure 6.1). Only a few of these cross section figures are presented in the study, the rest are placed in Appendix D.

Table 6.1: Overview of the different simulation runs

	Control run	Two degrees higher SST	Two degrees lower SST
11 January 1992	control_jan	higher_jan	lower_jan
2 March 1997	control_mar	higher_mar	lower_mar
15 November 2005	control_nov	higher_nov	lower_nov

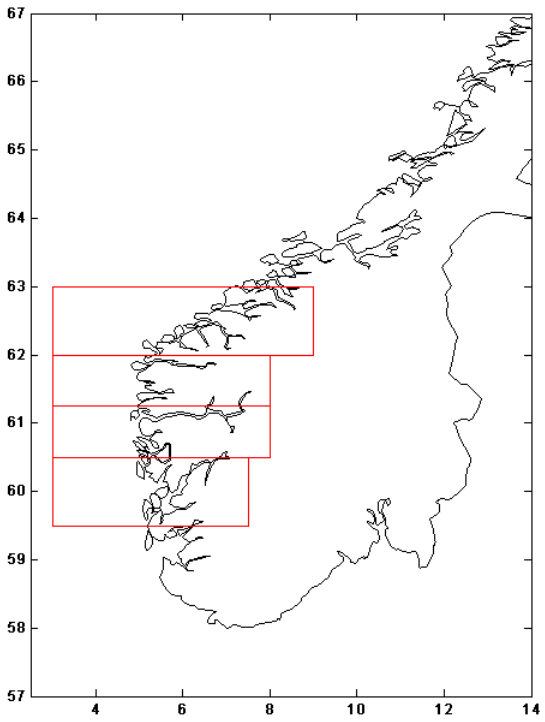

Figure 6.1: The four cross section areas. The box at the top is called Møre og Romsdal, the box beneath it is called North of Sognefjorden, beneath that again the is called South of Sognefjorden, and the box at the bottom is called Sunnhordaland.

6.1 The winter event: 11. January 1992

6.1.1 MERRA reanalysis

The synoptic pressure systems during the winter event are located in a region, where cold air from polar areas is drawn southward east of Greenland and mixed with warm and humid air from the south (Figure 6.2). The extratropical cyclone pushes the mixed air toward the west coast of Norway, causing the isobaric lines to almost be perpendicular to the coast. The large scale westerly flow results in enhanced orographic precipitation as the air is orographically forced over the complex terrain on the western side of Langfjella.

The distribution of the daily precipitation given by the MERRA reanalysis indicate most intense precipitation in coastal areas for Region 2 and more inland areas for Region 1 (Figure 6.3a). The observational data from the same time period indicates the highest precipitation amounts (values up to 85 mm/day) for the coastal areas in both Region 2 and Region 3. From a subjective point of view, the MERRA reanalysis seems to be able to reproduce the pattern but not the high precipitation values, especially those observed in the coastal areas. The horizontal resolution of the MERRA reanalysis is coarse. Hence,

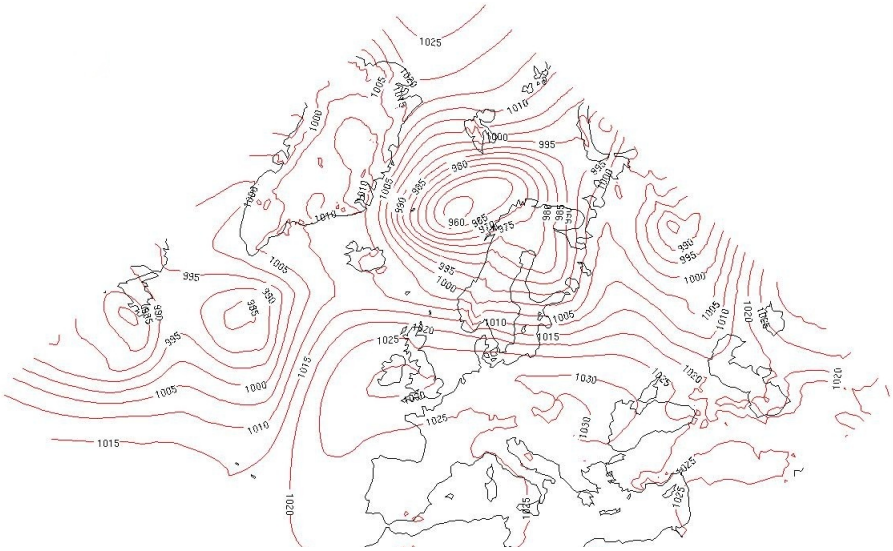

Figure 6.2: The large scale synoptic system by presenting the Sea Level Pressure (SLP) from the MERRA reanalysis at 06.00 UTC for the winter event (11. January 1992).

the reanalysis are not able to fully reproduce the topography on the west coast of Norway, and thereby the amount of precipitation. In addition to the problems of representing topographic effects, the coarse resolution of the MERRA reanalysis may not to be able to represent high precipitation values due to small-scale convection. Another possible effect could result from changes in friction between ocean and land areas. The change in friction from ocean to land could cause a reduction in the wind speed and a turning of the air flow. When these effects work together the air flow might converge resulting in a lifting of the air (Bergeron (1949); Godske et al. (1957)). If the air becomes saturated by the lifting, precipitation may form and fall in coastal areas. To quantify these results, the statistical validation measures MAE and MBE presented in Chapter 3 have been used (Table 6.2). With a MAE of almost 26 mm/day and an overall underestimation of 30 %, these statistical errors seems to support the subjective results presented above for the MERRA reanalysis.

Table 6.2: Values of the MAE and MBE for the predictions compared with the observations for the 114 stations located in the chosen area for the winter event (11. January 1992). The table represent both model data from the MERRA reanalysis, and model data from the control runs created by the WRF model.

	MAE [mm/day]	MBE [%]
MERRA reanalysis	25.6	-30.3
WRF model	16.7	-4.2

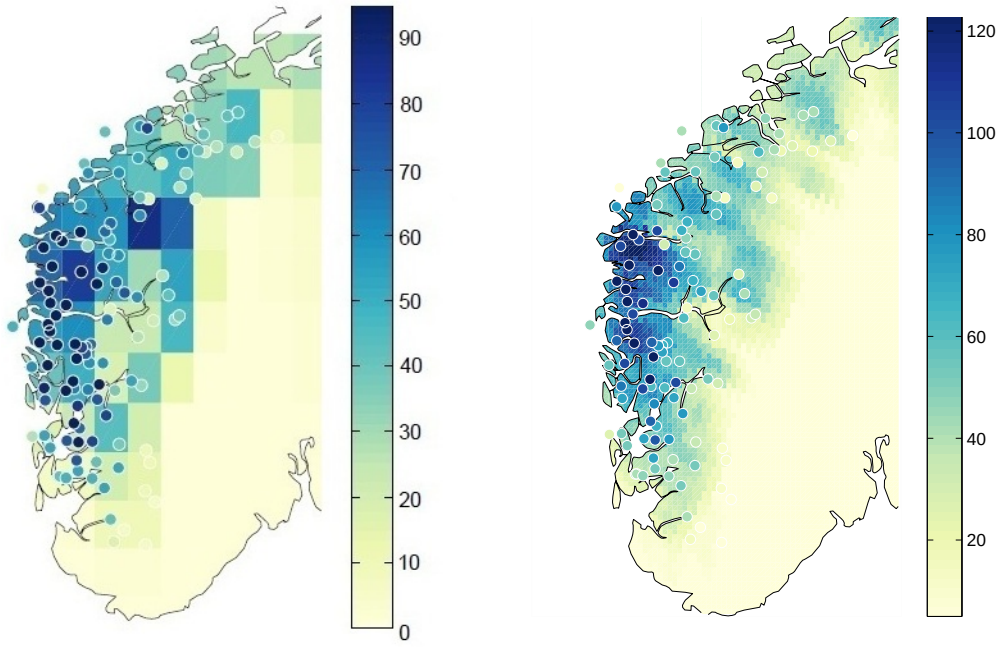

(a) MERRA reanalysis (b) WRF model

Figure 6.3: Daily precipitation distribution for the winter event (11. January 1992) created by a) the MERRA reanalysis and b) control run from the WRF model. Observational data are shown as circles. The colours represent the magnitude of precipitation.

6.1.2 WRF model

From a subjective point of view, when comparing the presentation of the daily precipitation for the winter event from the WRF model (Figure 6.3b) and the MERRA reanalysis (Figure 6.3a), one can see that the pattern is quite similar. The highest daily precipitation amounts are located in the coastal and central areas in Region 2 and decreases toward the inland mountainous areas. The main difference is the amount, where the WRF model is able to reproduce higher amounts of precipitation (values up to 140 mm/day) which was one of the main problems in the MERRA reanalysis due to its coarse resolution of the topography. The coastal areas also seem to be better represented than in the MERRA reanalysis. By checking the MAE and the MBE (Table 6.2), the WRF model was able to reproduce the winter event with higher accuracy than the MERRA reanalysis. With an overall underestimation in the amount of daily precipitation of 4 % compared to 30 % and a MAE of about 17 mm/day compared to 26 mm/day, the WRF model is able to reproduce the winter events reasonably well compared to the MERRA reanalysis.

From the cross sections of the control run (Figure D.-3 in Appendix D), the general result indicated the highest precipitation amounts in the coastal regions with decreasing amounts further inland. The largest amount was found in the cross section North of

Sognefjorden with daily precipitation amounts reaching up to 120 mm/day. The specific humidity decreases as it precipitate towards the top of the mountain range Langfjella. A general shift between the maximum vertical velocity and highest precipitation amount is shown in all four cross sections. This supports the theory of the time lag between condensation and observed precipitation, due to hydrometeor growth and fall speed of the precipitation.

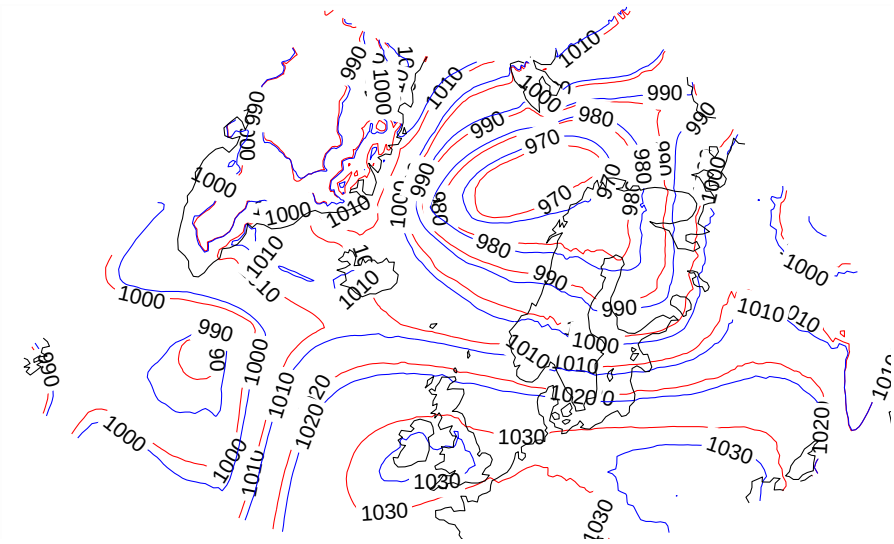

Figure 6.4: The Sea Level Pressure (SLP) fields for the control run (red line) and the sensitivity simulation (blue line) with increased SSTs for the winter event (11. January 1992).

As our model setup is designed to investigate the effect of changes in SST given the same location of the synoptic features, an important aspect was to see that the pressure systems were located in the same position for both the control and sensitivity simulations for each event. If this had not been the case, it would be much harder to compare the results from the control run and the sensitivity simulations for the three events. This has to do with the fact that the result of the different simulations may then be due to changed position of the lows instead of the thermodynamical effects of a change in the SST values. Figure 6.4 shows that the pressure systems were located almost at the exactly same place, for both the control run and the sensitivity simulation. The only observed change was in the depth of the pressure systems, with increased depth for the low pressure systems with the increased SST. The increasing depth of the extratropical cyclones does not prohibit any comparisons between the results, since the change in the depth of the pressure systems would not change the direction of the wind field as the gradient is the same. By changing the SST values one could change the available energy for the spin up of the large scale systems and therefore change the depth of it. The gradient between the isobaric lines

were almost the same causing no change in the strength of the wind field. One can also see from Figure 6.4 by comparing it with Figure 6.2, that the pressure systems are located at the same spot. In other words, the model was able to reproduce the same result as the MERRA reanalysis.

Two degrees higher SST

With increased SST values, a distinct percentage change in the distribution of the daily precipitation occur for the entire area (Figure 6.5a). In the coastal areas where some of the largest amounts of daily precipitation was located, a general decrease in the daily precipitation occurred. Further inland, in the more mountainous areas, a general percentage increase occurred with the increased SST. The largest percentage changes in daily precipitation seems to be located south of Sognefjorden. Areas closest to the mountain tops experienced the highest percentage increase in precipitation (over 40%), while the coastal areas in Region 3 (Figure 5.1) experienced the largest percentage decrease in daily precipitation (around 20%).

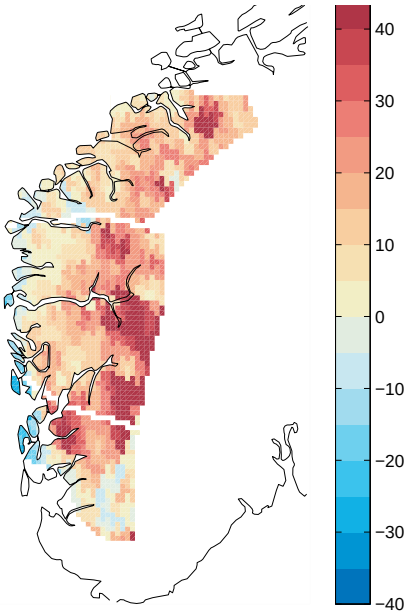

(a) Two degrees higher SST

Figure 6.5: Percentage change between the sensitivity simulation and the control run for the winter event (11. January 1992).

From the four cross sections (Figure 6.1) for the winter event, it was quite clear that there was a percentage decrease of around 20% in the daily precipitation in the coastal areas, and a quite strong percentage increase (up to 60%) in the more mountainous inland areas for all 4 areas (Figure 6.6). For interested readers can all four cross section be found in

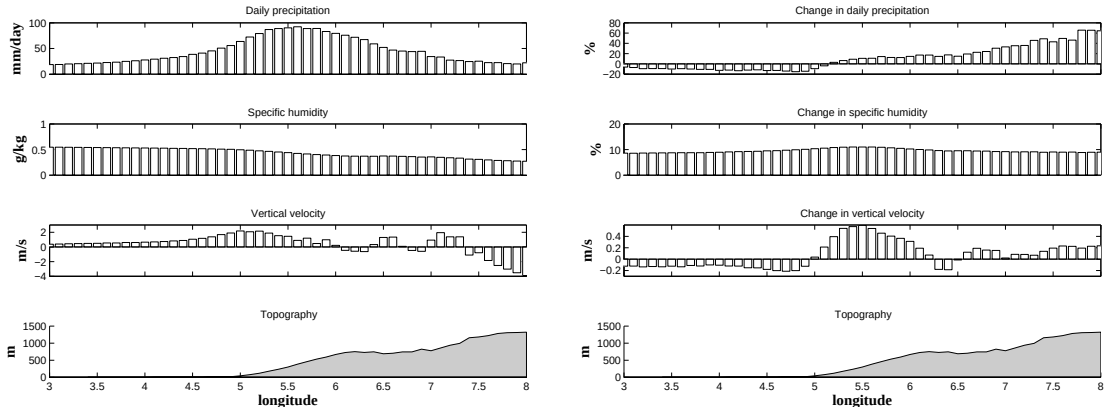

Figure 6.6: Cross section of the area South of Sognefjorden for 11. January 1992. The control run, control_jan, is on the left side while the change between the simulation higher_jan and control_jan is on the right side. Each of the bars in the different boxes for the 4 parameters represent an average for that specific longitude in the transect box. For the daily precipitation and the specific humidity the percentage change is shown, while the vertical velocity is found by taking the difference between the two runs to avoid extreme percentage values.

Figure D.-3 in Appendix D. The specific humidity had around a 10 % increase for all of the areas, and did not change much in the different cross section. The vertical velocity on the other hand changed a lot through the transect. From the ocean toward the coastal area the vertical velocity had a less positive value than control_jan, for then to have a general higher positive vertical velocity. Thus, it seems that with a 2 degrees higher SST the air had a smaller lifting prior to reaching land compared to the control run. The less adiabatic lifting may have caused less air to reach saturation so the production of precipitation is lowered and delayed. After hitting land the air is able to ascend even higher than in the control run.

As indicated from Figure 6.5, South of Sognefjorden and Sunnhordaland were the areas that experienced the strongest shift in the spatial pattern of daily precipitation. Therefore, the cross section South of Sognefjorden will be the only cross section evaluated further for the +2 simulation for the winter event (Figure 6.6). South of Sognefjorden experienced a decrease of around 20 % in coastal areas and an increase of around 60 % in the inland mountainous areas as its highest values. Considering the intensity of the precipitation in the South of Sognefjorden it is important to not only look at the percentage change but also the precipitation amount from the control run. The area of highest precipitation had an increase around 20 % (Figure 6.6), resulting in a large increase in mm/day.

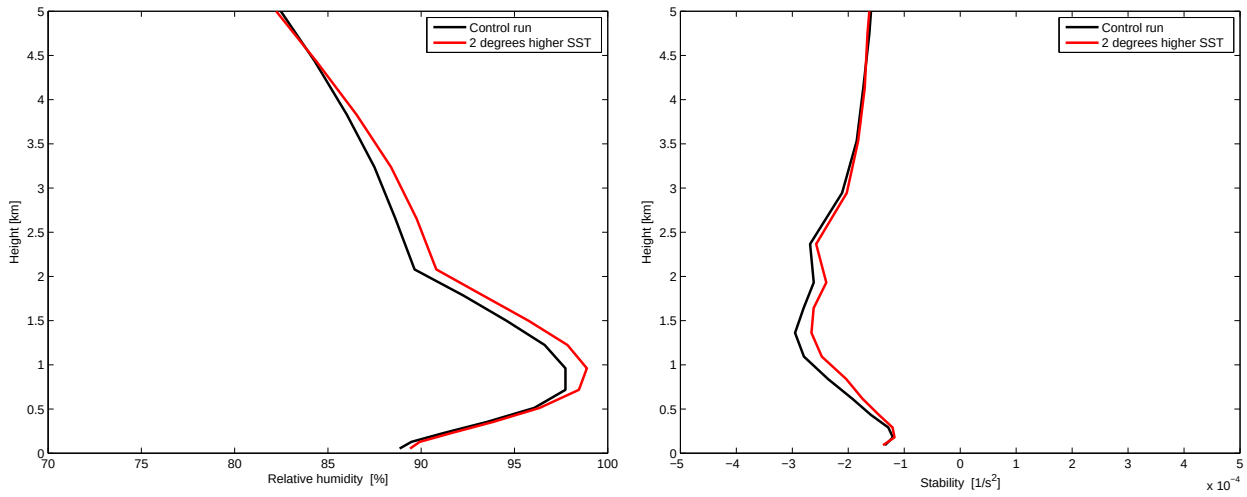

(a) Relative Humidity

(b) Static Stability

Figure 6.7: Vertical section of the average values of RH and Brunt Väisäla frequency (N^2) for the different vertical levels for the cross section South of Sognefjorden for the winter event (11. January 1992). Black line represent the control run, the red line represent the +2 simulation.

To get a better understanding of what happen to the air flow, vertical sections of the average RH and static stability (Brunt Väisälä frequency) for each vertical layer were made for the different cross sections. The vertical sections for South of Sognefjorden is presented in Figure 6.7. RH for the +2 simulation is generally higher than in the control_jan simulation for the lowest 5 km (Figure 6.7a). The air contains enough humidity, compared to the temperature increase, causing a higher percentage in RH. A result of increased RH is that humid air needs less cooling to reach saturation. The increase in the SST values also had an effect on the static stability of the atmosphere. For the lowest 5 km the air in the higher_jan simulation was in general more statically stable than control_jan, besides the lowest hundred metres and top kilometre of the 5 lowest kilometre (Figure 6.7b). This was also seen in the other three cross section areas, not shown in this thesis. Neither the vertical sections of the RH nor the static stability are able to explain the reduction of daily precipitation in the coastal areas.

The average change (%) for the different parameters represented and discussed above, for the four cross sections for the winter event, are presented in Table 6.3. This table gives the main result found for the differences between the +2 simulation and the control run. By increasing the SSTs the daily precipitation, specific humidity, vertical velocity and RH experience an average increase in percentage for both the four cross sections and the entire area. Even with an increase of around 10 % for the specific humidity and 15 % for the vertical velocity, the daily precipitation increase is only around 10 %. A possible

Table 6.3: Percentage change between the sensitivity simulation with increased SSTs and the control run for the different parameters daily precipitation, specific humidity, vertical velocity and relative humidity for the winter event (11. January 1992). The values are found by taking the mean for the region the west coast (WC), and the 4 transect regions, Møre og Romsdal (MR), North of Sognefjorden (NS), South of Sognefjorden (SS) and Sunnhordaland (SH). Specific humidity is found by taking the vertical average where the vertical layers are not weighted equally. The vertical velocity and relative humidity is found by taking the vertical average over the lowest 3 km.

	Daily precipitation [%]	Specific humidity [%]	Vertical velocity [%]	Relative humidity [%]
WC	8.8	9.5	13.8	0.4
MR	9.6	9.6	14.7	0.3
NS	6.1	10.0	11.1	0.6
SS	8.0	9.5	16.9	0.6
SH	12.5	9.0	15.3	0.4

reason for this is the general decrease in the instability with increased SST, presented earlier in this section. Decreasing the instability might suppress some of the vertical lifting resulting in air not being cooled enough adiabatically to reach saturation.

Two degrees lower SST

Due to numerical problems in the sensitivity simulation with decreased SST values (lower_jan), there are no results from this.

6.2 The spring event: 2. March 1997

6.2.1 MERRA reanalysis

The extratropical cyclone located north of Great Britain draws mixed humid air toward the west coast of Norway during the spring event (Figure 6.8). The resulting large scale flow hit the west coast of Norway with a south-westerly component. Enhanced orographic precipitation occur as the air gets orographically forced over the complex terrain.

With a south-westerly large scale flow, the highest precipitation amounts (values up to 70 mm/day) was found in central areas of Region 2 and Region 3 for the distribution of the daily precipitation given by the MERRA reanalysis (Figure 6.3a). The observational data had almost the same pattern as produced by the MERRA reanalysis for the spring event.

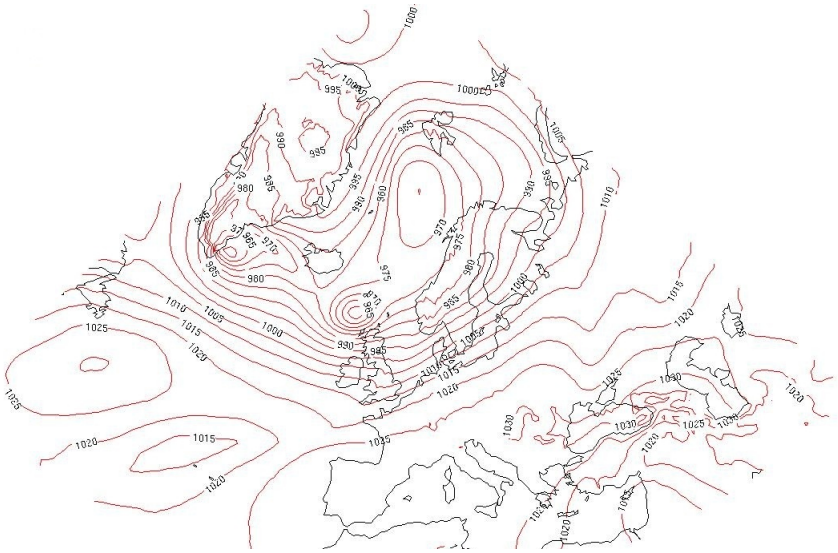

Figure 6.8: The large scale synoptic system by presenting the Sea Level Pressure (SLP) from the MERRA reanalysis at 06.00 UTC for the spring event (2. March 1997).

As indicated in Section 6.1.1 by the winter event, the horizontal resolution is too coarse for a good presentation of the complex topography on the west coast of Norway. As a result, the topography is less steep and therefore producing weaker enhanced orographic precipitation. As in the winter event (Section 6.1.1), the MERRA reanalysis is not able to fully recapture the precipitation amount in the coastal areas. The statistical validation measures MAE and MBE presented in Section 3 has also been used here to validate the results from the MERRA reanalysis data (Table 6.4). With an overall underestimation of 36 % and a MAE of 31 mm/day, the MERRA reanalysis is reproducing the spring event at the same accuracy as it did for the winter event.

Table 6.4: Values of the MAE and MBE for the predictions compared with the observations for the 114 stations located in the chosen area for the spring event (2. March 1997). The table represent both model data from the MERRA reanalysis, and model data from the control runs created by the WRF model.

	MAE [mm/day]	MBE [%]
MERRA reanalysis	31.0	-36.1
WRF model	23.1	-9.4

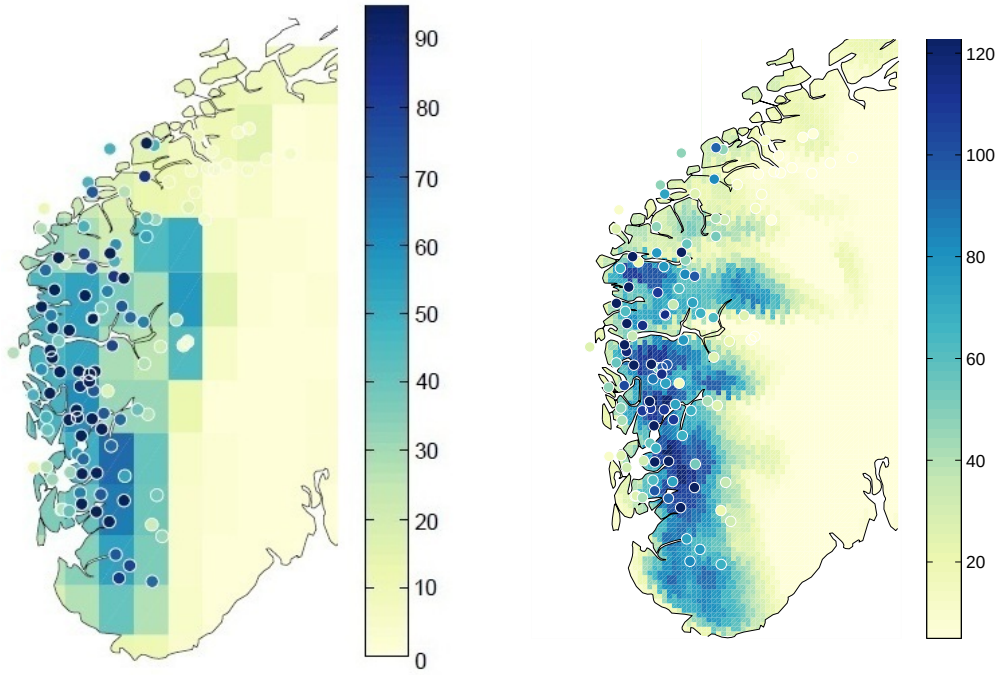

(a) MERRA reanalysis (b) WRF model

Figure 6.9: Daily precipitation distribution for the spring event (2. March 1997) created by a) the MERRA reanalysis and b) control run from the WRF model. Observational data are shown as circles. The colours represent the magnitude of precipitation.

6.2.2 WRF model

The WRF model is reproducing the spring event with general higher daily precipitation values for Region 2 and Region 3 (Figure 6.9b) compared to the reproduction by the MERRA reanalysis data (Figure 6.11b). From a subjective point of view, it seems like the WRF model is able to reproduce the event with higher accuracy when it comes to the highest daily precipitation rates, with values up to 130 mm/day compared to 70 mm/day (MERRA reanalysis). Table 6.4 verify this with an underestimation of only 9% with the WRF model compared to 36% from the MERRA reanalysis. MAE is also reduced with almost 8 mm/day with the WRF model.

More detailed representation of the extreme precipitation event is given with the four cross section (Figure 6.1). The general result from the cross sections of the control run indicate the highest precipitation values in the central areas at the top of the steepest slopes (Figure 6.12 and Figure 6.14). Sunnhordaland was the cross section that experienced the largest amount of daily precipitation (over 100 mm/day). A decrease in specific humidity toward the top of the mountain range was also observed in the cross sections for the spring event. The maximum vertical velocity seems to be located a certain distance prior

to maximum precipitation amount, which also was seen for the winter event.

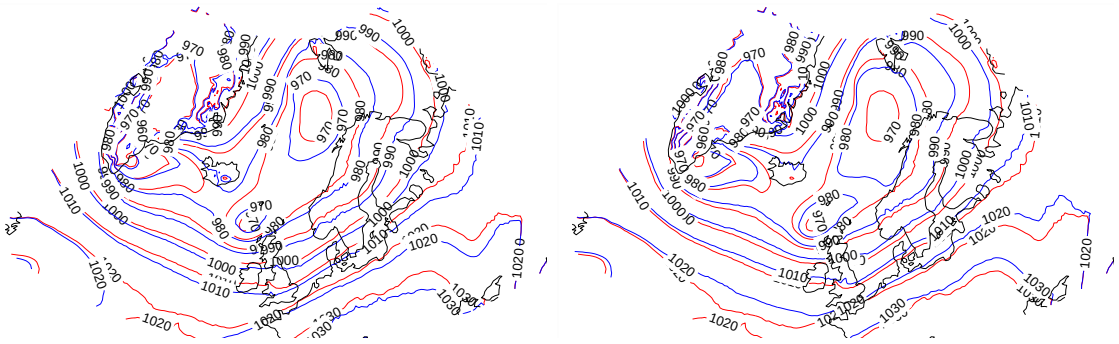

(a) Two degrees higher SST (b) Two degrees lower SST

Figure 6.10: Pressure fields for the control run (red line) and the sensitivity simulations (blue line) for the spring event (2. March 1997).

With the spectral nudging in the WRF model, the sensitivity simulations are able to obtain the same location for the pressure systems as the control run (Figure 6.10). The gradient between the isobaric lines did not seem to change, resulting in almost the exact same large scale synoptic flow for the control and sensitivity simulations for the spring event. The main difference between the control and sensitivity simulations is the depth of the pressure systems. For the lower SST simulations, the low pressure system was weaker than in the control run and the opposite was seen for higher SST values (Figure 6.10). By comparing this figure with Figure 6.8, one can also see that the pressure systems are located at the same spot. Hence, the WRF model is able to reproduce the same result as the MERRA reanalysis for the spring event.

Two degrees higher SST

Figure 6.10a indicates a shift in the spatial distribution of the daily precipitation with increased SSTs for the spring event. Most of the increased precipitation values is located in the coastal and inland areas of the west coast. These areas, especially Region 1, did not experience the largest precipitation values in the control run of the spring event. Decreasing precipitation seems to be located around the fjords and the central areas of the west coast, where some of the highest precipitation amounts was seen from the control run (Figure 6.9b). In other words, it seems like an increase in the SSTs results in a more uniform distribution of the daily precipitation for the western side of the mountain range Langfjella.

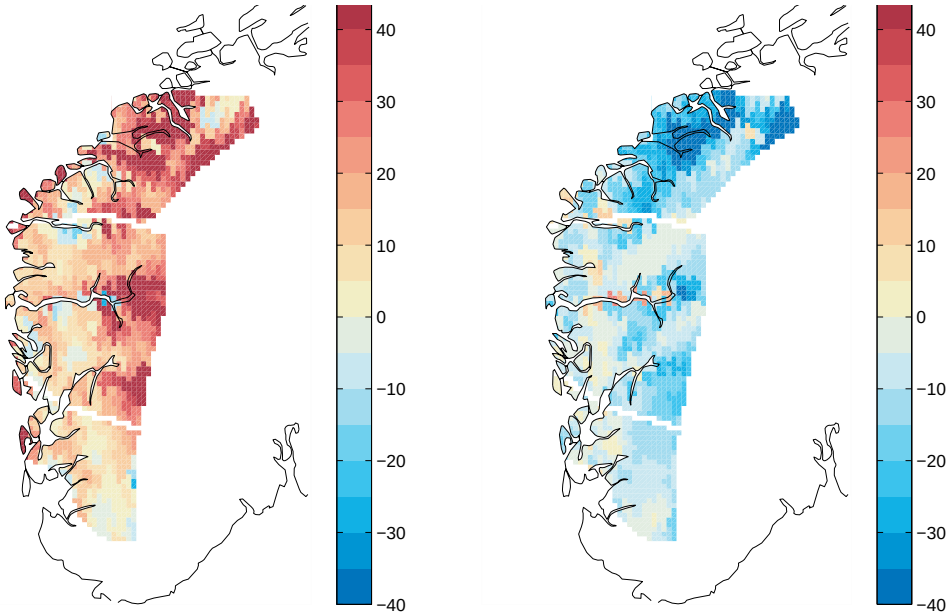

(a) Two degrees higher SST (b) Two degrees lower SST

Figure 6.11: Percentage change between the sensitivity simulations and the control run for the spring event (2. March 1997).

For all of the four cross sections the whole transect is experiencing an increase in the daily precipitation (Figure 6.12). For interested readers, all four cross sections can be found in Figure D.-8 in Appendix D. These transects verifies that central areas near the steepest slopes, which originally experienced the highest precipitation amount in the control run for the spring events, experienced the lowest relative increase in precipitation. The specific humidity has substantially increased with up to 20 % for all of the cross sections, and the vertical velocity has increased its value in most regions. There are some areas that have less ascending air than the control run, and these areas are either located before or in the area with the least percentage increase in the precipitation (Figure 6.12). The tendency of a shift in the less ascending air compared with the smallest increase in daily precipitation, might be due to the time needed in the production of large enough hydrometeors to escape the cloud to reach the ground without evaporating, as described in Section 2.2.

The average RH for the +2 simulation for the different areas were generally above 85% for the lowest 5 km. Sunnhordaland was the only cross section experiencing the +2 simulation to be lager than the control and -2 simulation for the lowest 500 metres (Figure 6.13a). The high values of RH for the different regions indicates that the air does not need to be cooled much adiabatically to reach saturation. When it came to the static stability, the values were more or less the same throughout the lowest 5 km, apart from the few

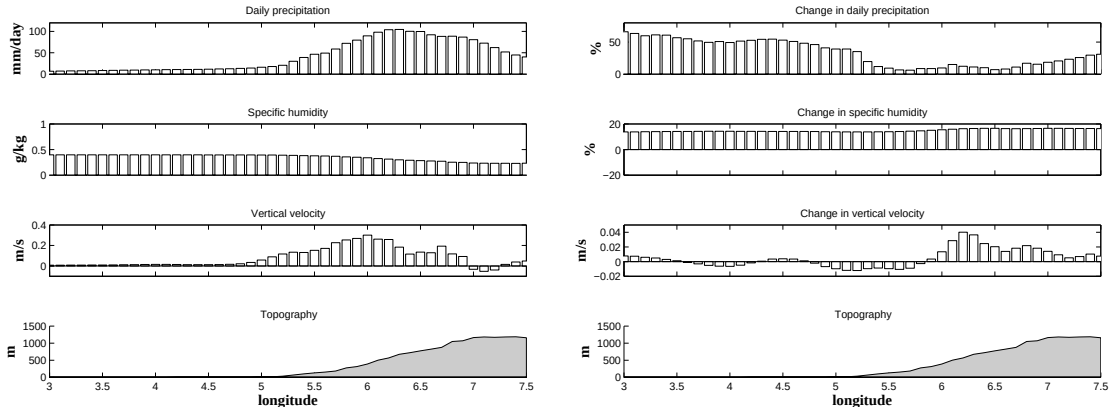

Figure 6.12: Cross section of the area Sunnhordaland for 2. March 1997. The control run, control_mar, is on the left side while the change between the simulation higher_mar and control_mar is on the right side. Each of the bars in the different boxes for the 4 parameters represent an average for that specific longitude in the transect box. For the daily precipitation and the specific humidity the percentage change is shown, while the vertical velocity is found by taking the difference between the two runs to avoid extreme percentage values.

hundred metres closest to the ground where the +2 simulation was generally more stable than the control run (Figure 6.13b). Due to the small change in static stability and large general values for RH, the increased amount of daily precipitation for the simulation with higher SST values does not come as a surprise.

The spring event had generally higher changes (%) in the daily precipitation and specific humidity, compared to the winter event. When comparing Table 6.5 with Table 6.3 from the +2 simulation for the winter event, the vertical velocity and RH seem to be more or less of the same magnitude. As a result, the higher changes in precipitation is due to the large increase in specific humidity for the spring event. Larger increase in specific humidity means a larger increase of humidity in the air for hydrometeor production.

Two degrees lower SST

For the -2 simulation the situation was reversed compared to the +2 simulation (Figure 6.11b). Most of the west coast had a decrease in the daily precipitation, with the largest percentage decrease in the coastal and inland areas. Around the fjords and the central areas of the west coast, there was either a small percentage decrease or increase in the daily precipitation. In other words, the areas that originally experienced the lowest amount of precipitation, experienced the relative largest changes in daily precipitation.

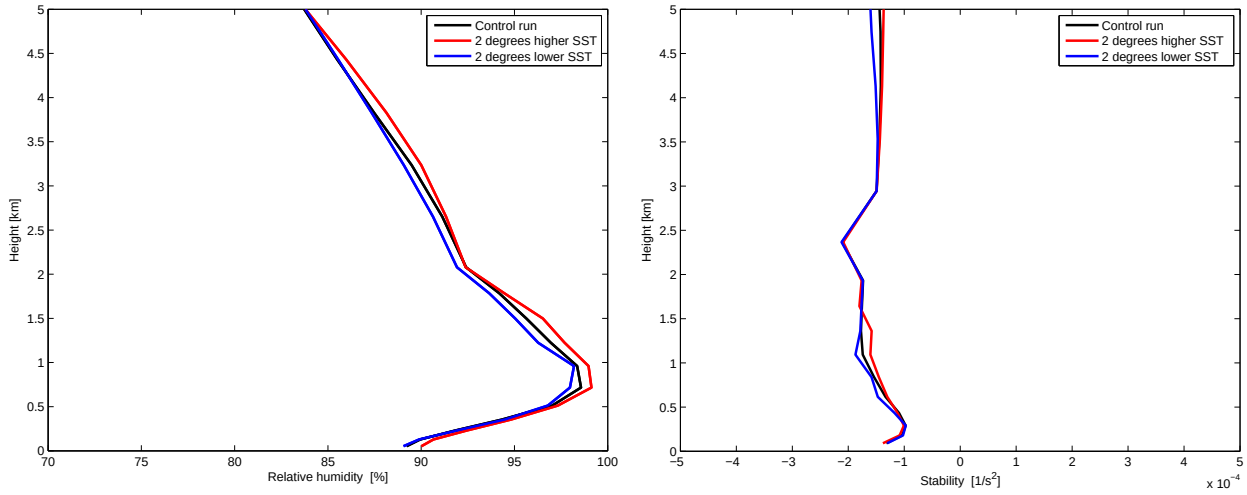

(a) Relative Humidity

(b) Static Stability

Figure 6.13: Vertical section of the average values of RH and Brunt Väisäla frequency (N^2) for the different vertical levels for the cross section Sunnhordaland for the spring event (2. March 1997). The black line represent the control run, the red line represent the +2 simulation and the blue line represent the -2 simulation.

Table 6.5: Percentage change between the sensitivity simulation with increased SSTs and the control run for the different parameters daily precipitation, specific humidity, vertical velocity and relative humidity for the spring event (2. March 1997). The values are found by taking the mean for the region the west coast (WC), and the 4 transect regions, Møre og Romsdal (MR), North of Sognefjorden (NS), South of Sognefjorden (SS) and Sunnhordaland (SH). Specific humidity is found by taking the vertical average where the vertical layers are not weighted equally. The vertical velocity and relative humidity is found by taking the vertical average over the lowest 3 km.

	Daily precipitation [%]	Specific humidity [%]	Vertical velocity [%]	Relative humidity [%]
WC	19.8	14.8	12.2	0.4
MR	28.9	14.6	50.2	0.2
NS	20.5	15.0	11.0	0.4
SS	16.5	15.3	13.7	0.8
SH	16.3	14.7	6.1	0.5

The four cross sections for the -2 simulation verify this result, where the daily precipitation decreased by a maximum of 20 % over most of the land areas. The specific humidity decreased between 10 and 20 % over all four transects. There was no general pattern for the vertical velocity. The cross section North of Sognefjorden experienced a strange result. A small increase in the precipitation was located in the same area as where the vertical velocity decreased the most, creating less ascending air (Figure 6.14). The reason for the observed increase in precipitation, might be due to colder air and therefore the relative humidity has increased. If this is the case, the air needs to be less adiabatically lifted to reach saturation and thereby producing clouds and precipitation, than it would for warmer air.

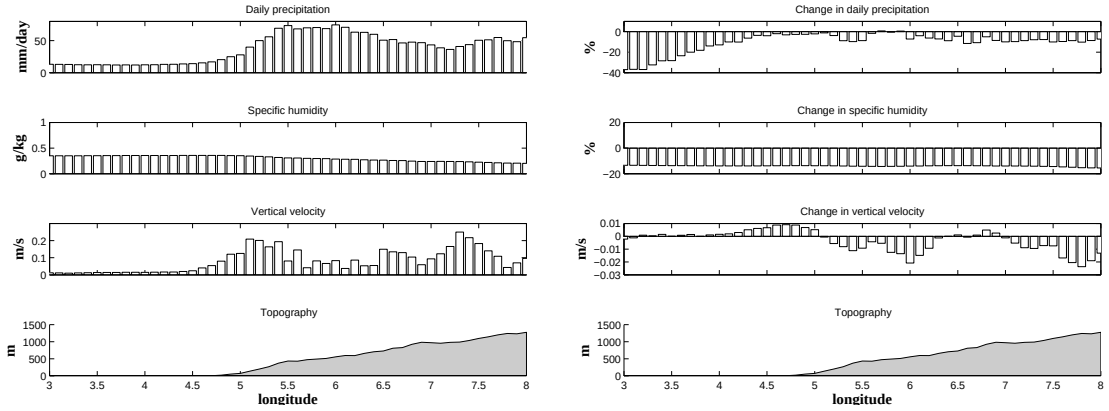

Figure 6.14: Cross section of the area North of the Sognefjorden for 2. March 1997. The control run, control_mar, is on the left side while the change between the simulation lower_mar and control_mar is on the right side. Each of the bars in the different boxes for the 4 parameters represent an average for that specific longitude in the transect box. For the daily precipitation and the specific humidity the percentage change is shown, while the vertical velocity is found by taking the difference between the two runs to avoid extreme percentage values.

As mentioned earlier, the average RH values for the -2 simulation was larger than for the +2 SST simulation for the lowest 500 metres for the areas besides Sunnhordaland. So the small increase in the daily precipitation seen in the area North of Sognefjorden could be a result of the increased RH in the lowest 500 metres (Figure 6.15a). The reason for this is that the air flow in the lowest layers reaching the coast would need less vertical lifting to reach saturation, thereby precipitation. The static stability was in general around -1×10^{-4} s^{-2}, and varied between being more and less unstable than the control run for the 5 lowest km (Figure 6.15b). It was therefore hard to conclude anything from the vertical sections of the static stability (Brunt Väisälä frequency).

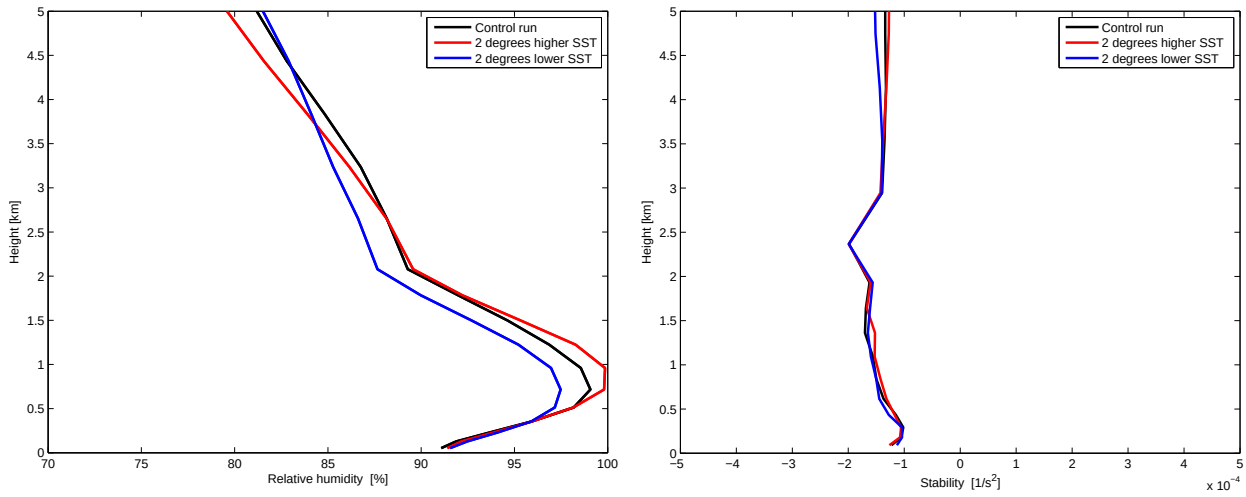

(a) Relative Humidity

(b) Static Stability

Figure 6.15: Vertical section of the average values of RH and Brunt Väisäla frequency (N^2) for the different vertical levels for the cross section North of Sognefjorden for the spring event (2. March 1997). The black line represent the control run, the red line represent the +2 simulation and the blue line represent the -2 simulation.

Table 6.6: Percentage change between the sensitivity simulation with decreased SSTs and the control run for the different parameters daily precipitation, specific humidity, vertical velocity and relative humidity for the spring event (2. March 1997). The values are found by taking the mean for the region the west coast (WC), and the 4 subjective transect regions, Møre og Romsdal (MR), North of Sognefjorden (NS), South of Sognefjorden (SS) and Sunnhordaland (SH). Specific humidity is found by taking the vertical average where the vertical layers are not weighted equally. The vertical velocity and relative humidity is found by taking the vertical average over the lowest 3 km.

	Daily precipitation [%]	Specific humidity [%]	Vertical velocity [%]	Relative humidity [%]
WC	-11.8	-13.4	-8.5	-0.8
MR	-24.1	-14.1	-59.8	-1.2
NS	-8.0	-14.0	-3.9	-1.0
SS	-9.4	-13.1	-4.9	-0.4
SH	-8.6	-12.6	-5.8	-0.3

The -2 simulation for the spring event (Table 6.5) seems to be less sensitive compared to the +2 simulation for the spring event (Table 6.6). The lower average change for the daily precipitation seems to be a result of a lower percentage change in vertical velocity and specific humidity for most of the areas.

6.3 The fall event: 15. November 2005

6.3.1 MERRA reanalysis

During the fall event, an extratropical cyclone is located in the Gulf of Bothnia (Figure 6.16). The resulting isobaric lines are perpendicular to the coast of Møre og Romsdal (Region 1). The large scale synoptic flow is therefore moving over the complex terrain on the west coast of Norway from a north-westerly direction. The mix of warm humid air from the south with cold polar air is not that obvious for the fall event as for the two other events. Still, the high pressure system located north of the Azores is probably pulling warm humid air from the south towards the north-westerly large scale flow, causing a mix of the two air masses.

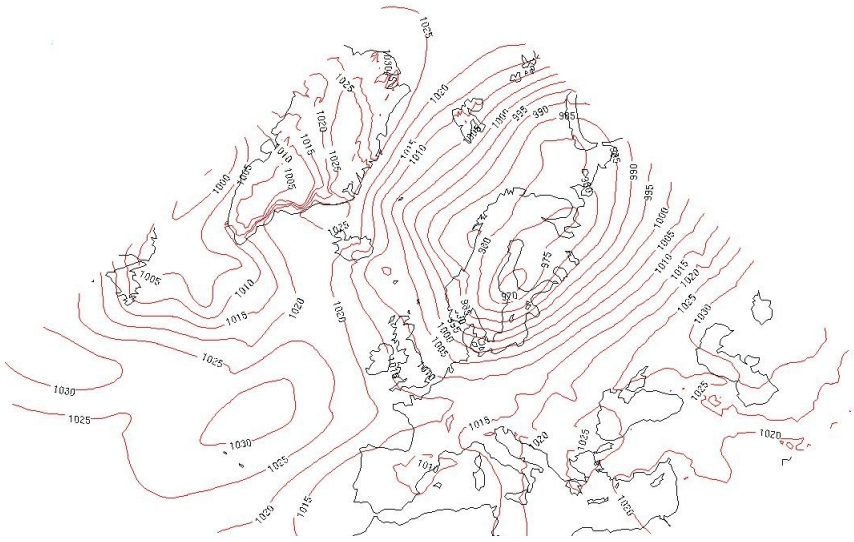

Figure 6.16: The large scale synoptic system by presenting the Sea Level Pressure (SLP) from the MERRA reanalysis at 06.00 UTC for the fall event (15. November 2005).

The distribution of the daily precipitation for the fall event, given by the MERRA reanalysis, indicate that the highest precipitation amounts are located in the mountainous inland areas in Region 2 and Region 3 (Figure 6.17a). Central areas in these two regions also seem to get high precipitation amounts, with values up to 90 mm/day. When comparing the results from the MERRA reanalysis with the observational data from a subjective point of view, it seems like the MERRA reanalysis data is not able to reproduce the highest precipitation amount, especially in the coastal regions. The reason for these underestimated values of daily precipitation is probably due to the coarse horizontal resolution in the MERRA reanalysis. As mentioned earlier, coarse horizontal resolution smooths out complex terrain and causes a possible poorly representation of the precipita-

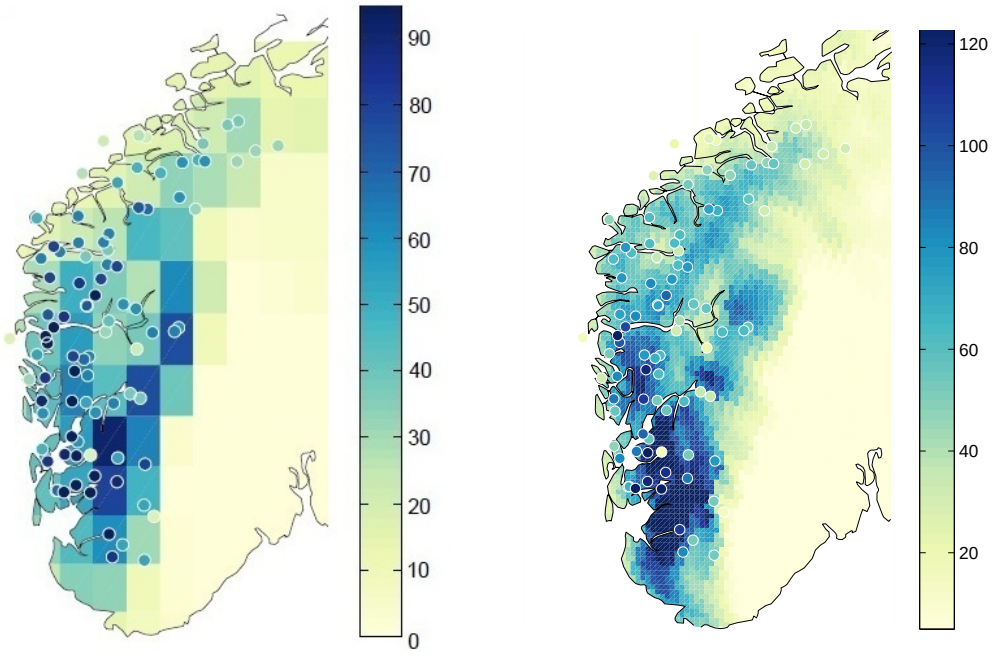

(a) MERRA reanalysis (b) WRF model

Figure 6.17: Daily precipitation distribution for the fall event (15. November 2005) created by a) the MERRA reanalysis and b) control run from the WRF model. Observational data are shown as circles. The colours represent the magnitude of precipitation.

tion due to small-scale convection. MAE of 28 mm/day and an overall underestimation of 29 % of the daily precipitation verify this (Table 6.7).

Table 6.7: Values of the MAE and MBE for the predictions compared with the observations for the 114 stations located in the chosen area for the fall event (15. November 2005). The table represent both model data from the MERRA reanalysis, and model data from the control runs created by the WRF model.

	MAE [mm/day]	MBE [%]
MERRA reanalysis	28.4	-29.2
WRF model	18.3	13.4

6.3.2 WRF model

The distribution of the daily precipitation produced by the WRF model for the fall event (Figure 6.17b) has the same pattern as the MERRA reanalysis, but with much higher precipitation amounts. The highest precipitation amounts (values up to 170 mm/day)

are located in Region 2 and Region 3, which also were the case for the MERRA reanalysis. By comparing the distribution from the WRF model with the observational data it seemed that the model actually produced higher precipitation amounts than what were observed for several of the stations. The statistical validation measure MBE confirm this (Table 6.7). The WRF model is actually overestimating the daily precipitation with 13 % compared with the MERRA reanalysis underestimation of 29 %. The MAE is 18 mm/day instead of 28 %. Hence, the WRF model is reproducing the fall event with higher accuracy compared to the MERRA reanalysis data.

From the four cross sections of the control run (Figure D.-13 in Appendix D), the daily precipitation is extremely dependent on the topographic slope. Large precipitation amounts are observed where the slopes of the terrain are steep. Areas that are flatter experienced less precipitation. This is due to less vertical velocity in these flatter areas, and therefore no adiabatic cooling to create condensation. The specific humidity decreases toward the mountain ridge Langfjella. The main reason for the decrease is that the air looses humidity as it precipitate. Sunnhordaland experienced the largest mean precipitation amount with values up to 120 mm/day.

As indicated by the two other events in Section 6.1.2 and Section 6.2.2, spectral nudging is causing the large scale synoptic flow to be orientated in the same direction for both the control and the two sensitivity simulations. Figure 6.18 shows the change in depth of the pressure systems, where increasing (decreasing) the SST values causes the low pressure center to be deeper (weaker). When comparing the large scale system from the MERRA reanalysis (Figure 6.16) with the result of the WRF model (Figure 6.18), it is about the same. Thus, the WRF model is able to reproduce the same results as the MERRA reanalysis for the three chosen events.

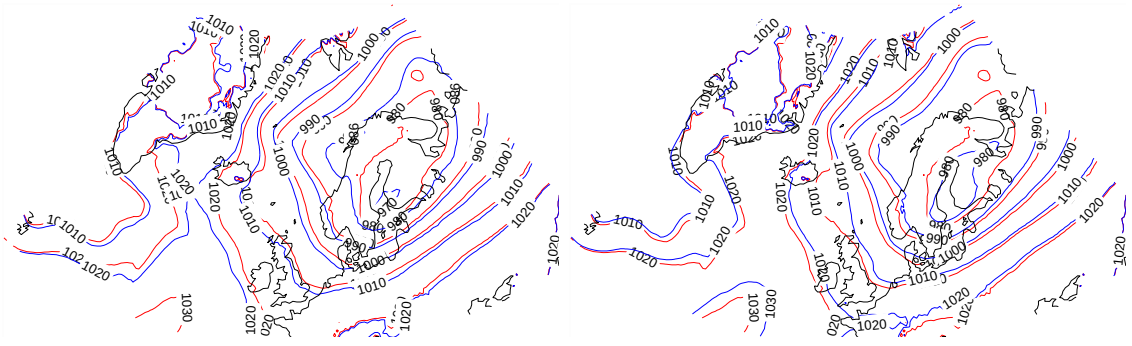

(a) Two degrees higher SST (b) Two degrees lower SST

Figure 6.18: Pressure fields for the control run (red line) and the sensitivity simulations (blue line) for the fall event (15. November 2005).

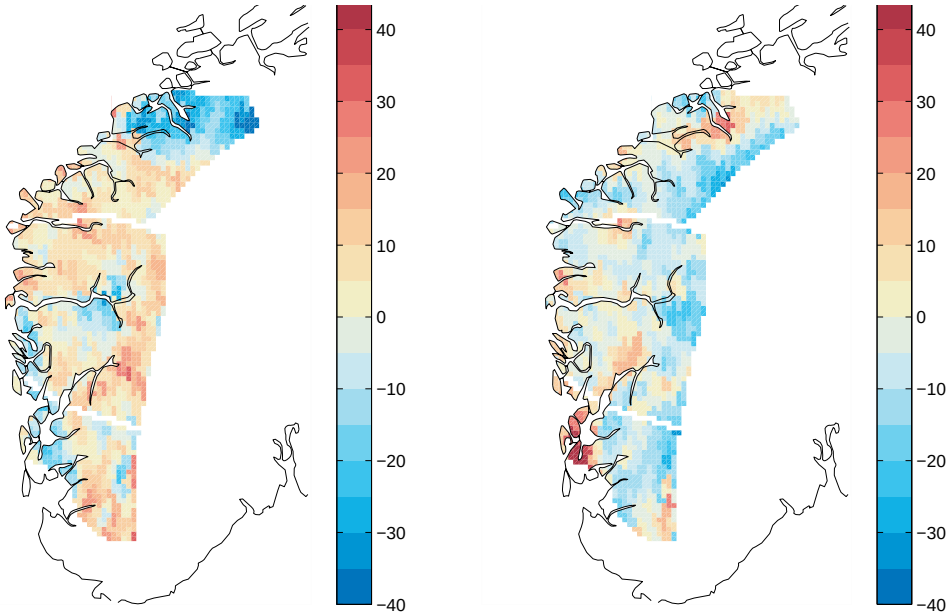

(a) Two degrees higher SST

(b) Two degrees lower SST

Figure 6.19: Percentage change between the sensitivity simulations and the control run for the fall event (15. November 2005).

Two degrees higher SST

For the west coast of Norway, a general increase in daily precipitation was the dominant effect when increasing the SSTs. The most notable change by increasing the SST was the decrease in precipitation in the northern part of Region 1, along Sognefjorden and in the coastal areas South of Sognefjorden (Figure 6.19a). It was hard to give a description of how the spatial distribution has generally changed, when comparing Figure 6.19a with the spatial distribution of the daily precipitation from the control run (Figure 6.17b).

From the four cross sections a general change in the spatial distribution for the daily precipitation was not found. The cross section Møre og Romsdal experienced a general decrease in the daily precipitation except in the coastal areas (Figure 6.20). This results from the strong decrease in daily precipitation seen in the northern part of Region 1 (Figure 6.19). The change in specific humidity was always positive in all of the cross sections with values around 10 %. This parameter was not able to explain the decrease, since the theory indicates that the daily precipitation should increase with increased specific humidity when relative humidity is close to saturation. The vertical velocity showed both stronger and weaker values in an oscillating pattern toward the inland area. It was therefore hard to conclude its effect on the precipitation. What probably happened, even though the air has been vertically lifted upwards, the increased SST values have increased

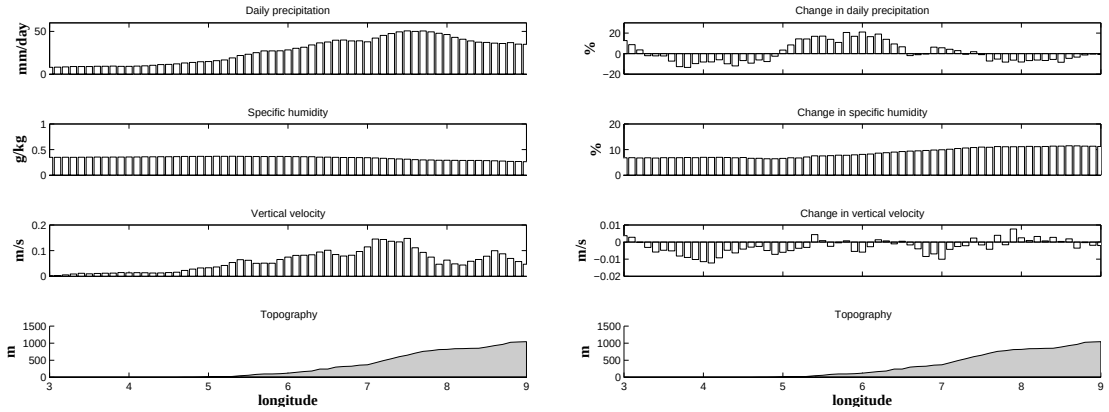

Figure 6.20: Cross section of the area Møre og Romsdal for 15. November 2005. The control run, control_nov, is on the left side while the change between the simulation higher_nov and control_nov is on the right side. Each of the bars in the different boxes for the 4 parameters represent an average for that specific longitude in the transect box. For the daily precipitation and the specific humidity the percentage change is shown, while the vertical velocity is found by taking the change between the two runs to avoid extreme percentage values.

the temperature so that the rising air does not become saturated even if the specific humidity has increased. The reason for this is that colder air demands less humidity to become saturated than warmer air. The decrease in precipitation in the coastal area was also noticeable in the cross section North of Sognefjorden and Sunnhordaland (see Figure D.-13 in Appendix D). From these transects it looks like the vertical velocity has a more pronounced effect, with lower positive values in both prior areas and in the area where the decrease in daily precipitation is seen.

The vertical cross section of the average RH for the area Møre og Romsdal showed that the simulation with higher SST was slightly lower compared to the control run for the lowest 5 km (Figure 6.21a). Even with increased amounts of humidity in the air it is not enough to compensate for the increase in temperature for these air masses in order to keep constant relative humidity. Therefore the air will need to be lifted higher to reach saturation causing the +2 simulation to have a lower value than what was seen for the control run. Throughout the lowest 5 km of the atmosphere, the +2 simulation experienced in general more stable air than the control run for all of the four areas (Figure 6.21b). The decrease in instability was at its highest around 2.5 km.

The +2 simulation for the fall event has the lowest percentage change in precipitation compared to the two other events. Under the assumption that the air is saturated, simple theory would predict a higher percentage increase in daily precipitation then seen from

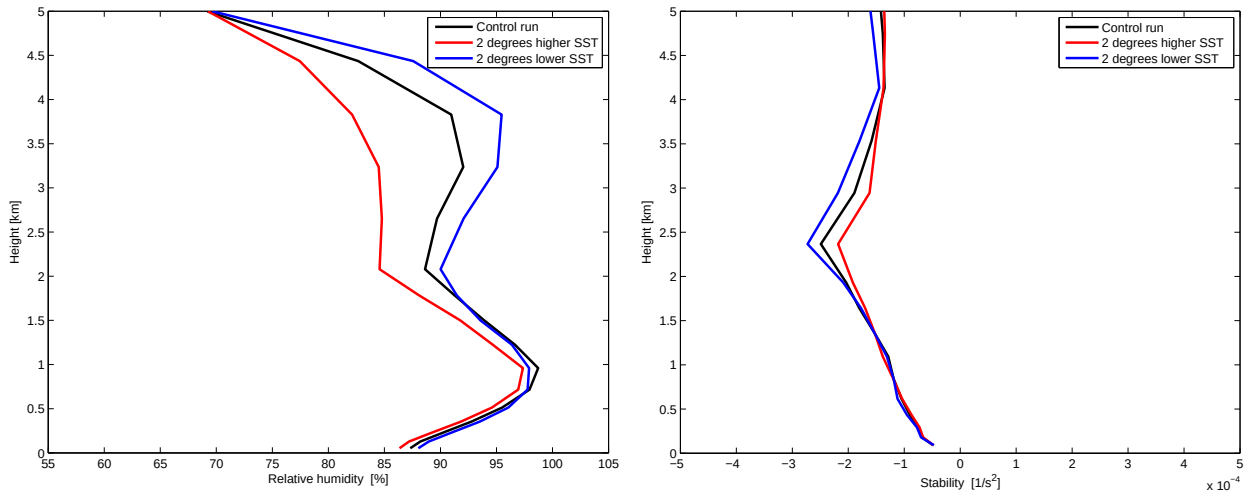

(a) Relative Humidity

(b) Static Stability

Figure 6.21: Vertical section of the average values of RH and Brunt Väisäla frequency (N^2) for the different vertical levels for the cross section Møre og Romsdal for the fall event (15. November 2005). The black line represent the control run, the red line represent the +2 simulation and the blue line represent the -2 simulation.

the +2 simulation for the fall event, when the vertical velocity and specific humidity had a percentage increase of up to 10 % (see Section 2.2 for more info). Hence, something else prohibits more precipitation to fall to the ground. Even with the percentage increase in both specific humidity and vertical velocity, the air may not reach its saturation level in the same height. The air may therefore be able to hold more of its water content on its way over the mountains. The percentage changes in RH support this statement (Table 6.8) where the daily precipitation is not increasing as much as the theoretical precipitation expect it to. The decrease in RH might result in smaller portions of the air column to be cooled adiabatically enough to reach saturation. The reason for decreased RH values for the +2 simulation can be seen from the Clausius Clapeyrons equation where the saturation vapor pressure is almost increasing exponentially with temperature. Hence, there is an exponential relationship between the amount of humidity in the air and the temperature of the air. So even with an increase in the specific humidity and vertical velocity, a smaller portion of the air column seems to be cooled enough adiabatically to reach saturation.

Two degrees lower SST

The change in the spatial pattern for the -2 simulation, was more or less the same as the +2 simulation just with the opposite sign (Figure 6.19b). The main difference between

Table 6.8: Percentage change between the sensitivity simulation with increased SSTs and the control run for the different parameters daily precipitation, specific humidity, vertical velocity and relative humidity for the fall event (15. November 2005). The values are found by taking the mean for the region the west coast (WC), and the 4 subjective transect regions, Møre pg Romsdal (MR), North of Sognefjorden (NS), South of Sognefjorden (SS) and Sunnhordaland (SH). Specific humidity is found by taking the vertical average where the vertical layers are not weighted equally. The vertical velocity and relative humidity is found by taking the vertical average over the lowest 3 km.

	Daily precipitation [%]	Specific humidity [%]	Vertical velocity [%]	Relative humidity [%]
WC	3.7	9.7	4.3	-1.4
MR	0.8	8.6	-5.0	-2.4
NS	8.3	10.2	6.2	-0.7
SS	2.3	9.7	5.6	-1.2
SH	3.8	10.4	10.1	-0.8

the changed SST simulations compared to the control run, is that the percentage change in the northern part of Region 1 which is not of the same magnitude as in comparison to lower SST.

These results were also seen in the cross sections with a general decrease in precipitation besides the coastal areas and in lee areas (Figure D.-13 in Appendix D). The specific humidity decreased with around 10 % and had the strongest decrease over the inland mountainous areas. In the areas where the precipitation has increased, the vertical velocity generally increased (Figure D.-13 in Appendix D). Another observation from this comparison was that the air was usually ascending faster towards the coast. This means that this air may have been cooled enough to reach its condensation level, so when the air hits the coast more precipitation has developed, and can thereby fall out.

The RH was generally a little higher for the -2 simulation compared with the control and +2 simulation in the the area between 1.5 km and almost up to 5 km (Figure 6.21a). In other words, the air is able to produce precipitation with lower adiabatic lifting in these areas, which means that the percentage decrease in precipitation will not be as large as the theory expect it to. The air is also generally more unstable for the 4 different regions (Figure 6.21b). This increased instability with the decreased SSTs is also supporting the lower decrease in daily precipitation values than the simple theory would suggest.

As indicated for the +2 simulation for the fall event, the daily precipitation is not decreasing as much as one would expect from simple theory on calculating the theoretical precipitation (Table 6.9). The increased values of RH is probably the main reason for

Table 6.9: Percentage change between the sensitivity simulation with decreased SSTs and the control run for the different parameters daily precipitation, specific humidity, vertical velocity and relative humidity for the fall event (15. November 2005). The values are found by taking the mean for the region the west coast (WC), and the 4 subjective transect regions, Møre pg Romsdal (MR), North of Sognefjorden (NS), South of Sognefjorden (SS) and Sunnhordaland (SH). Specific humidity is found by taking the vertical average where the vertical layers are not weighted equally. The vertical velocity and relative humidity is found by taking the vertical average over the lowest 3 km.

	Daily precipitation [%]	Specific humidity [%]	Vertical velocity [%]	Relative humidity [%]
WC	-4.5	-9.8	-7.9	0.4
MR	-7.0	-10.4	-7.3	0.8
NS	-4.7	-10.8	-3.4	-0.2
SS	-3.8	-9.9	-9.7	0.1
SH	-3.4	-8.5	-10.3	0.5

this. Even with the percentage decrease in both specific humidity and vertical velocity, portions of the air might reach its saturation level, due to the need of less adiabatic cooling from the increased RH values. When comparing Table 6.9 with Table 6.8 from the +2 sensitivity simulation for the fall event, it seems as if the the -2 simulation is more sensitive to the change in the SSTs. The reason for this might be due to the larger decrease in both the specific humidity and vertical velocity combined with a smaller average change in RH, which prohibit larger changes in the daily precipitation, for the -2 simulation compared with +2 simulation.

6.4 General similarities and differences

One of the the aims of this study was to see if the simple methods for calculating the theoretical precipitation could be used to represent the changes in intensity for the daily precipitation seen by the sensitivity simulations from the WRF model. For Alternative 1 (Clausius Clapeyrons equation), the specific humidity should change with about 6-8 %/K. If the air is saturated, the change in specific humidity is essentially what we might get as precipitation if all the other parameters remain unchanged (see Section 2.2 for more details). The equation indicates that a temperature change of one degree should cause a change of 6 to 8 percent of the precipitation depending on the pressure. Alternative 2 can be explained in a similar way, but here the specific humidity should change with about 2-6 %/K. To test the two methods, the average percentage changes in daily precipitation have been plotted against the average percentage changes in temperature 2 meters above

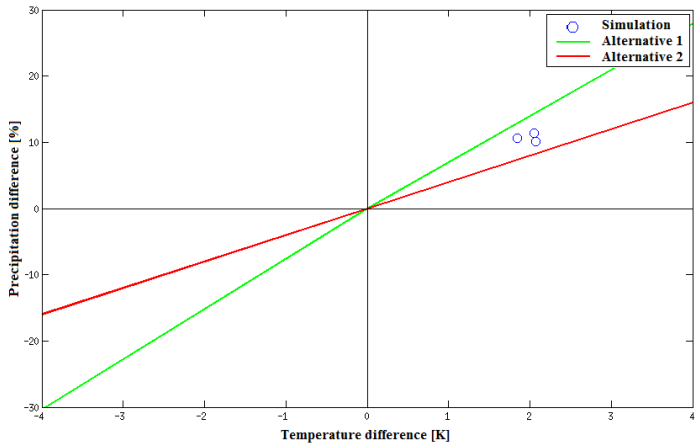

(a) The winter event

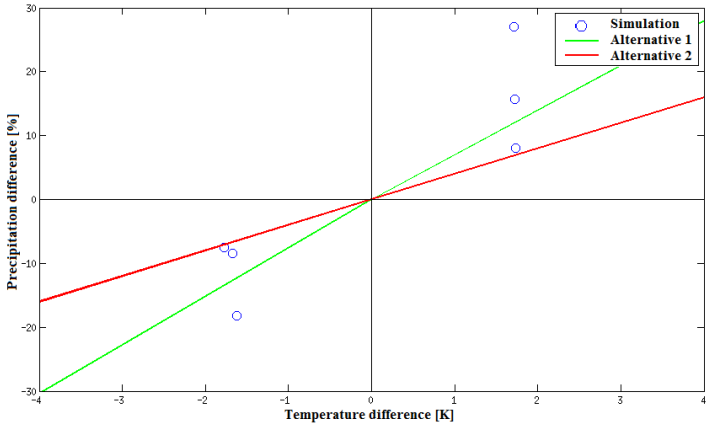

(b) The spring event

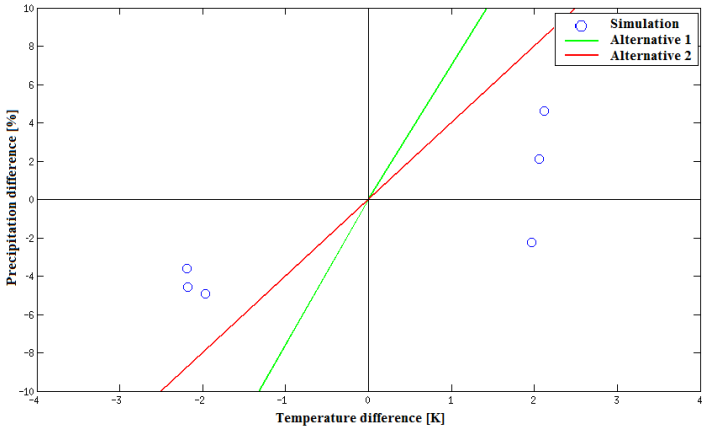

(c) The fall event

Figure 6.22: Comparing the percentage change in precipitation per Kelvin with Alternative 1 and Alternative 2 for the three chosen events. The percentage change in precipitation is indicated by the blue circles. These values are the percentage change between the average values of region 1, 2 and 3, see figure 5.1, for the 2 simulations with the average value of the same regions in the control run. Alternative 1 (green line) and Alternative 2 (red line) are the methods presented in Section 2.2 which can be used to calculate how the theoretical precipitation changes with temperature.

the ground for the 3 regions defined in Figure 5.1 for each of the three chosen events. Then to compare the result with Alternative 1 and Alternative 2 to see if the simple theory can explain the change in precipitation. From the average temperature 2 metres above the ground from the three events, Alternative 1 had a change of around 7 %/K while Alternative 2 had a change of around 4%/K.

The +2 simulation for the winter event experienced a percentage change in daily precipitation due to a change in temperature of 5.4 %/K (Figure 6.22a). From Figure 6.22a, the change of 5.4 %/K for the winter event is located between Alternative 1 (green line) and Alternative 2 (red line). The predicted change in daily precipitation is a bit closer to Alternative 2 than Alternative 1. Alternative 2 might therefore be able to reproduce the change in daily precipitation with higher accuracy, even if this method underestimate the simulated change in daily precipitation.

For the spring event on the other hand, there was a change of 8.3 %/K (Figure 6.22b). None of the two methods are able to explain the strong sensitivity of daily precipitation due to the change in SSTs. Even so, Alternative 1 is able to represent the spring event with higher accuracy than Alternative 2. This might be due to the larger role specific humidity plays for this event compared to the two other events.

Lastly, the fall event had a change of 1,4 %/K of the daily precipitation (Figure 6.22c), which is not even close to the theory given by the two methods. Alternative 2 (red line) represent this event better than Alternative 1 (green line), with a lower overestimation of the daily precipitation.

When the percentage change in daily precipitation is plotted against the change in SST, the average daily precipitation seems to change by 5 %/K (Figure 6.23a) for the four cross sections during the three events (Table 6.3, 6.5, 6.6, 6.8 and 6.9). From this figure a large spread in the values can be seen, where the strongest changes are for the spring event and the weakest changes for the fall event. Hence, when viewing all of the sensitivity simulations from the three events are the method Alternative 2 representing the average change in precipitation per Kelvin. The specific humidity on the other hand, is more or less affected in the same way with the change in SST for all of the regions for the 3 events. Increasing (decreasing) the SST will cause an increase (decrease) in the specific humidity. By comparing the percentage values for all of the regions and events the specific humidity will in average increase with 5.7 %/K (Figure 6.23b). This value is closer to the estimate from Alternative 1 than Alternative 2. Hence, the specific humidity acts in a similar way as expected by the Clausius Clapeyrons equation (Alternative 1) for calculating the theoretical precipitation.

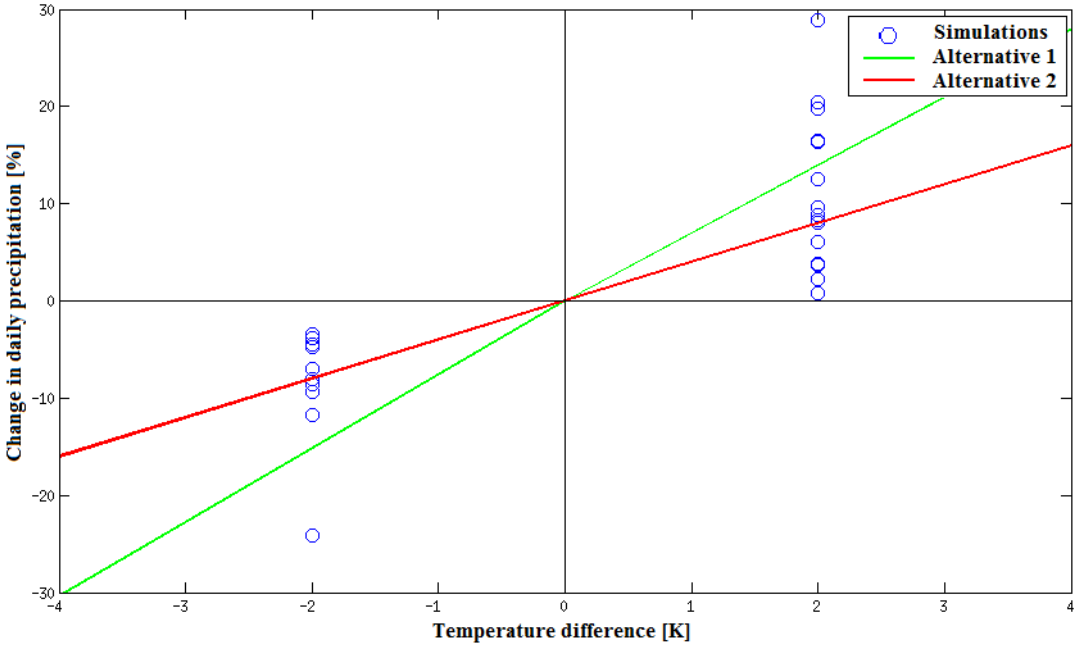

(a) Daily precipitation

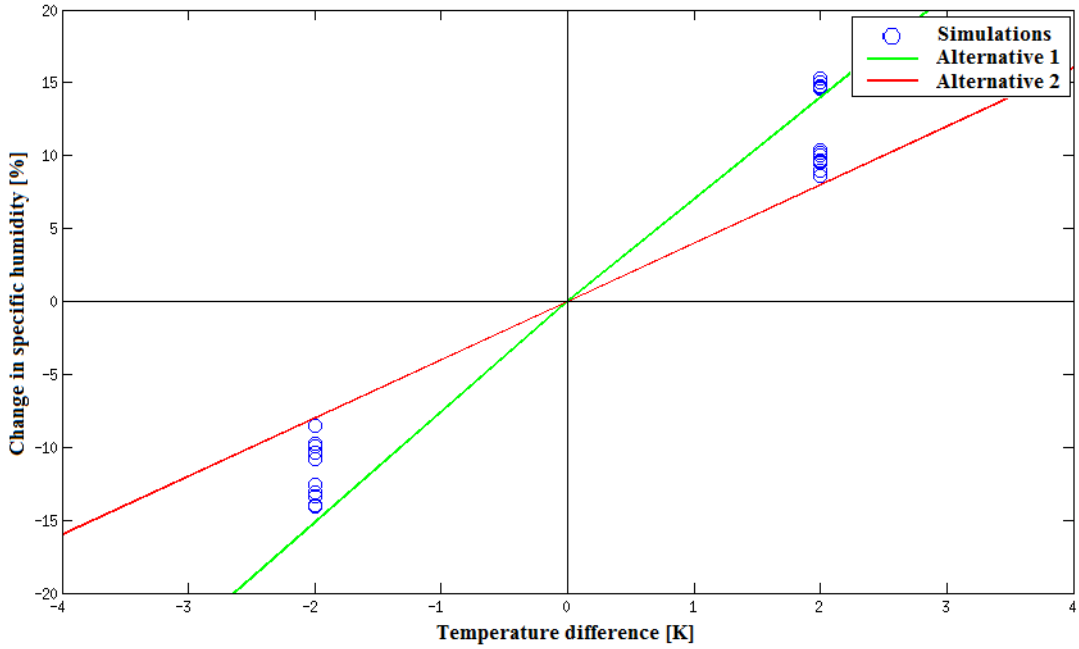

(b) Specific humidity

Figure 6.23: The percentage change in a) daily precipitation and b) specific humidity, for all of the simulations for the 3 events, is indicated by the blue circles. Alternative 1 (green line) and Alternative 2 (red line) are the methods presented in Section 2.2 which can be used to calculate how the theoretical precipitation changes with temperature.

By all of this it seems like Alternative 2 would be a better approximation for both the winter and fall event. But even this method produces values that are either too large or too small compared with the predicted values produced by the WRF model. Alternative 1 seems to work quite well for the spring event even if the values might be underestimated compared with the WRF model. Alternative 1 and Alternative 2 might be able to give indications on the changes in daily extreme precipitation amounts, but its assumptions on no change in vertical velocities, temperature profiles(only for Alternative 1) or depth of the saturated layer makes it very crude. Therefore, it might be best to use a method which uses thresholds for precipitation, such as relative humidity, to be able to calculate the precipitation changes with larger accuracy. Effects such as the time and space delay of air reaching saturation and precipitation reaching the ground, might also increase the accuracy. This is especially important when it comes to the spatial distribution.

Another interesting result was how the mean vertical velocity varied in the vertical for the different cross sections for the four areas. The mean vertical velocity oscillates from ascending to descending with higher altitudes almost like a sinus/cosine function (Figure 6.24). This result demonstrates that the simple internal wave theory gives some indications on flow over complex topography. It is important however to remember that these vertical sections of the mean vertical velocity for each layer does not represent every air flow over the different topography. Instead it gives an understanding that the large scale topography (Langfjella) has the largest effect on the flow over the topography in southern Norway.

6.5 Conclusions

In the study of the three individual cases, the ability of the MERRA reanalysis and the WRF model reproduction of the events were tested by the statistical errors MAE and MBE. In general, the events were underestimated by the two methods, except for the fall event which was overestimated by the WRF model. The systematic error (MBE) was greatly improved by almost 20 % for the three events by the use of the WRF model instead of the MERRA reanalysis. The WRF model was in general reproducing the individual observations with a 10 mm/day lower MAE compared to the MERRA reanalysis. The improved presentation of the events by the WRF model is due to higher horizontal resolution. The higher resolution causes the model to represent the topography better causing enhanced orographic precipitation, and to be able to represent precipitation values due to small scale convection and friction.

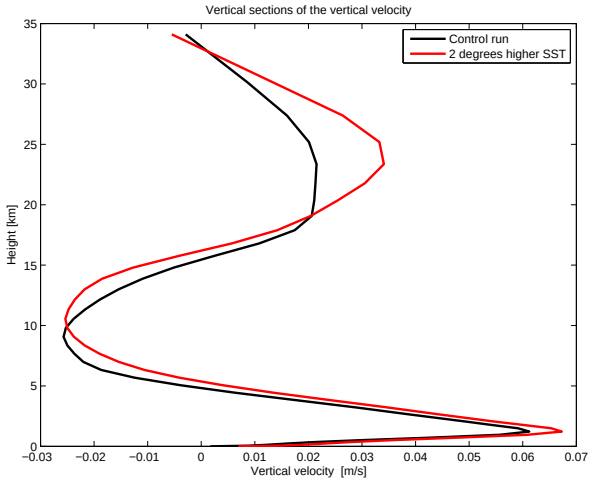

(a) 11. January 1992

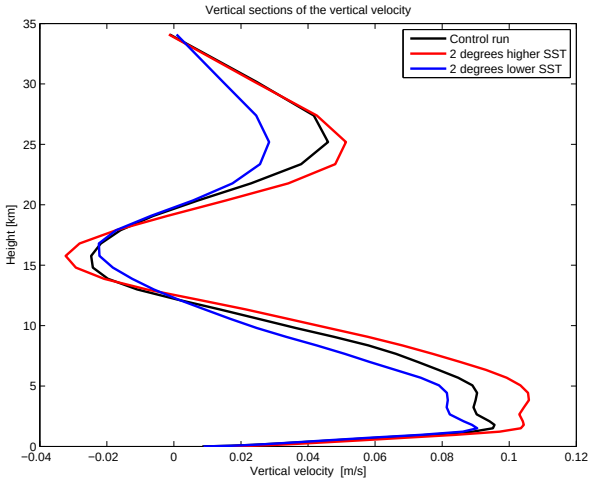

(b) 2. March 1997

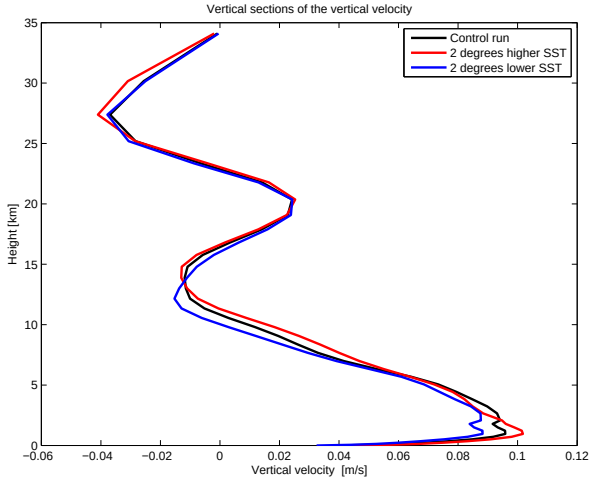

(c) 14. November 2005

Figure 6.24: Vertical sections of the mean vertical velocity (m/s). The vertical velocity is calculated as the average velocity for each vertical layer in the cross section South of Sognefjorden.

The study showed, that with changed SST values for the entire domain, the WRF model with the use of spectral nudging was able to sustain the large scale synoptic system as in the control runs. The intensity of the low pressure system did not seem to be much affected by the changed SST. This supports Bengtsson et al. (2009) finding that extratropical cyclones does not change in intensity with increased temperatures but with an increase in the temperature gradient.

The study of the three individual cases showed that they all responded differently to the changed SST values for the entire domain. The winter event experienced a general decrease (increase) in the coastal areas and increase (decrease) in the mountainous inland areas for increased (decreased) values of SST. In other words, there is a shift in the distribution of the daily precipitation. By comparing the different parameters (specific humidity, vertical velocity, relative humidity and static stability) with the distribution of daily precipitation, it is reasonable to conclude that the shift with decreased amounts of precipitation in the coastal areas and an increase in the mountainous areas further inland is a result of the vertical velocity. The vertical velocity prior to hitting the coastal areas indicates that air is not adiabatically cooled to the same degree as for the control run due to vertical lifting. The opposite occurs after the air passes the coastal areas. The study of the spring event showed that the WRF model predicts the largest percentage change in specific humidity, upto 20 %. All of the simulations also showed a RH over 85 % for the lowest 5 km. When knowing this, it is no surprise that the spring event had the largest percentage change in the daily precipitation of the three event. A change in the distribution was not that obvious for the spring event. The fall event on the other hand, had the lowest overall change in daily precipitation. From the different analysis of the parameters mentioned above it seems as if a combination of the RH and static stability are the main contributors. With increasing (decreasing) SST values the air became less (more) unstable and the RH decreased (increased) resulting in a lower response in the daily precipitation. Even with a relatively small response with the changed SST values compared to the other events, the fall event experienced a change in the daily precipitation distribution in coastal areas south of Sognefjorden and the northern part of Møre og Romsdal. The vertical velocity seems to have a similar effect as for the winter event.

The static stability and RH might be the biggest contributor for why the fall event is not able to reproduce percentages of the same size as the spring event in changed daily precipitation due to a change in SST. From the study of the static stability, the general result indicates that the air in the lowest 5 km for all of the events was unstable. An increase in SST caused the air to be less unstable compared to the control run, the oppo-

site when decreased SST. As indicated by the Clausius Clapeyrons equation, there is an exponential relationship between the amount of humidity in the air and the temperature of the air. As a result, the fall event experience a general decrease (increase) in RH with increased (decreased) SST. The spring event on the other hand, had the highest percentage change in specific humidity and therefore experienced a general increase (decrease) in RH for increased (decreased) SST. The lower sensitivity in daily precipitation for the winter event compared to the spring event seems to be due to the lower percentage change in specific humidity for the winter event. A larger change in specific humidity result in a large change in the air storage of humidity which can be used for hydrometeor growth.

The general conclusion from the study is that simple theory on calculating theoretical precipitation can be used for some events. When the percentage changes in daily precipitation for the three individual events is combined, Alternative 2 seems to represent them best. The main reason for this is probably that the method includes how the temperature changes with height. Latent heat release is an effect of condensation of water vapor in humid air, and as a results the temperature gradient will change. However, each event is unique. So none of the two simple presentations of the theoretical precipitation can be used for all three cases. Of the two, Alternative 1 would work best for the spring event. Alternative 2 would probably represent both the winter and fall events best. With the need of more accurate quantitative predictions of precipitation, a reinforcement of these simple methods would probably result in more accurate values. Thresholds for precipitation with parameters such as RH and by including the time and space delay of hydrometeor production as presented in the paper Sinclair (1994) could result in higher accuracy for precipitation amounts.

The vertical section of the vertical lifting of the air over the complex terrain on the west coast of Norway seems to be mainly driven by the large scale topography, Langfjella, when taking the average values for the chosen area. Thus, quite simple theory gives reasonable representation of the large scale vertical velocity. To get a better description of the vertical velocity on a much smaller scale in a complex terrain, a more complex model/method is needed.

Chapter 7

Summary

The investigation of the time distribution for the 50 most extreme daily precipitation events indicated, even with a large yearly change in number of events, a trend with increased number of events over ten year periods between 1970-1999. The largest number of these 50 events occurred during late fall and winter months. From investigation of the synoptic situation during the 50 most extreme daily precipitation events, the large scale flow on the west coast of Norway contained no easterly component. The extratropical cyclones where positioned so that a mixed air mass of warm humid air from the south and cold polar air was pushed toward the west coast of Norway.

In the study of the three case studies, the statistical errors MAE and MBE showed that the ability to recapture the daily precipitation amount improved with the use of the WRF model compared with the use of the MERRA reanalysis data. The systematic error was greatly improved by almost 20 % and the individual error was reduced for the given events with up to 10 mm/day. The WRF model simulations were done with higher horizontal resolution than the MERRA reanalysis data causing topography and small scale features to be better represented.

The detailed study of the three case studies, indicated a different response in both distribution and intensity with an equal change in the SST values for the entire domain. A general shift in the distribution of the daily precipitation was seen for the winter and fall event. Increasing (decreasing) the SST values caused a decrease (increase) in daily precipitation for coastal regions, and an increase (decrease) in the inland mountainous areas. The combination of the response in RH and the vertical velocity seems to be able to explain the shift in the daily precipitation distribution, especially for the fall event. The change in the intensity of the daily precipitation, with over 20 % for some areas, was most pronounced for the spring event. Specific humidity had its largest percentage

change for this event and is therefore probably one of the biggest reasons for the large intensity change. The different responses in the change in intensity of the daily precipitation is probably due to the combination of RH and static stability. Instability seem to generally increase (decrease) with decreased (increased) SST values, creating a more "hostile" situation for adiabatic cooling due to vertical lifting. This effect is reinforced in the fall event with the generally increase (decrease) with decreased (increased) SST values. In other words, the detailed study of the three case studies did not produce a general response in distribution and intensity for changing the SST values.

A study of the percentage change per Kelvin in daily precipitation indicated that each event is an unique event. Thus, none of the two simple methods to calculate the theoretical precipitation are able to explain all the events with high accuracy. Alternative 1 worked best for the spring event, while the two other events were better represented by Alternative 2. To be able to represent the response for the different events with more accuracy the simple methods might be better by introducing threshold for parameters such as RH, and the time delay for hydrometeor production and the fall speed of precipitation.

Chapter 8

Future work

To give more information on how extreme precipitation events studied in this thesis have changed through time, an observational study over a longer time period would be ideal. Where the events have a certain percentage of the stations observing extreme precipitation for the chosen area. By creating monthly, yearly and ten year distributions trends might be seen more clearly. Possible trends might give more indication about what to expect in future climate.

Case studies on other extreme daily precipitation events for the same area may result in more general conclusions for the different types of extreme daily precipitation events. Events with similar large scale situations may respond in a similar way by changing the SST. The season for the event can also have an affect. More general conclusions on certain conditions may produce a better understanding about why a certain event becomes extreme for the daily precipitation. A better understanding could result in better presentation of different processes so that numerical models can predict these extreme events with higher accuracy. Other parameters (wind, temperature gradient in the sea surface layer, latent heat fluxes etc.) that have a large influence on the orographic enhanced precipitation could also be tested. It is important to create better understanding about these types of events due to their severity. Insight into how these extreme daily precipitation events might change in future climate, could result in saving lives and reducing costs of rebuilding destroyed infrastructures.

By running the different simulations with higher resolution in the WRF model (maybe down to a horizontal grid size of 1 km), effects on a much smaller scale could be further investigated. Nested grids could also be used to increase the models ability to capture small scale features, where the cost in both computing time and storage space would be less than increasing the resolution for the entire domain. To explain local effects during

a large scale extreme precipitation event is an important aspect for prediction of floods, landslides and avalanches.

Appendix A

Stations

Table A.1: Containing the names, id number, latitude, longitude and meters above sea level for the 114 stations chosen in this thesis, which lies in either Region 1, Region 2 or Region 3 and has 80 % data of daily precipitation in the timeline 1961-2009.

Name	ID number	Latitude [^{o}]	Longitude [^{o}]	Meter above sea level [m]
Eide pånordmøre	62900	62.8915	7.3905	49
Hustadvatn	62700	62.9088	7.2453	80
Vigra	60990	62.5617	6.1150	22
Svinøy fyr	59800	62.3283	5.2700	38
Eresfjord	61820	62.6635	8.1063	14
Eikesdal	61850	62.4740	8.1765	39
Norddal	60400	62.2477	7.2415	28
Tafjord	60500	62.2335	7.4167	15
Ångårdsvatnet	63580	62.6717	9.1978	596
Nerskogen II	66580	62.7672	9.5687	803
Hjelvik i romsdal	61170	62.6162	7.2107	21
Åndalsnes	61350	62.5658	7.6773	20
Verma	61550	62.3418	8.0517	247
Berkåk - Lyngholt	66730	62.8173	10.0172	475
Rindal	64900	63.0380	9.2205	228
Ona II	62480	62.8597	6.5395	13
Geiranger	60300	62.0765	7.2415	419
Øksendal	63100	62.6855	8.4245	47
Sunndalsøra III	63420	62.6750	8.5588	6
Ålvundfjord	64580	62.8347	8.5213	5
Innerdal	64700	62.7222	8.7912	403
Surnadal	64800	63.0050	9.0113	39
Halsafjord II	64460	62.9762	8.2427	12
Ekset i Volda	59670	62.1678	6.0347	58
Ålesund III	60970	62.4762	6.2015	136

Ørskog	60800	62.4788	6.8200	4
Hornindal	58960	62.0032	6.6512	340
Stadlandet	59450	62.1477	5.2140	75
Lesjaskog	61770	62.2317	8.3733	621
Osland ved Stongfjorden	57110	61.4327	5.2217	119
Aurland	53700	60.9032	7.2018	15
Svelgen II	57810	61.7708	5.2988	3
Davik II	57860	61.8833	5.5500	3
Ålfoten II	57940	61.8320	5.6687	24
Nordfjordeid - Nymark	58780	61.9190	6.0403	34
Hovlandsdal	56520	61.2345	5.4323	60
Dale i Sunnfjord II	56650	61.3533	5.4022	51
Eikefjord	57680	61.5888	5.4720	30
Haukedal	56960	61.4202	6.3758	329
Botnen i Førde	57480	61.5362	6.0602	237
Oppedal i Gaular	56860	61.3180	6.2180	241
Viksdalen i Gaular	56850	61.3262	6.1983	243
Sandane	58070	61.7878	6.1857	51
Myklebust i Breim	58320	61.7135	6.6165	315
Takle	52860	61.0267	5.3850	38
Brekke i Sogn	52930	60.9593	5.4268	240
Rørvikvatn ved Vadheim	56280	61.2163	5.7513	350
Lavik	56320	61.1122	5.5470	31
Skei i Jølster	57390	61.5760	6.4922	205
Fortun	55160	61.5000	7.7005	27
Hafslo	55550	61.2925	7.1887	246
Lærdal - Tønjum	54130	61.0617	7.5167	36
Borlo	54500	61.0742	7.9553	502
Maristova	54600	61.1093	8.0360	806
Sogndal - Selseng	55730	61.3348	6.9335	421
Fjærland - Skarestad	55840	61.4383	6.7683	10
Ytre Solund	56400	61.0047	4.6758	3
Innvik	58400	61.8503	6.6267	32
Briksdal	58480	61.6945	6.8097	40
Sindre	58880	61.9238	6.5418	118
Vik i Sogn III	53070	61.0728	6.5813	65
Vangsnes	53100	61.1725	6.6455	51
Øvre Årdal	54780	61.3115	7.8183	28
Holsnøy - Landsvik	52440	60.6055	5.0590	27
Bergen - Fredriksberg	50560	60.3963	5.3095	41
Eidsfjord	49630	60.4668	7.0723	5
Liset	49750	60.4232	7.2732	748
Kvåle	49070	60.2803	6.3828	342
Nedre Ålvik	50050	60.4323	6.419	18
Øystese - Borge	50080	60.3790	6.1927	108

Omastrand	50130	60.2170	5.9837	2
Eikanger - Myr	52400	60.6230	5.3808	72
Haukeland	52600	60.8248	5.5732	196
Frøyset	52750	60.8480	5.2173	13
Modalen	52300	60.8333	5.9333	104
Tyssedal I	49350	60.1198	6.5608	32
Tysse	50250	60.3690	5.7473	41
Kvamskogen	50300	60.3933	5.9133	408
Samnanger	50350	60.4640	5.8938	370
Kinsarvik	49550	60.3725	6.7382	108
Fjellanger II	52110	60.7992	6.0660	456
Eksingedal	52170	60.8027	6.1502	450
Gullbrå	52220	60.8288	6.2500	579
Øvstedal	51250	60.6887	5.9647	316
Brekkhus	51400	60.7365	6.1438	202
Bulken	51470	60.6460	6.2235	323
Voss - Bø	51590	60.6450	6.4950	125
Fana - Stend	50450	60.2733	5.3315	54
Slåtterøy fyr	48330	59.9083	5.0683	25
Etne	47500	59.6648	5.9655	35
Eikemo	47820	59.8580	6.2825	178
Fitjar - Prestbø	48250	59.9167	5.3163	24
Indre Matre	47900	59.8500	6.0000	24
Husnes	48450	59.8643	5.7698	13
Rosendal	48500	59.9910	6.0240	51
Hatlestrand	50150	60.0422	5.9057	45
Røldal	46450	59.8293	6.8253	393
Litlabø- Dale	48090	59.7927	5.4318	35
Lysebotn	45350	59.0568	6.6493	9
Sauda	46610	59.6487	6.3633	5
Skreådalen	42890	58.8215	6.716	474
Øvre Sirdal	42950	58.9463	6.9193	582
Ulla	46050	59.3805	6.5248	200
Sand i Ryfylke II	46150	59.4787	6.2783	25
Suldalsvatn	46300	59.5887	6.8090	333
Hundseid i Vikedal	46850	59.5558	5.9955	159
Nedre Vats	46910	59.4840	5.7507	64
Skjold - Viken	47120	59.5000	5.6000	11
Skjold - Frøvik	47090	59.5033	5.6257	5
Ljosland - Monen	41550	58.7880	7.3522	504
Bykle - Kultran	40420	59.3517	7.3468	599
Bjåen	40900	59.6415	7.4433	927
Homme	40270	59.2382	7.5467	364
Vågsli i Vinje	33900	59.7667	7.3667	821

Appendix B

Average daily precipitation over two days

Table B.1: The 50 most extreme precipitation events from 1960 to 2009 for the the merged dataset, were the daily precipitation is taken as the average over two days. They are organized after percentage of stations that experienced extreme precipitation for that given date.

Number of Stations	Percentage of Stations [%]	Date	Max precipitation [mm/day]
74	81	14 Nov 2005	223.0
67	60	31 Mar 1997	158.2
64	57	11 Jan 1992	156.2
61	54	16 Mar 1990	138.0
60	53	4 Feb 1993	138.7
59	53	18 Oct 1995	121.2
51	47	1 Mar 1997	175.0
51	45	9 Mar 1983	172.8
49	43	28 Jan 1989	142.5
47	42	10 Dec 1973	124.1
47	41	4 Mar 1990	109.4
47	41	10 Nov 1986	129.2
46	41	28 Nov 1999	135.8
46	40	17 Sep 1978	178.5
32	40	11 Jan 2009	121.6
45	39	4 Dec 1986	102.2
34	38	13 Sep 2005	160.0
41	37	26 Oct 1995	184.6
40	37	17 Dec 1966	162.2
41	36	26 Dec 1975	151.2
39	36	15 Mar 1967	149.9
40	35	30 Aug 1984	123.0
32	35	11 Dec 2006	89.8
36	34	15 Oct 1967	90.6

37	33	21 Nov 1980	129.7
37	32	19 Dec 1993	123.5
36	32	23 Sep 1975	170.3
30	31	6 Jan 2005	146.0
28	31	5 Nov 2006	146.2
30	30	15 Nov 2004	195.0
30	28	5 Feb 1967	169.6
30	27	20 Mar 1993	144.3
28	25	6 Nov 1992	89.2
28	25	25 Oct 1983	138.1
24	25	5 Dec 2004	161.0
27	24	3 Jan 1992	131.0
27	24	14 Jan 1989	110.7
27	24	1 Jan 1984	156.2
27	24	27 Oct 1983	131.6
27	24	7 Oct 1975	109.3
22	24	31 Oct 2007	135.6
26	23	9 Sep 1997	75.0
26	23	9 Oct 1992	175.0
26	23	3 Nov 1971	124.0
25	22	28 Nov 1986	105.0
25	22	20 Jan 1983	140.2
25	22	19 Oct 1970	106.5
24	21	14 Dec 1992	127.5
23	21	1 Feb 1981	119.0
23	20	28 Nov 1984	117.3

Appendix C

Figures of the Surface Level Pressure

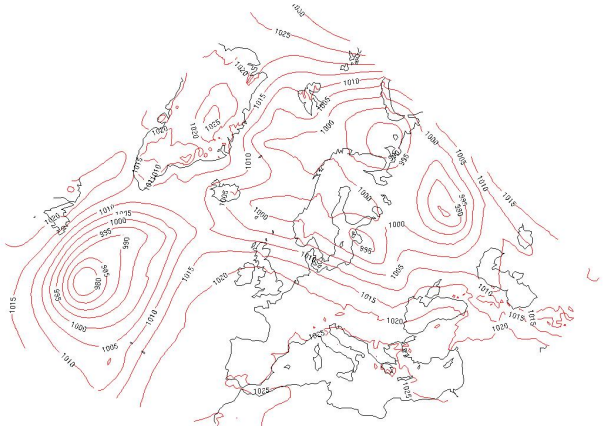

(a) 9. March 1983

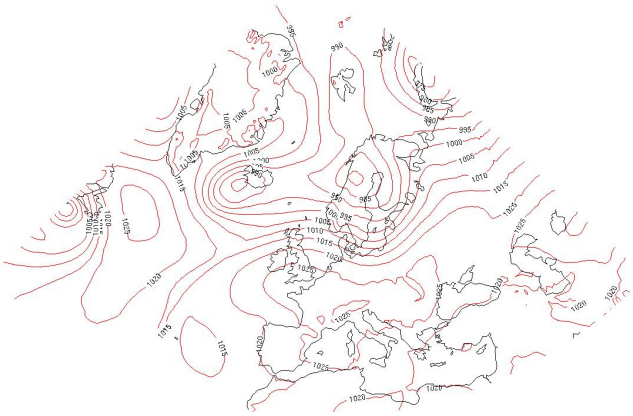

(b) 26. October 1983

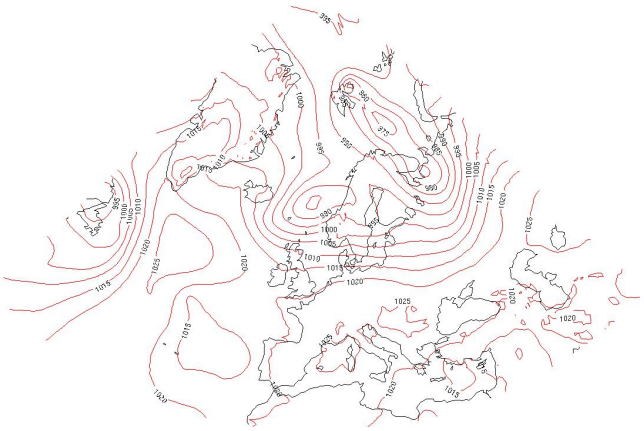

(c) 27. October 1983

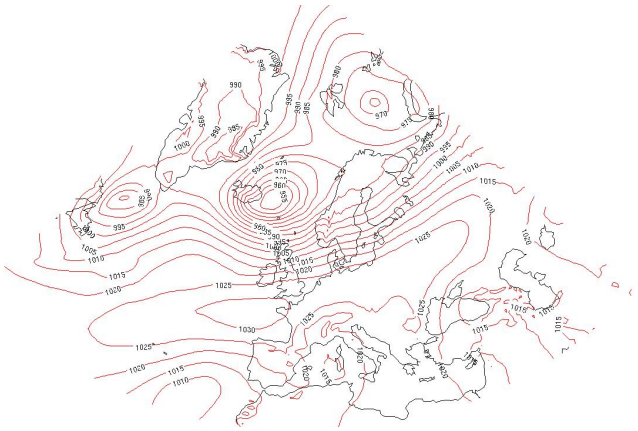

(d) 30. October 1983

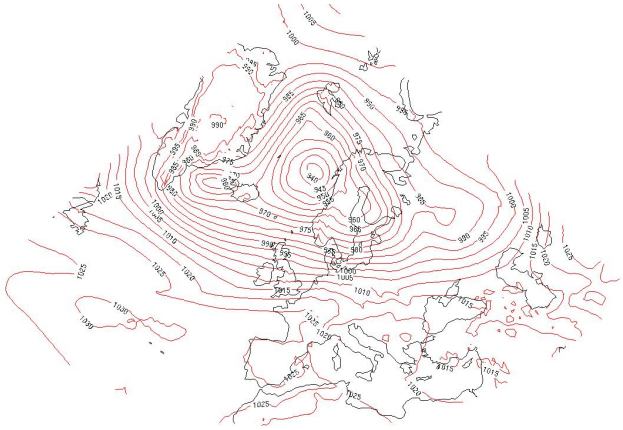

(e) 1. January 1984

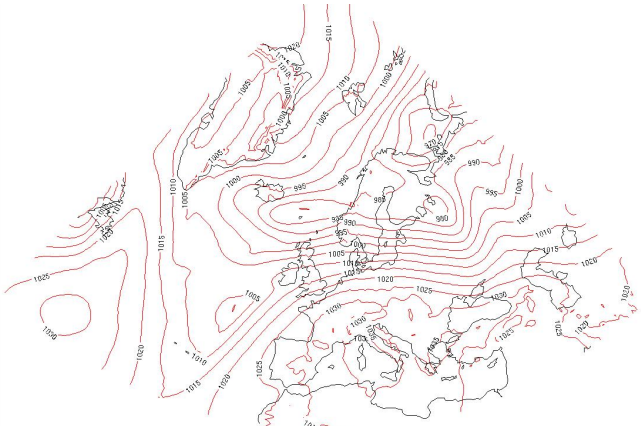

(f) 4. December 1986

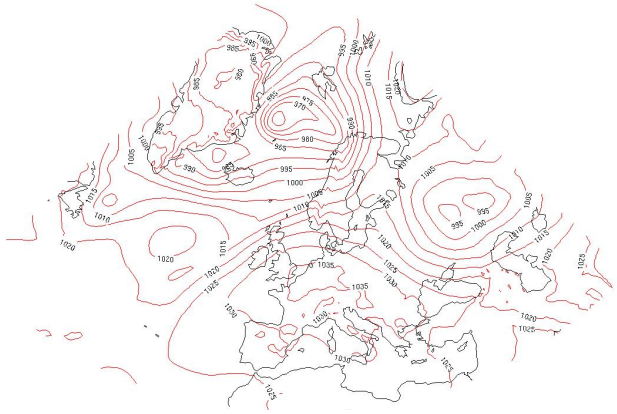

(g) 19. January 1989

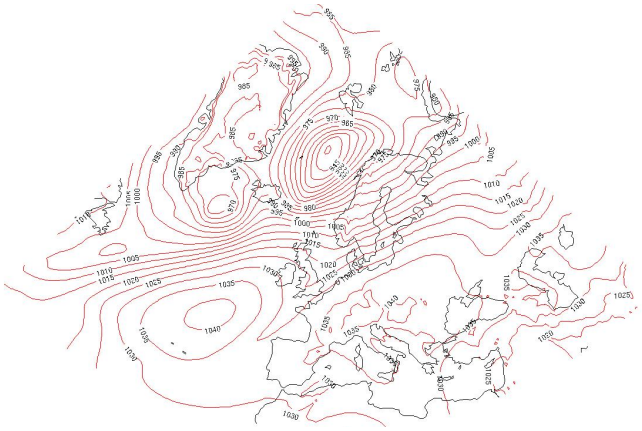

(h) 28. January 1989

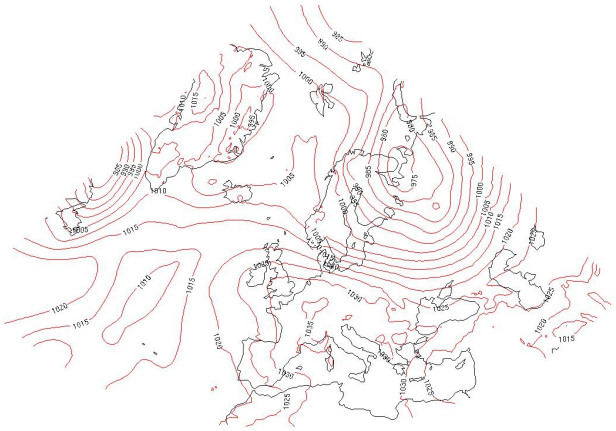

(i) 14. December 1991

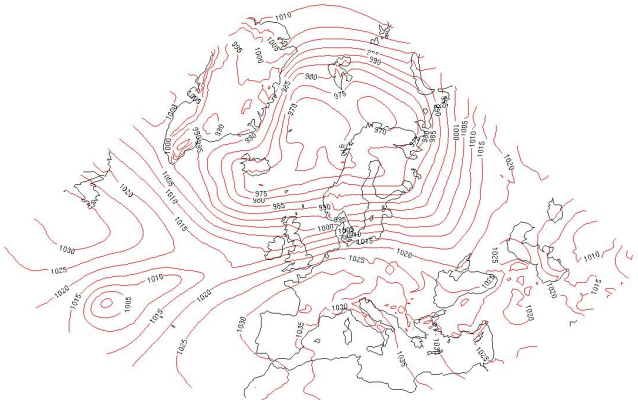

(j) 3 January 1992

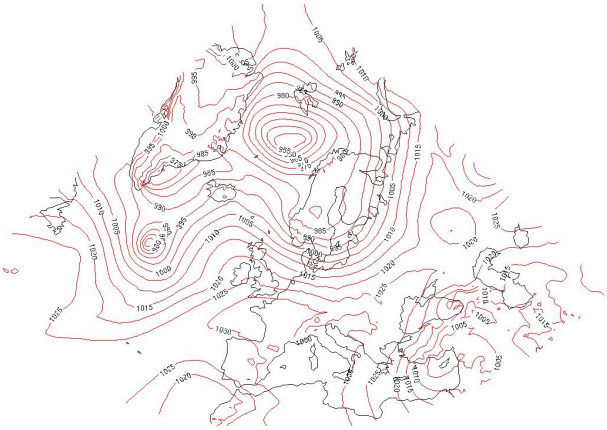

(k) 23. February 1992

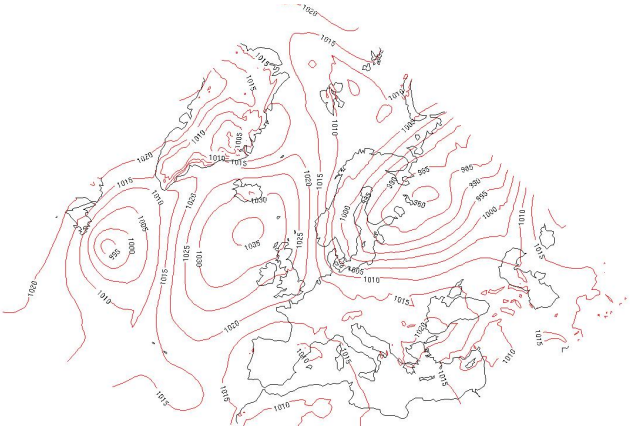

(l) 9. October 1992

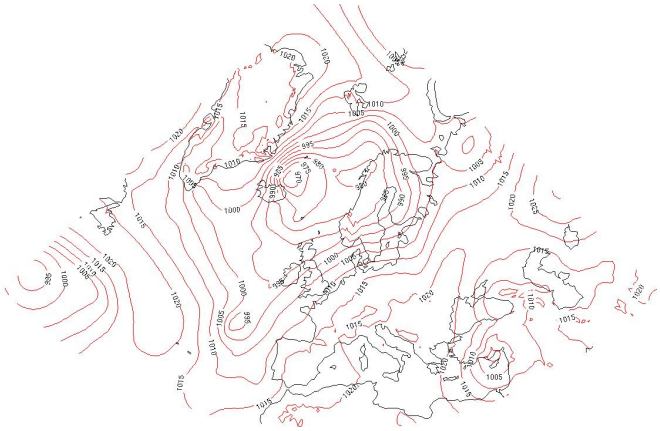

(m) 15. December 1992

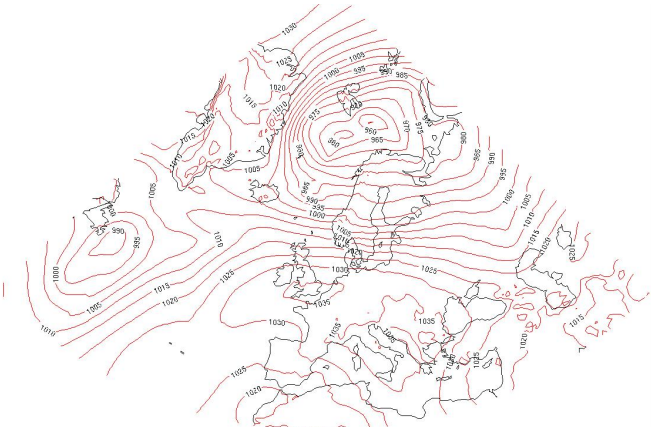

(n) 4. February 1993

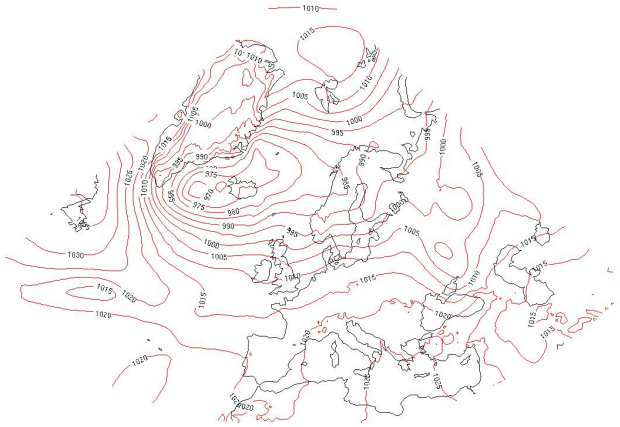

(o) 21. March 1993

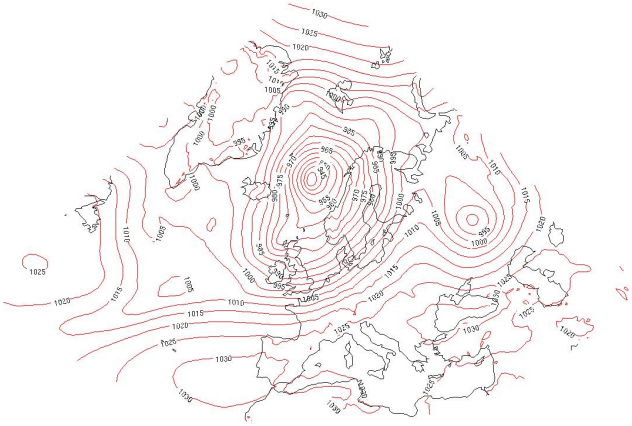

(p) 19. December 1993

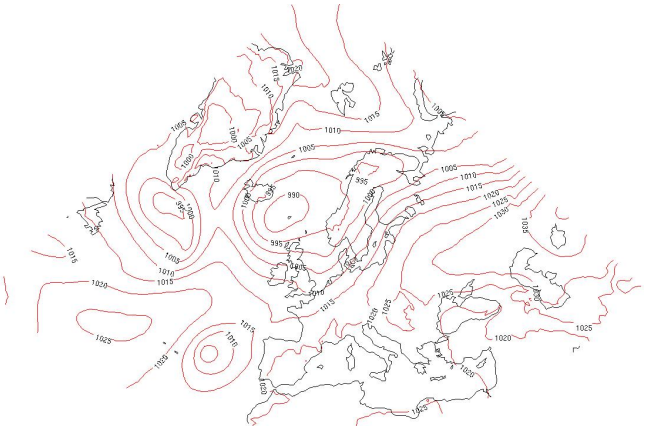

(q) 27. October 1995

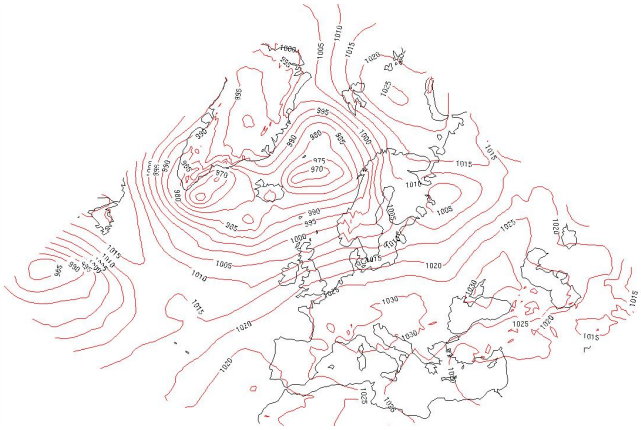

(r) 9. February 1998

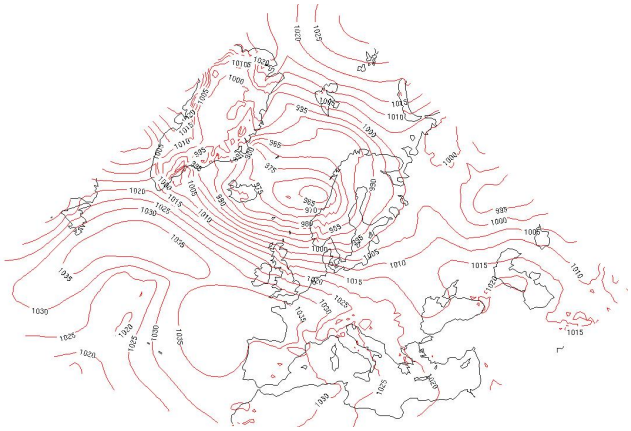

(s) 4. February 1999

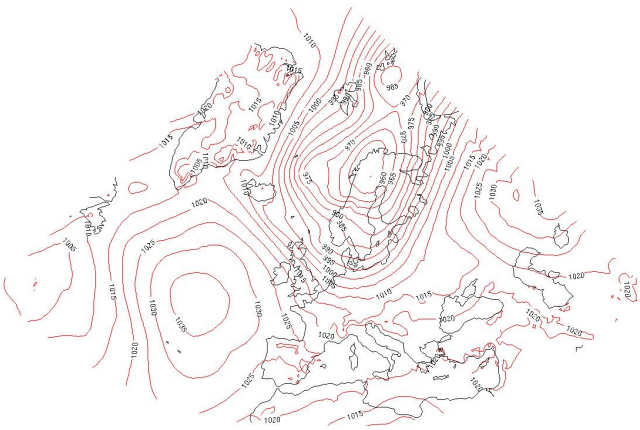

(t) 16. February 1999

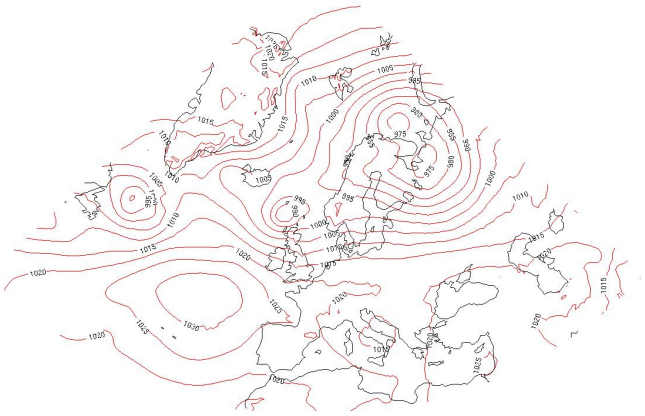

(u) 10. April 1999

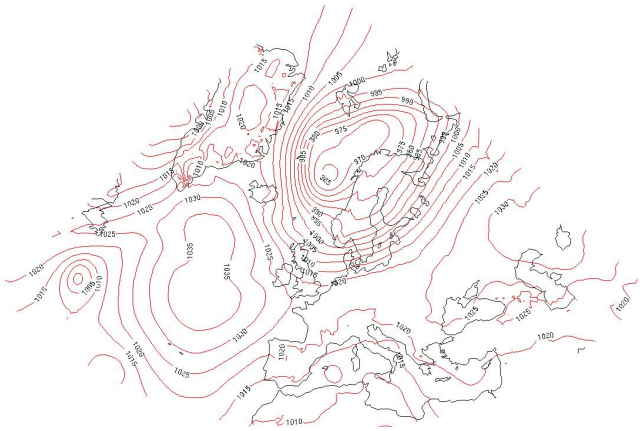

(v) 12. November 2004

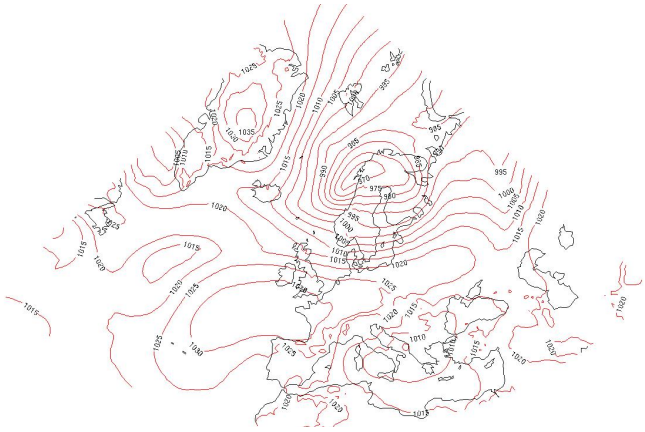

(w) 15. November 2004

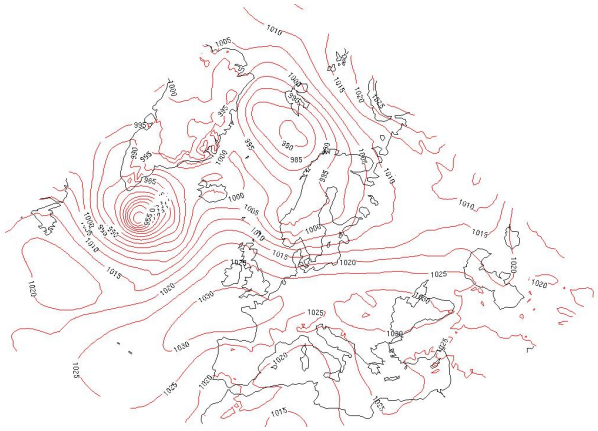

(x) 5. December 2004

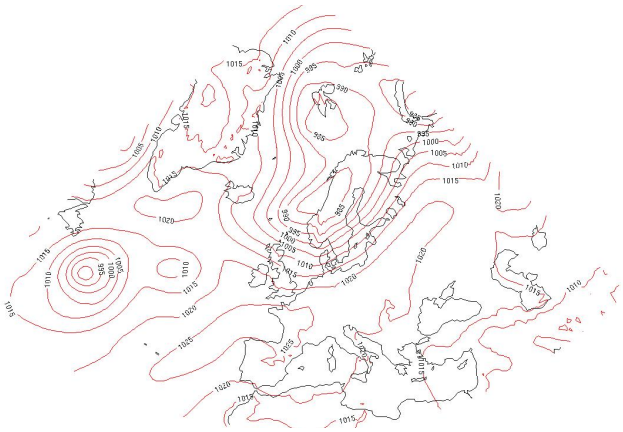

(y) 14. September 2005

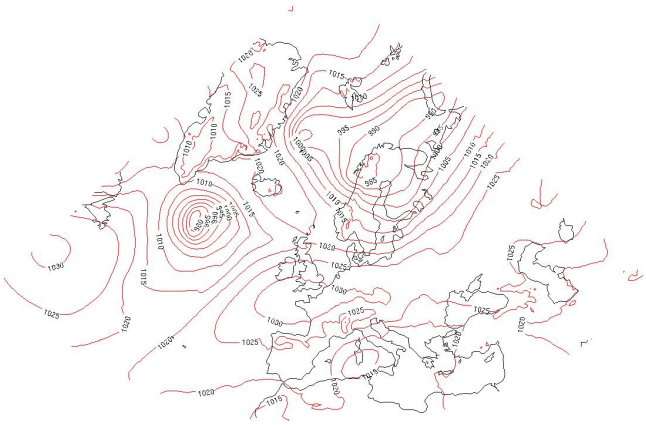

(z) 1. November 2007

Figure C.-43: SLP data from the MERRA reanalysis at 06.00 UTC for the given date. The events a) to z) are organized in a chronicle order from 1961 to 2009.

Appendix D

Figures from the 4 cross sections for the three case studies

The cross section plots are organized in a figure for each individual event. To be able to compare the control run with the simulations with changes SST for each of the four areas (Møre og Romsdal (MR), North of Sognefjorden (NS), South of Sognefjorden (SS) and Sunnhordaland (SH)) they are organized so each area are located at the same page. Each of the bars in the different boxes for the 4 parameters represent an average for that specific longitude in the transect box. The specific humidity is found by taking the vertical average where the vertical layers are not weighted equally. The vertical velocity and relative humidity is found by taking the vertical average over the lowest 3 km.

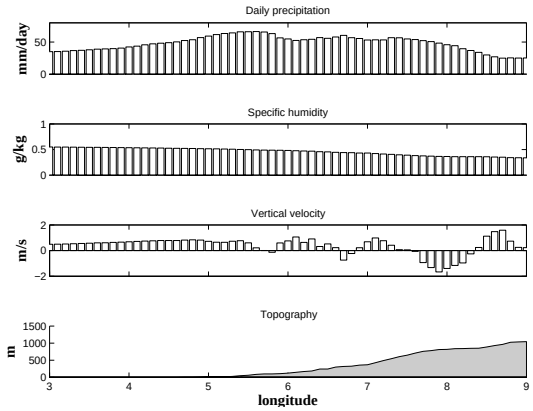

(a) Control run for MR

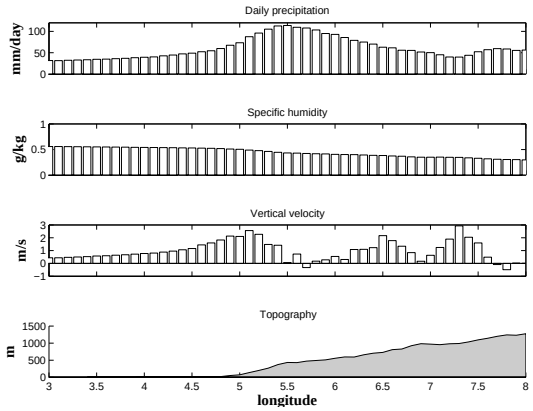

(b) Control run for NS

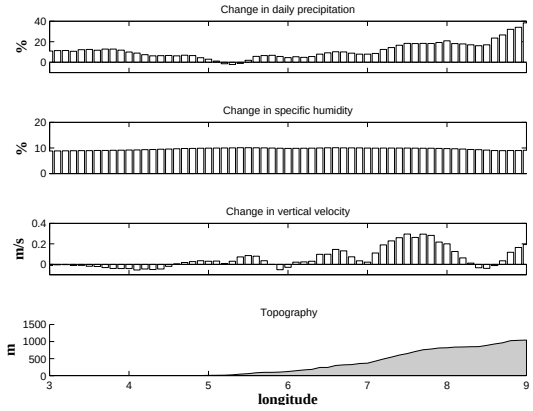

(c) Higher SST for MR

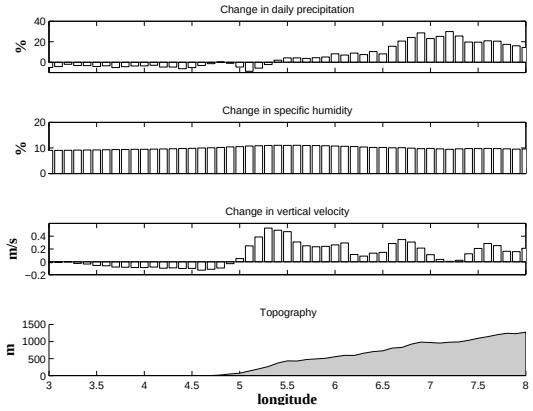

(d) Higher SST for NS

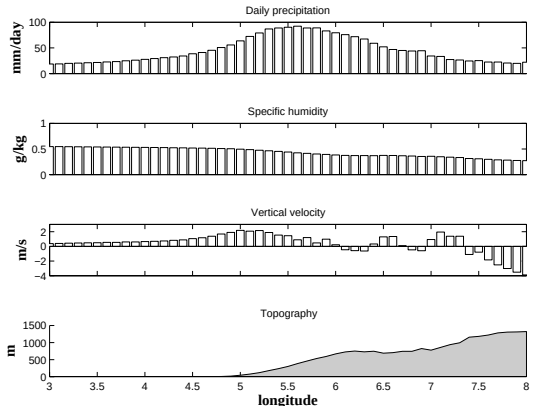

(e) Control run for SS

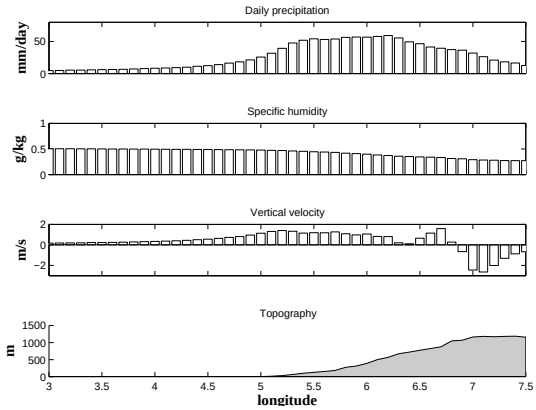

(f) Control run for SH

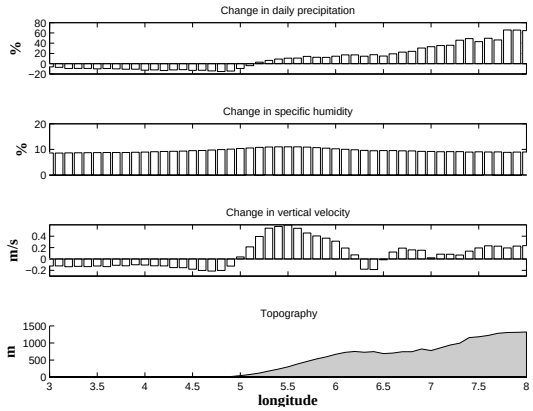

(g) Higher SST for SS

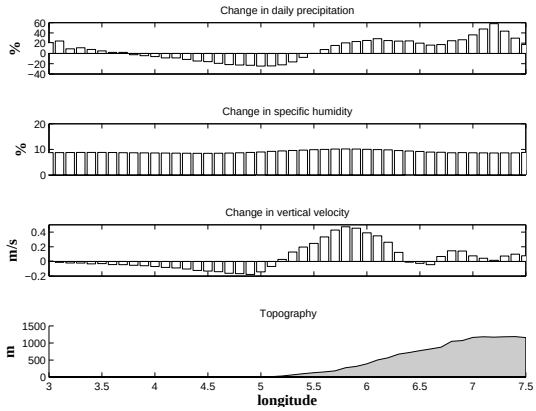

(h) Higher SST for SH

Figure D.-3: Cross sections for 11. January 1992.

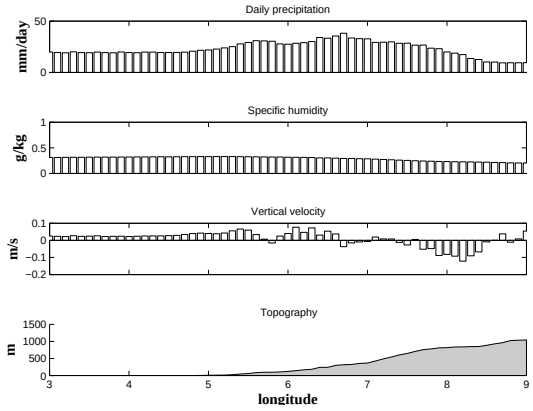

(a) Control run for MR

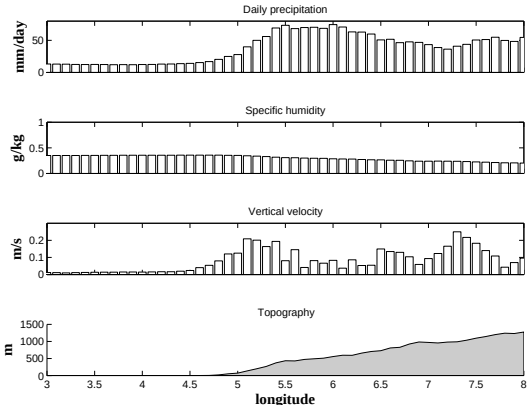

(b) Control run for NS

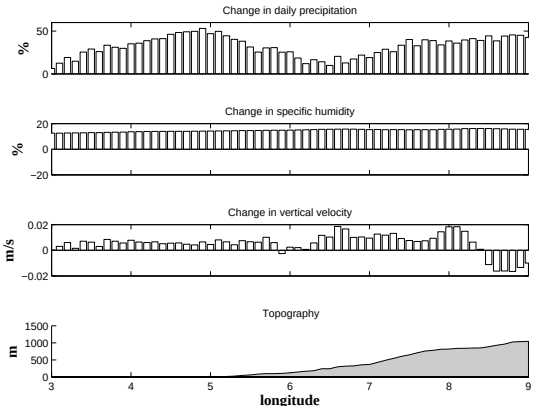

(c) Higher SST for MR

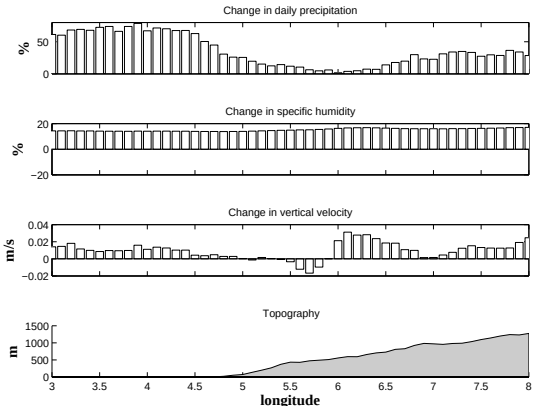

(d) Higher SST for NS

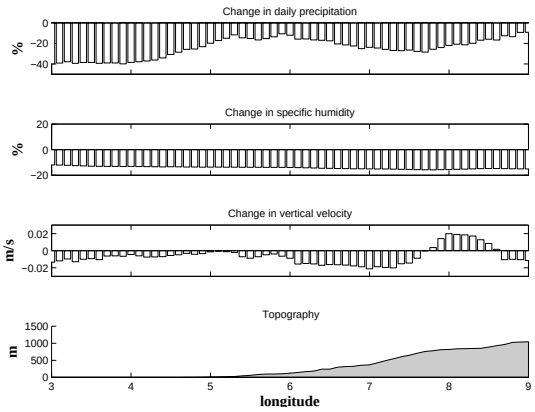

(e) Lower SST for MR

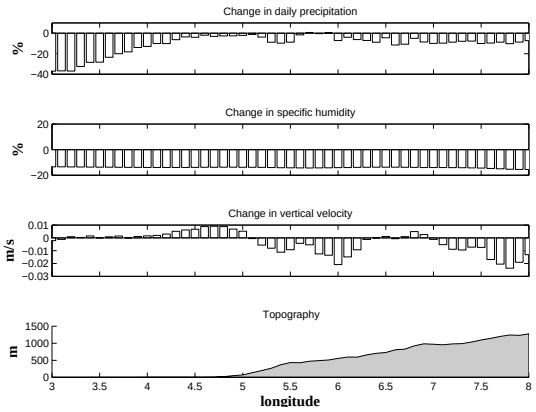

(f) Lower SST for NS

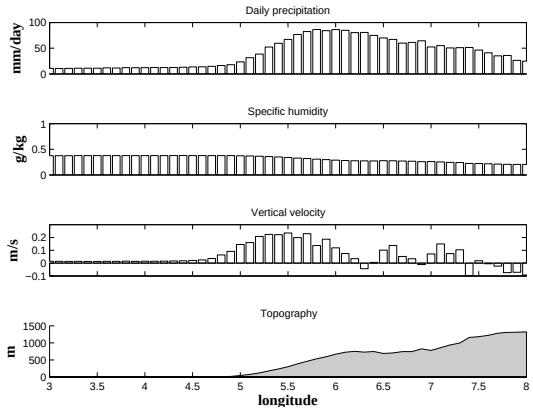

(g) Control run for SS

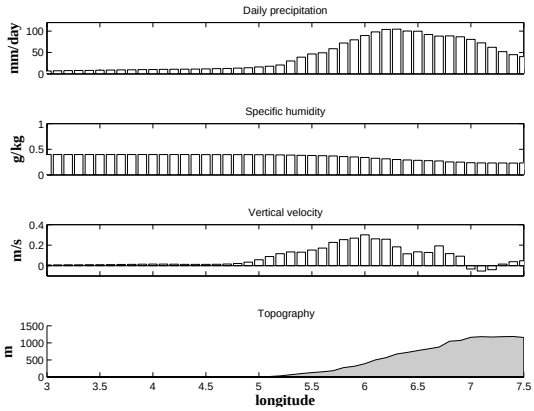

(h) Control run for SH

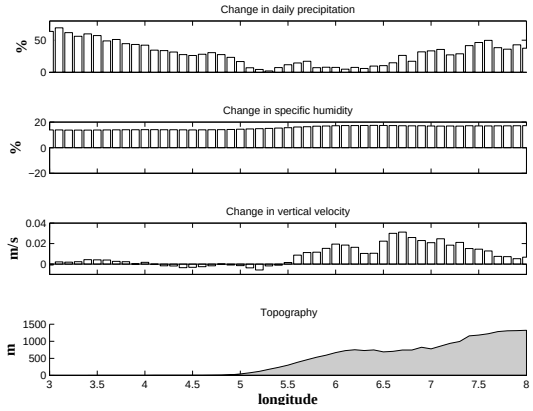

(i) Higher SST for SS

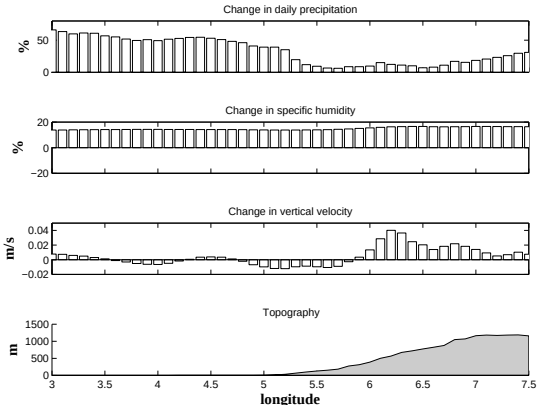

(j) Higher SST for SH

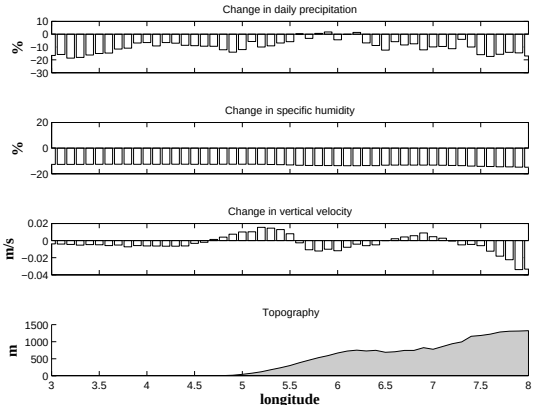

(k) Lower SST for SS

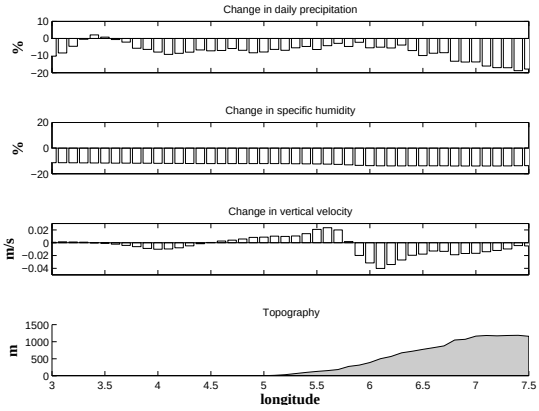

(l) Lower SST for SH

Figure D.-8: Cross sections for 2. March 1997.

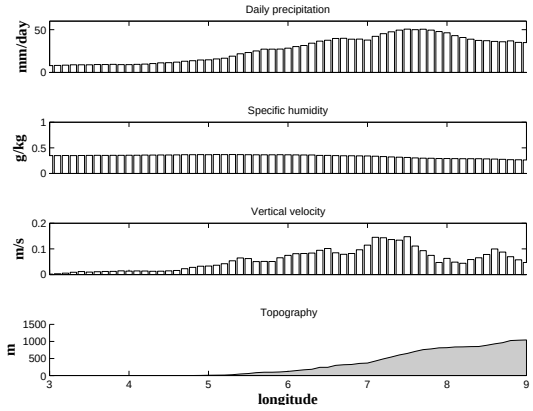

(a) Control run for MR

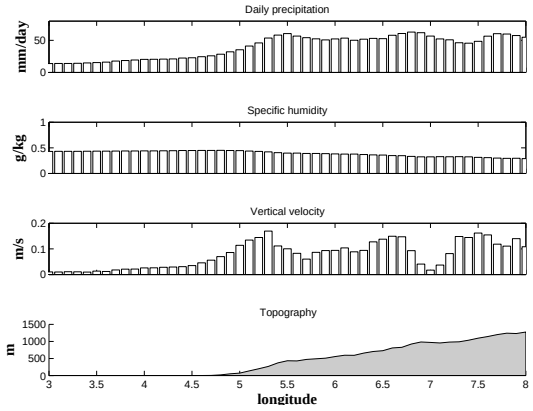

(b) Control run for NS

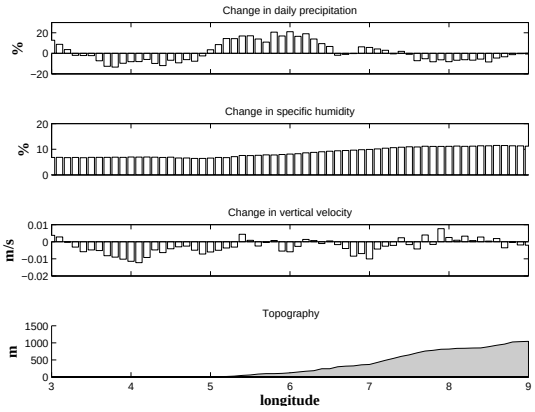

(c) Higher SST for MR

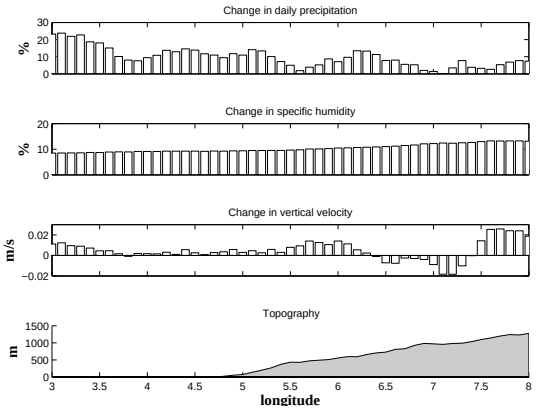

(d) Higher SST for NS

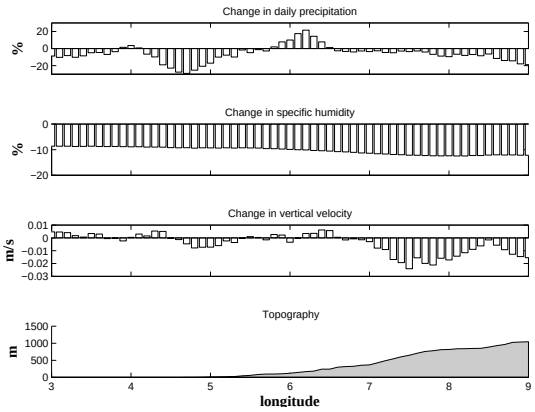

(e) Lower SST for MR

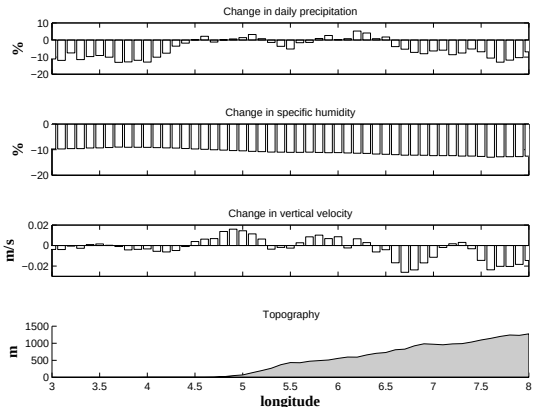

(f) Lower SST for NS

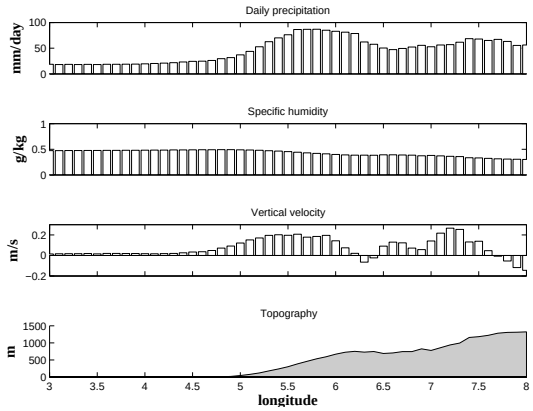

(g) Control run for SS

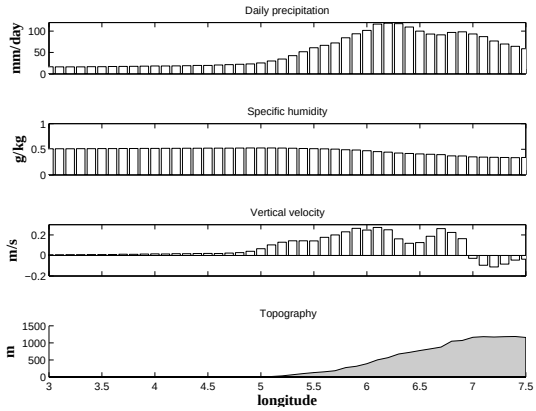

(h) Control run for SH

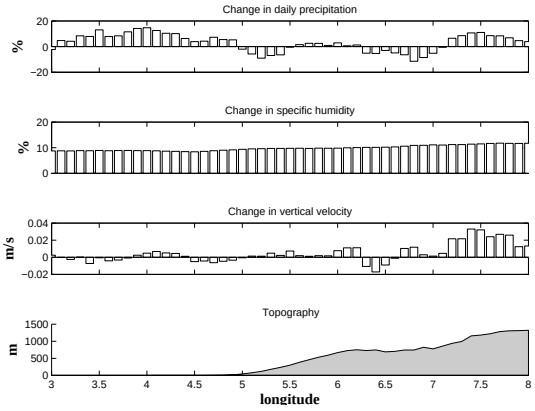

(i) Higher SST for SS

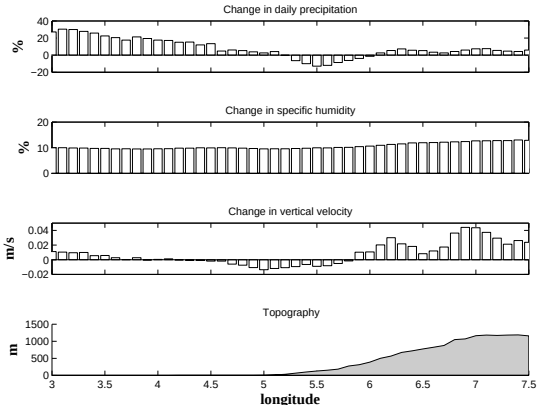

(j) Higher SST for SH

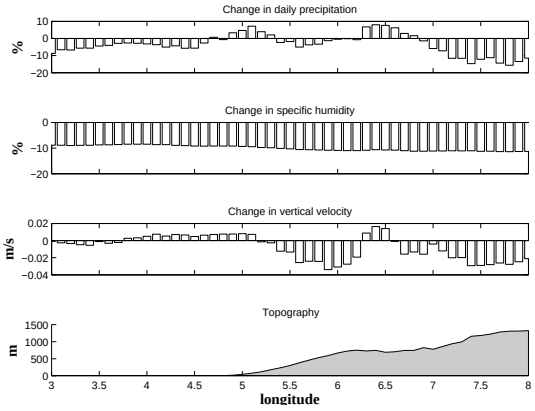

(k) Lower SST for SS

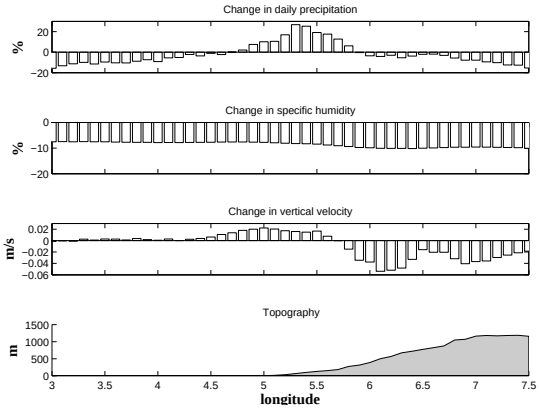

(l) Lower SST for SH

Figure D.-13: Cross sections for 15. November 2005.

References

Alexandru, A., De Elia, R., Laprise, R., Separovic, L., & Biner, S. (2009). Sensitivity study of regional climate model simulations to large-scale nudging parameters. *Monthly Weather Review*, *137*(5), 1666–1686.

Bader, M., & Roach, W. (1977). Orographic rainfall in warm sectors of depressions. *Quarterly Journal of the Royal Meteorological Society*, *103*(436), 269–280.

Bengtsson, L., Hodges, K., & Keenlyside, N. (2009). Will extratropical storms intensify in a warmer climate? *Journal of Climate*, *22*(9), 2276–2301.

Bergeron, T. (1949). The problem of artificial control of rainfall on the globe1: Ii. the coastal orographic maxima of precipitation in autumn and winter. *Tellus*, *1*(3), 15–32.

Bergeron, T. (1960). Physics of precipitation. *American Geophysical Union, Washington, DC*.

Bolton, D. (1980). The computation of equivalent potential temperature. *Monthly Weather Review*, *108*(7), 1046–1053.

Caroletti, G. N., & Barstad, I. (2010). An assessment of future extreme precipitation in western norway using a linear model. *Hydrology and Earth System Sciences*, *14*(11), 2329-2341.

Dee, D. P., Uppala, S. M., Simmons, A. J., Berrisford, P., Poli, P., Kobayashi, S., et al. (2011). The era-interim reanalysis: configuration and performance of the data assimilation system. *Quarterly Journal of the Royal Meteorological Society*, *137*(656), 553–597.

Durran, D., & Klemp, J. (1982). On the effects of moisture on the brunt–väisälä frequency. *Journal of the Atmospheric Science*, *39*, 2152–2158.

Godske, C., Bergeron, T., Bjerknes, J., & Bundgaard, R. (1957). Dynamic meteorology and weather forecasting: Amer. *Meteorology Society, Boston, Mass., and Carnegie Inst. of Washington*.

Haltiner, G., & Williams, R. (1980). *Numerical prediction and dynamic meteorology*. Wiley.

Heikkilä, U., Sandvik, A., & Sorteberg, A. (2010). Dynamical downscaling of era-40 in complex terrain using the wrf regional climate model. *Climate Dynamics*.

Holton, J. (2004). *An introduction to dynamic meteorology* (Vol. 1). Academic press.

Jaedicke, C., Solheim, A., Blikra, L., Stalsberg, K., Sorteberg, A., Aaheim, A., et al. (2008). Spatial and temporal variations of norwegian geohazards in a changing climate, the geoextreme project. *Natural Hazards and Earth System Sciences*, *8*(4), 893–904.

Jiang, Q., & Smith, R. (2003). Cloud timescales and orographic precipitation. *Journal of the Atmospheric Science*, *60*, 1543-15559.

Kunz, M., & Kottmeier, C. (2006). Orographic enhancement of precipitation over low mountain ranges. part i: Model formulation and idealized simulations. *Journal of Applied Meteorology and Climatology*, *45*(8), 1025–1040.

Laprise, R. (1992). The euler equation of motion with hydrostatic pressure as an independent variable. *Monthly Weather Review*, *120*(1), 197–207.

Markowski, P., Richardson, Y., & Unido), R. M. S. R. (2010). *Mesoscale meteorology in midlatitudes*. Wiley Online Library.

Miguez-Macho, G., Stenchikov, G., & Robock, A. (2004). Spectral nudging to eliminate the effects of domain position and geometry in regional climate model simulations. *Journal of Geophysical Research*, *109*, D13104.

Miguez-Macho, G., Stenchikov, G., & Robock, A. (2005). Regional climate simulations over north america: Interaction of local processes with improved large-scale flow. *Journal of Climate*, *18*(8), 1227–1246.

Pall, P., Allen, M., & Stone, D. (2007). Testing the clausius–clapeyron constraint on changes in extreme precipitation under co2 warming. *Climate Dynamics*, *28*(4), 351–363.

Radu, R., Déqué, M., & Somot, S. (2008). Spectral nudging in a spectral regional climate model. *Tellus A*, *60*(5), 898–910.

ResClim. (2005). *Norges klima om 100 år: Usikkerheter og risiko, [brochure].* Available from `http://regclim.met.no/presse/download/regclim_brosjyre2005.pdf`

Rogers, R. R., & Yau, M. K. (1989). *A short course in cloud physics.* (Vol. 1). Pergamon Press.

Sinclair, M. (1994). A diagnostic model for estimating orographic precipitation. *Journal of Applied Meteorology*, *33*(10), 1163–1175.

Skamarock, W. C., Klemp, J. B., Dudhia, J., Gill, D. O., Barker, D. M., Wang, W., et al. (2008). A description of the advanced research wrf version 3.

Smith, R. (1979). The influence of mountains on the atmosphere. *Advances in Geophysics*, *21*, 87–230.

Storch, H. von, Langenberg, H., & Feser, F. (2000). A spectral nudging technique for dynamical downscaling purposes. *Monthly Weather Review*, *128*(10), 3664–3673.

Trenberth, K. (1999). Conceptual framework for changes of extremes of the hydrological cycle with climate change. *Climatic Change*, *42*(1), 327–339.

Waldron, K., Paegle, J., & Horel, J. (1996). Sensitivity of a spectrally filtered and nudged limited-area model to outer model options. *Monthly Weather Review*, *124*(3), 529–547.

Wallace, J. M., & Hobbs, P. V. (2006). *Atmospheric science: an introductory survey* (Vol. 92). Academic press.

Willmott, C., & Matsuura, K. (2005). Advantages of the mean absolute error (mae) over the root mean square error (rmse) in assessing average model performance. *Climate Research*, *30*(1), 79.